Composite particle mean field theory for strongly correlated systems

Daniel Huerga Gómez

Supervisor: Prof. Jorge Dukelsky Bercovich

Instituto de Estructura de la Materia,
Consejo Superior de Investigaciones Científicas

Dto. de Física Teórica de la Materia Condensada,
Universidad Autónoma de Madrid

A thesis submitted for the degree of

Doctor of Philosophy

Madrid, 2014

Resumen

Presentamos un método aplicable a Hamiltonianos que modelizan sistemas bosónicos y fermiónicos fuertemente correlacionados relevantes en física de la materia condensada y de átomos fríos en redes ópticas. El método propuesto resulta particularmente conveniente para describir aislantes de Mott y fases con correlaciones de corto alcance que emergen en sistemas frustrados bosónicos y de espín cuya descripción plantea serias dificultades a otros métodos del estado-del-arte. La idea fundamental reside en la identificación de conjuntos de grados de libertad de la red original (*clusters*) como las piezas básicas que capturan los rasgos esenciales de las fases presentes en el sistema objeto de estudio. Presentamos los *mappings* canónicos que relacionan los operadores the espín, bosónicos y fermiónicos del modelo original con formas bilineales de unos nuevos operadores bosónicos y fermiónicos *compuestos* que representan los estados cuánticos de dichos clusters. Gracias a que el mapping es canónico, el Hamiltoniano de estudio puede reescribirse en términos de estos nuevos operadores compuestos y aproximarse mediante técnicas usuales de muchos cuerpos, con la ventaja de que las correlaciones cuánticas dentro de los clusters están incluidas de manera exacta por definición. Presentamos diferentes esquemas de campo medio autoconsistente aplicables a Hamiltonianos generales de particulas compuestas y con ellos estudiamos diferentes modelos. Concretamente, estudiamos un modelo de espines con interacción en anillo (*ring exchange*), hacemos benchmark de los modelos de Hubbard bosónico y fermiónico y estudiamos un sistema de bosones fuertemente correlacionados en presencia de un campo gauge artificial de flujo π. La teoría de partículas compuestas presentada en esta tesis permite obtener el diagrama de fases del estado fundamental de dichos modelos. El uso de *clusters* como grado de libertad permite la descripción de diferentes fases caracterizadas por diferentes órdenes de largo alcance.

El esquema algebraico establecido mediante los mappings permite la computación de las excitaciones de baja energía como magnones en ferromagnetos o el modo de Higgs y de Goldstone en superfluidos. Además, permite diferentes extensiones y aproximaciones que puedan describir, por ejemplo, fases con correlaciones de largo alcance, o el estudio de dinámica de *quenches* en sistemas de átomos fríos.

Abstract

We present a simple method applicable to lattice spin, bosonic, and fermionic model Hamiltonians relevant for strongly correlated condensed matter and cold atom physics. In particular, it is well suited to describe short-range correlated phases emerging in frustrated spin and bosonic systems that pose significant problems to other state-of-the-art techniques. The key idea resides on the identification of clusters of the original degrees of freedom as the building blocks capturing the necessary quantum correlations to describe the essential features of the phases present in the system under study. We present the canonical mappings that relate the spin, bosonic and fermionic operators of the original lattice to bilinear forms of new *composite* bosons and fermions that describe the quantum many-body states of these clusters. The model of interest can be reexpressed in terms of this new set of composite operators and approached by standard many-body techniques, with the advantage that quantum correlations inside the cluster are automatically computed from the onset. We present various self-consistent mean-field schemes applicable to general composite particle Hamiltonians and apply them to different models. In particular, we study a model of spins with ring-exchange interaction, we benchmark the bosonic and fermionic Hubbard models, and study a system of strongly interacting bosons in the presence of a π-flux artificial gauge field. The composite particle mean field theory presented in this thesis allows to map the ground-state phase diagram of these models. The use of clusters as the basic degree of freedom allows for the description of different phases characterized by coexistence and competition of different orders. Finally, the algebraic framework set by the mappings allows for the computation of low-lying excitations such as magnon dispersions on ferromagnets or the Higgs and Goldstone modes in superfluids. Further extensions and approximation schemes may permit the description of long-range correlated phases, or the study of quench-dynamics in cold atom systems.

Acknowledgements

The work presented in this thesis has been developed during a restrictive period for Spanish research and education. As a milestone event, the Spanish Research Council (CSIC) declared a temporary receivership in Summer 2012 that caused the risk of its economic collapse one year later.

In spite of these discouraging circumstances, I have had the chance to meet students, postdocs, professors and researchers with who I have greatly learned and enriched. The completion of this thesis have been possible thanks to all of them.

I want to thank my supervisor, Jorge Dukelsky, for his patience in the early stages, for being always willing to discuss on the blackboard about any problem or idea, for his support and guidance, and his efforts in doing my PhD experience productive and interesting.

I want to thank Gerardo Ortiz, for the intense and fruitful discussions, for his good pedagogy and contagious enthusiasm. I want to thank Leonid Isaev, for his help with my first codes and the discussions at Bloomington.

I thank Gustavo E. Scuseria, Jinmo Zhao and Carlos Jimenez-Hoyos for the intense and synergistic discussions, with which I have greatly learned. I want to thank Ireneusz W. Bulik for his invaluable help with ARPACK.

I want to thank Nicolas Laflorencie and the Groupe des Fermions Fortements Correlés of the Laboratoire de Physique Théorique de l'Université Paul Sabatier de Toulouse for their hospitality and the interesting discussions which have contributed positively to my knowledge. I specially thank all the students and postdocs who made of my stay in Toulouse a nice experience. I want to thank Sandrine for her help with Linux.

I want to thank Luis Santos and Sebastian Greschner for sharing their knowledge and enthusiasm. I thank the hospitality and the nice discussions with the Quantum Optics group from the Institut für Theoretische Physik, Hannover.

I thank the Instituto de Estructura de la Materia and my colleagues from the Theoretical Chemistry and Physics Department, who have made my PhD time more pleasant. I thank Rafael Molina for his help with Linux, his advices, and his help for a proper Fortran coding, Jordi Mur-Petit for his pedagogy and help with the seminars, Beamer and Latex. I thank Stefan Rombouts for his help with Fortran and bosonic canonical tranformations. I thank Pedro Sarriguren, Eduardo Garrido, Carolina Romero, Raúl de Diego, Laura Ortiz, Juanma, Diana, Alejandro, Armando Relaño, Herr Mathias Lunde, Javier Rodriguez-Laguna, Carlos Esebbag, Niku Sandulescu and Rayner Rodriguez-Guzmán for the warm and relaxed lunchtimes.

I acknowledge financial support from the Ministry of Economy and Competitiveness of Spain through grants BES-2010-031607, EEBB-2011-44056, EEBB-12-03677, EEBB-13-06139 and EEBB-14-09077. This thesis would have not been possible without it.

Special thanks to Pedro de Andrés for his always good advice and encouraging support, to Alejandro Bermudez for the nice discussions when driving Milano-Trento, to Giovanni Ramirez for his invaluable help with the world of Linux, to Fernando de Juan and Nerea for sharing "the Bloomington experience", to Tapan and Nandha for their familiarity, to Philipp for his hospitality and friendship, to Luca for his friendship, advices and help, to Pedro (Maestro!) for the good discussions of physics and more, to Sumiran for the trips to students cantine.

Special thanks to Dani Trompas and Diego Armando, for the infallible crisis plans, for the good advices and the best congresses. Thanks for your encouraging support and friendship.

Special thanks to João Nuno. Thanks for that cite of Pessoa, which came to my mind several times.

The thesis has been possible also thanks to all my family, with who I can always share the good and the not so good, with who I have shared lots of moments of the daily life.

Je voudrais remercier Xavier, Marie, Louise, Felix et Christoff pour leur familiarité et leur bon humour.

Gracias a Tefi, Álex, Glor, Ari, Tere, Cano, Peter, Will, Barbados... Pablo, Paco, Juan, Paola, Marta, Maykel, Esther, Marta y David, por vuestra amistad imrescindible y disposición a celebrar.

Gracias a Ivanova por la crítica excéntrica, siempre bienvenida.

Gracias a Merino, por el entusiasmo y las máquinas mortíferas.

Gracias a Top y Enrique, por la mejor música frita, por la dialéctica, por compartir los atardeceres estivales del Sampeter y la emoción sobrecogedora al filo de Malcaras y Posets.

Gracias a Camille, por tu cariño, por estar siempre a este y al otro lado.

Gracias a Irene, Mario, Maite, por vuestro apoyo incondicional.

Madrid, Agosto 2014.

Contents

Chapter 1

Introduction

Strongly correlated materials show a rich variety of fascinating properties intrinsically characterized by the collective behavior of electrons. Contrary to usual metals and semimetals, the phenomena emerging in these systems cannot be described in terms of non-interacting *quasi-particles* moving over a uniform background. In materials characterized by having f and d open shells, the electrons experience a strong Coulomb repulsion due to the localized shape of the electron orbitals. The complex interplay of the electrons' internal degrees of freedom leads to the emergence of a plethora of exotic phases at low temperatures, many of them still not well understood. Well-known examples are the high transition temperatures in layered copper-oxides [1] and iron based superconductors [2] or the unusally big effective fermion masses in the so-called heavy fermion systems [3]. Due to their extreme sensibility to the microscopic details, different simplified model Hamiltonians are used to describe the materials showing these phenomena.

The Hubbard model is the minimal tight-binding model that accounts for the competition of the free kinetic energy of the electrons and their interaction at the localized atomic shells. It is the paradigmatic strongly correlated model, as it was originally proposed to describe the physics of the electrons in transition metal oxides, and afterwards it has been used to describe cuprate superconductors and heavy-fermion compounds. It exhibits a metal-insulator transition, being the weakly interacting limit governed by the Fermi-liquid behaviour. In the strong interacting limit or Mott insulator phase, electrons tend to localize in the atomic shells. The addition or removal of an electron in an atomic shell costs a finite energy proportional to the strong electron-electron interaction, rendering the system insulating. In this limit, the low-energy charge and spin excitations can be described by the effective t-J model. At half-filling, the combination of strong interaction and Pauli exclusion principle induces the electrons to fill uniformly the lattice and to have opposite spin with respect

to their respective nearest neighbours in order to minimize the energy via superexchange processes [4]. In this regime, the low-energy physics is primarily governed by spin excitations and it can be effectively described by quantum Heisenberg models. The broad variety of Mott insulators leads to a large family of spin models comprising the field of quantum magnetism. For example, lanthanides are believed to be described by the family of Kitaev-Heisenberg models on the honeycomb lattice [5], iron arsenides are described by the J_1-J_2 Heisenberg model [6], and the Heisenberg antiferromagnet on the Kagome lattice is expected to describe the herbertsmithites [7].

In spite of the simplicity of these models, finding their ground state is far from trivial; the combination of strong interactions and low dimensionality results in strong quantum fluctuations and the competition of different long-range orders. The impossibility to minimize all the terms in the model at the same time leads to strong *frustration* [8], and the emergence of exotic short-range and long-range correlated phases.

In order to overcome these difficulties, numerous theoretical schemes have been developed along the years. In spite of computers increasing power, the exponential scaling of the Hilbert space with the size of the system makes these computations to be extremely expensive, and severe approximations have to be carried out. At the same time, the rapid experimental development of ultracold atoms loaded in optical lattices opens the possibility to probe *in situ* these strongly correlated models, and some others of interest on other areas of physics. Since the first proposal and posterior experimental realization of the superfluid-to-Mott transition of the Bose-Hubbard model, a large variety of spin, bosonic, and fermionic systems have been proposed for cold-atom experimental implementation. These include Hubbard-type models, spin-boson models, spin-glass models, bosonic systems in the presence of disorder or synthetic gauge fields, among others [9].

Among the various available numerical techniques the density matrix renormalization group (DMRG), quantum Monte Carlo (QMC), and exact diagonalization (ED) methods stand out for being exact within numerical precision. Nevertheless, they suffer from several limitations. The DMRG method is mainly restricted to one-dimensional and quasi-one-dimensional systems with short-range interactions. Its extension to two-dimensions requires sophisticated choices of one-dimensional paths covering the lattice that induce ficticious long-range interactions and reduce the precision of results. The QMC method suffers from the infamous "sign problem" that limits its application to non-frustrated bosonic systems in general, and to fermionic

systems in some particular cases. The ED method is restricted to small lattice sizes of a few tens of spins in two-dimensions and expensive computations are needed in order to obtain information about the thermodynamic limit through scaling analysis. Other approximate methods based on the dynamical variational principle require sophisticated computational implementations. Such is the case of the dynamical mean-field theory (DMFT) and its cellular extension, or the family of cluster methods such as the variational cluster approximation (VCA).

The aim of this thesis is to provide a simple and inexpensive alternative method to unveil strongly correlated phases of bosonic and fermionic lattice systems where the other methodologies find serious difficulties or are even inapplicable. In particular, frustrated spin and bosonic models in two-dimensional geometries with relevance in condensed matter and cold atom physics. With this purpose, we extend the algebraic framework of the Hierarchical Mean Field Theory (HMFT) [10] to treat general bosonic and fermionic systems. We propose several mean-field schemes based on the initial identification of composite degrees of freedom as the basic building blocks containing the significant quantum correlations of the phases present in the system under study. By setting a general algebraic framework we open up the possibility to extend the method further by implementing other approximations or combining it with other methodologies.

The outline of the thesis is as follows:

In Chapter 2 we set up the algebraic framework that will be used throughout the thesis. In particular, we present the canonical mappings relating the spin, boson and fermion operators of the original system with a new set of *composite particle* operators. The mappings can be considered a cluster extension of the Dickerscheid mapping [11] of bosons, and the Zou-Anderson mapping [12] of fermions, respectively. As the mappings are canonical the Hamiltonian of interest can be rewritten in terms of composite operators and treated by different approximations. We describe several mean-field schemes that can be applied to general composite particle Hamiltonians. The formalism presented in this Chapter is contained in Ref. [13] and in Ref. [14].

In Chapter 3 we study a system of hard-core bosons with a frustrating double-hopping or ring-exchange term in the presence of external chemical potential. We map out the phase diagram over the frustrated and non-frustrated regions obtaining several novel superfluid and solid phases characterized by the presence of chirality. The results presented in this Chapter are contained in Ref. [15].

In Chapter 4 we benchmark the composite boson coherent wave function proposed in Chapter 2 against the Bose-Hubbard model in two-dimensions. The phase diagram obtained is in quantitative agreement with QMC computations and the composite particle approach allows for the description of the low-lying Goldstone and Higgs excitation modes of the superfluid in agreement with recent cold atom experiments. These results are contained in Ref. [13].

In Chapter 5 we study a system of bosons in the presence of an artificial π-flux magnetic field, which may be implemented with current cold atom experimental techniques. We study the evolution of the phase diagram with the dimensionality by computing two- and four-leg ladders and two-dimensions. We obtain several fractional Mott plateaux as well as stable chiral superfluid and supersolid phases. These results comprise a yet unpublished work.

In Chapter 6 we benchmark a composite fermion-boson mean-field scheme presented in Chapter 2 against the Fermi Hubbard model in one- and two-dimensions obtaining a good description of the Mott phase. The results obtained are contained in Ref. [14].

In Chapter 7 we end up with a summary and discuss further applications and extensions of the method.

Chapter 2

Composite degrees of freedom

In this Chapter we provide the theoretical framework that is proposed in this thesis to approach the models of strongly correlated systems. It can be considered as an extension to the Hierarchical Mean Field Theory (HMFT)[10]; an algebraic framework that has already been successfully applied to different frustrated models of relevance in quantum magnetism. We extend the HMFT ideas in order to treat general lattice bosonic or fermionic Hamiltonians relevant for condensed matter and cold atom physics.

The HMFT is an algebraic formalism based on the identification of the relevant elementary degrees of freedom which capture the necessary quantum correlations in order to describe the essential features of the phases present in the system under study. The set of operators that describe the quantum states of the new degrees of freedom and their algebra provide the *hierarchical language* [10] adequate to describe the system. The use of this method combined with bond-algebra techniques and duality mappings [16, 17, 18] makes the HMFT a suitable and powerful technique to investigate phase diagrams of strongly correlated systems.

In practice, we tile the original many-body Fock space into clusters preserving most of the symmetries of the Hamiltonian and represent each many-body state by the action of a composite operator over the vacuum of a new enlarged Fock space. The mapping that relates the original set of operators and the new composite ones is canonical if a physical constraint is implemented. As a consequence, the Hamiltonian of study can be exactly reexpressed in the new language of composite operators and treated by standard many-body techniques, with the advantage that the intra-cluster quantum correlations are computed exactly from the onset.

Here, we will focus on two-dimensional systems in the thermodynamic limit and tile the real-space lattice yielding to a cluster superlattice. Nevertheless, different tilings are possible. We will identify the clusters of the resulting superlattice as the

new composite degrees of freedom. The new set of operators, dubbed *composite bosons* (CB) and *composite fermions* (CF), carry a label indicating their position in the superlattice and an additional quantum label corresponding to the respective bosonic or fermionic cluster many-body state that they describe. The physical subspace of the new enlarged composite particle Fock space is defined by all those many-body composite particle states having *one and only one* composite particle at each superlattice site.

In the following, we present the CB mapping that relates bosonic and spin operators[1] on the lattice to bilinear forms of CBs on the superlattice (Section 2.1). We describe two different mean-field schemes to treat the resulting CB Hamiltonian. In the first case, we use a product of uncorrelated clusters, or CB Gutzwiller ansatz (Section 2.2) to map the ground state phase diagram. Correlations among clusters can be added to obtain the low-lying excitations over the ground state within a self-consistent Bogoliubov scheme by using a CB coherent-Bogoliubov ansatz (Section 2.3).

Also, we introduce the composite fermion-boson (CFB) mapping that relates fermionic operators to bilinear forms of CBs and CFs (CF×CB), where now the CFs are introduced in order to preserve the fermionic statistics (Section 2.4). We describe two mean-field schemes to treat a general composite particle Hamiltonian derived from the mapping. Specifically, we propose a CFB ansatz which decouples the CB and CF sectors. We treat the CF sector within a Bogoliubov approximation and approach the CB sector either with a CB coherent ansatz or with a CB Bogoliubov ansatz (Section 2.5).

2.1 The composite boson mapping

Let us start by tiling the real-space lattice into a perfect superlattice of clusters, in such a way that each one of the sites of the original lattice belongs to only one cluster of the superlattice. We represent each many-body bosonic state of the cluster as the action of a creation CB operator over a CB vacuum,

$$|\mathbf{Rn}\rangle \rightarrow b^{\dagger}_{\mathbf{Rn}}|0\rangle_B, \tag{2.1}$$

where $\mathbf{R}$ labels the position of the cluster in the superlattice, and $\mathbf{n} = (n_1, \ldots, n_V)$ refers to a many-body bosonic state in the occupation basis of a cluster with V sites.

[1] These can be equivalently represented as *hard-core* bosons via the Matsubara-Matsuda mapping.

The physical subspace of the new CB Fock space is spanned by all those many-body CB states having *one-and-only-one* CB at each superlattice site $\mathbf{R}$,

$$|\Psi_{\{\mathbf{n}\}}\rangle = \prod_{\mathbf{R}} b^{\dagger}_{\mathbf{Rn}}|0\rangle_B. \tag{2.2}$$

where $\{\mathbf{n}\}$ refers to a particular configuration of the superlattice space, i.e., $\{\mathbf{n}\} = (\ldots, \mathbf{n}, \mathbf{n}', \ldots)$. The relation between the original bosonic operators and these new CBs can be set in the following form,

$$a^{\dagger}_i = \sum_{\mathbf{m},\mathbf{n}} \langle \mathbf{Rm}|a^{\dagger}_i|\mathbf{Rn}\rangle \; b^{\dagger}_{\mathbf{Rm}} b_{\mathbf{Rn}}, \qquad a_i = (a^{\dagger}_i)^{\dagger}, \tag{2.3}$$

where i labels a site of the original lattice contained in the cluster $\mathbf{R}$, and $\mathbf{m}$ and $\mathbf{n}$ refer to cluster many-body configurations in the occupation basis. In order to preserve the canonical bosonic commutation relations of the original operators, $[a_i, a^{\dagger}_j] = \delta_{i,j}$, three conditions must be fulfilled by the CBs, namely,
i) resolution of the identity,

$$\sum_{\mathbf{n}} |\mathbf{Rn}\rangle \langle \mathbf{Rn}| = I, \tag{2.4}$$

ii) bosonic canonical relations,

$$[b_{\mathbf{Rn}}, b^{\dagger}_{\mathbf{R'n'}}] = \delta_{\mathbf{RR'}}\delta_{\mathbf{nn'}}, \qquad [b_{\mathbf{Rn}}, b_{\mathbf{R'n'}}] = 0, \qquad [b^{\dagger}_{\mathbf{Rn}}, b^{\dagger}_{\mathbf{R'n'}}] = 0, \tag{2.5}$$

and *iii)* physical constraint,

$$\sum_{\mathbf{n}} b^{\dagger}_{\mathbf{Rn}} b_{\mathbf{Rn}} = 1. \tag{2.6}$$

The demonstration of the satisfaction of the canonical relations based on *i*), *ii*) and *iii*) is straightforward though a little bit lengthy, therefore, it is given in the Appendix 2.A. The mapping (2.3) can be expressed in any general CB basis $\{b^{\dagger}_{\mathbf{R}\alpha}, b_{\mathbf{R}\alpha}\}$ whenever these conditions are satisfied. It can be considered a cluster generalization of the slave-boson mapping of canonical bosons [11]. In the particular case where the original bosonic operators $\{a^{\dagger}_i, a_j\}$ refer to *hard-core* bosons, the mapping (2.3) can be considered a cluster generalization of the Schwinger-boson mapping [4] of $S = 1/2$ spin operators [19].

A direct consequence of the CB mapping (2.3) is that any operator $\hat{\mathcal{O}}_{\mathbf{R}}$ that is an algebraic function of the original operators $\{a_i, a^{\dagger}_j\}$ acting on sites lying within a single cluster will be mapped to a one-body CB operator,

$$\hat{\mathcal{O}}_{\mathbf{R}} = \sum_{\alpha\beta} \langle \mathbf{R}\alpha|\hat{\mathcal{O}}_{\mathbf{R}}\,|\mathbf{R}\beta\rangle \; b^{\dagger}_{\mathbf{R}\alpha} b_{\mathbf{R}\beta}. \tag{2.7}$$

Expression (2.7) accounts for the effect of the operator $\hat{\mathcal{O}}_{\mathbf{R}}$ over the cluster configuration β changing into another cluster configuration α, weighted by its transition probability. Moreover, if a general algebraic function contains operators acting on sites which are contained in two different clusters at positions $\mathbf{R}$ and $\mathbf{R}'$, it will be mapped to a two-body CB operator,

$$\hat{\mathcal{O}}_{\mathbf{R},\mathbf{R}'} = \sum_{\alpha\beta} \langle \mathbf{R}\alpha; \mathbf{R}'\alpha' | \hat{\mathcal{O}}_{\mathbf{R},\mathbf{R}'} | \mathbf{R}\beta; \mathbf{R}'\beta' \rangle \, b^{\dagger}_{\mathbf{R}\alpha} b^{\dagger}_{\mathbf{R}'\alpha'} b_{\mathbf{R}\beta} b_{\mathbf{R}'\beta'}. \tag{2.8}$$

In the same way, any product of operators belonging to n different clusters will be mapped to an n-body CB operator. A formal derivation starting from the mapping (2.3) and using conditions (2.4), (2.5) and (2.6) is given in the Appendix 2.B for various specific cases which will be of use in this thesis. Once we have chosen a particular tiling of the original lattice, this recipe allow us to map any operator exactly in the CB Fock space. In particular, we can arrange the terms of the Hamiltonian of study depending on the number of clusters that they involve

$$\begin{aligned} H &= \sum_{\mathbf{R}} H^{\square}_{\mathbf{R}} + \sum_{\mathbf{R}_1\mathbf{R}_2} H^{\parallel}_{\mathbf{R}_1\mathbf{R}_2} \\ &\quad + \sum_{\mathbf{R}_1\mathbf{R}_2\mathbf{R}_3} H^{III}_{\mathbf{R}_1\mathbf{R}_2\mathbf{R}_3} + \sum_{\mathbf{R}_1,\mathbf{R}_2,\mathbf{R}_3,\mathbf{R}_4} H^{\times}_{\mathbf{R}_1,\mathbf{R}_2,\mathbf{R}_3,\mathbf{R}_4} + \ldots, \end{aligned} \tag{2.9}$$

where the symbols $\square$ refers to an intra-cluster term, and $\parallel$, III and $\times$, to inter-cluster terms involving two, three and four different clusters, respectively. Using the previous recipe, we can map it onto the CB Fock space. Terms involving two sites (e.g. a hopping term) will be mapped onto either one-body CB terms, if the hopping acts within a cluster, or two-body CB terms, if the hopping acts between two clusters. For the sake of simplicity, let us assume a boson Hamiltonian that acts at most between two clusters [2], being the generalization to n clusters straightforward, as it will be shown in Chapter 3 through a particular example. The composite boson mappings (2.7) and (2.8) lead to a CB Hamiltonian of the general form

$$H^B = \sum_{\mathbf{R}} (T_{\mathbf{R}})^{\alpha}_{\beta} \; b^{\dagger}_{\mathbf{R}\alpha} b_{\mathbf{R}\beta} + \sum_{\mathbf{R}\mathbf{R}'} (V_{\mathbf{R}\mathbf{R}'})^{\alpha\alpha'}_{\beta\beta'} \; b^{\dagger}_{\mathbf{R}\alpha} b^{\dagger}_{\mathbf{R}'\alpha'} b_{\mathbf{R}\beta} b_{\mathbf{R}'\beta'} \, , \tag{2.10}$$

where repeated Greek indices sum and the tensors $\hat{T}$ and $\hat{V}$ are defined by

$$(T_{\mathbf{R}})^{\alpha}_{\beta} = \langle \mathbf{R}\alpha | \, H^{\square} \, | \mathbf{R}\beta \rangle \, , \tag{2.11}$$

$$(V_{\mathbf{R}\mathbf{R}'})^{\alpha\alpha'}_{\beta\beta'} = \langle \mathbf{R}\alpha, \mathbf{R}'\alpha' | \, H^{\parallel} \, | \mathbf{R}\beta, \mathbf{R}'\beta' \rangle \, . \tag{2.12}$$

[2] This includes all nearest-neighbor spin and boson Hamiltonians and more general ones.

They contain all the information of the original Hamiltonian and the general unitary transformation $\hat{U}$ defined by $b^\dagger_{\mathbf{R}\alpha} = \sum_{\mathbf{n}} U^\alpha_{\mathbf{Rn}} b^\dagger_{\mathbf{Rn}}$. We have The interaction tensor $\hat{V}$ may possess certain symmetries under the interchange of indices. In particular, for a hermitian Hamiltonian,

$$(T_{\mathbf{R}})^\alpha_\beta = \left[(T_{\mathbf{R}})^\beta_\alpha\right]^*, \tag{2.13}$$

$$(V_{\mathbf{RR}'})^{\alpha\alpha'}_{\beta\beta'} = \left[(V_{\mathbf{RR}'})^{\beta\beta'}_{\alpha\alpha'}\right]^*. \tag{2.14}$$

while, in general,

$$(V_{\mathbf{RR}'})^{\alpha\alpha'}_{\beta\beta'} = (V_{\mathbf{RR}'})^{\alpha'\alpha}_{\beta'\beta}\ , \tag{2.15}$$

may not be true. As the new degrees of freedom have a structure, the two-body CB tensor $\hat{V}$ depends on the precise layout of the two clusters involved in the process, that is,

$$(V_{\mathbf{RR}'})^{\alpha\alpha'}_{\beta\beta'} = (V_{\mathbf{R}'\mathbf{R}})^{\alpha'\alpha}_{\beta'\beta}. \tag{2.16}$$

For clearness purposes, we will use lower (upper) Greek indices in the tensors (2.11) and (2.12) of a general composite particle Hamiltonian to refer to the initial (final) quantum state of the cluster.

The CB Hamiltonian (2.10) can be approached by standard many-body techniques, with the advantage that short-range quantum correlations are contained exactly in the CBs definition. In the following, we introduce a CB product wave function, dubbed CB Gutzwiller, which has been the ansatz used in previous HMFT studies [19, 20, 21].

2.2 Composite boson Gutzwiller approach

The crudest approximation that we can think about is a cluster product wave function or, in other words, a *CB Gutzwiller* wave function,

$$|\Psi\rangle = \prod_{\mathbf{R}} |\Phi_{\mathbf{R}}\rangle = \prod_{\mathbf{R}} \left(\sum_{\mathbf{n}} U^{\mathsf{g}}_{\mathbf{Rn}} b^\dagger_{\mathbf{Rn}} \right) |0\rangle_B. \tag{2.17}$$

The amplitudes $U^{\mathsf{g}}_{\mathbf{Rn}}$ encode the information about the state g referred in the occupation basis $\mathbf{n}$ and will be determined variationally. The minimization of the energy with respect to the variational amplitudes results in a non-linear set of coupled equations that can be cast in matrix form,

$$\sum_{\mathbf{m}} (h_{\mathbf{R}})_{\mathbf{mn}} U^{\mathsf{g}}_{\mathbf{Rm}} = \lambda_{\mathbf{R}} U^{\mathsf{g}}_{\mathbf{Rn}}\ , \tag{2.18}$$

where the parameter $\lambda_{\mathbf{R}}$ is a Lagrange multiplyer associated to the normalization condition, $\sum_{\mathbf{n}}(U^{\mathtt{g}}_{\mathbf{Rn}})^* U^{\mathtt{g}}_{\mathbf{Rn}} = 1$. The lowest eigenvalue and corresponding eigenvector defines $\lambda_{\mathbf{R}}$ and $U^{\mathtt{g}}_{\mathbf{R}}$, respectively.

In general the Hartree Hamiltonian $\hat{h}$ will have an algebraic dependence on the set of variational parameters $\{U^{\mathtt{g}}\}$ given by the different many-body CB terms of the Hamiltonian (2.10). As a consequence, Eq. (2.18) comprises a set of nonlinear equations which is solved iteratively after starting with an initial guess for the amplitudes $U^{\mathtt{g}}_{\mathbf{Rn}}$. Being a variational procedure, the energy decreases at each iteration step, converging to a minimum at selfconsistency. Moreover, as the CB Gutzwiller wave function preserves exactly the physical constraint (2.6), the energy obtained is an upper bound to the exact one. In the limit where the cluster is a single-site, we recover the standard Gutzwiller approximation. The use of clusters as the basic degrees of freedom allows for the description of a wide range of multiple-sublattice phases with a unique wave function.

When treating a uniform system with translational invariance, we may consider all clusters to be equivalent and drop the superlattice site index $\mathbf{R}$ in (2.18). As a consequence, Eq. (2.18) reduces to a single Hartree equation. In this case, the CB Gutzwiller approximation is exactly equivalent to diagonalize the Hamiltonian in a cluster with open boundary conditions (OBC) and a set of self-consistently defined auxiliary fields acting on its borders. Other cluster mean-field approaches have been shown to be equivalent to this approximation [22, 23].

The CB Gutzwiller approach can be understood as a combination of ED and standard mean-field. The standard ED procedure provides information about the thermodynamic limit through a finite-size scaling analysis, whereas the CB Gutzwiller obtains information about the thermodynamic limit through the self-consistently defined mean-fields. Moreover, further finite size scaling analysis is feasible within the CB Gutzwiller approach [19, 23]. However, the sizes reached by this means are usually smaller than in ED, as the auxiliary-fields allow for the explicit breaking of the symmetries of the Hamiltonian and block-simplifications are not possible.

In spite of the crude simplicity of this wave function it permits to access a wide range of different phases characterized by local order parameters (OPs) in an unbiased way, as a unique cluster already contains information about various competing orders. The ground state phase diagram can be mapped out using a thoughtful tiling of the lattice preserving most of the symmetries of the Hamiltonian of study. The borders are determined through the computation of the energy and its derivatives with respect to the control parameters across the transitions. In addition, the value of the OPs

and other physical observables can be computed in a systematic way. In particular, non-vanishing peaks in scattering matrices of the general form,

$$S(\mathbf{q}) \propto \sum_{ij} e^{-\mathrm{i}\mathbf{q}(\mathbf{r}_i-\mathbf{r}_j)} \langle\Psi| \hat{\mathcal{O}}_i^\dagger \hat{\mathcal{O}}_j |\Psi\rangle \tag{2.19}$$

signal different type of orders. For example, when $\hat{\mathcal{O}}_i = a_i^\dagger$, the peaks in (2.19) signal Bose-Einstein condensation (BEC); when $\hat{\mathcal{O}}_i = n_i$, they signal charge density wave order (CDW). Computed with a CB Gutzwiller wave function (2.17), Eq. (2.19) takes the form

$$\begin{aligned} S(\mathbf{q}) \;\propto\; & \sum_{\mathbf{R}} \sum_{i,j\in\mathbf{R}} e^{-\mathrm{i}\mathbf{q}(\mathbf{r}_i-\mathbf{r}_j)} \langle\Phi_{\mathbf{R}}| \hat{\mathcal{O}}_i^\dagger \hat{\mathcal{O}}_j |\Phi_{\mathbf{R}}\rangle \\ & + \sum_{\mathbf{R}\neq\mathbf{R}'} \sum_{i\in\mathbf{R}} \sum_{j\in\mathbf{R}'} e^{-\mathrm{i}\mathbf{q}(\mathbf{r}_i-\mathbf{r}_j)} \langle\Phi_{\mathbf{R}}| \hat{\mathcal{O}}_i^\dagger |\Phi_{\mathbf{R}}\rangle \langle\Phi_{\mathbf{R}'}| \hat{\mathcal{O}}_j |\Phi_{\mathbf{R}'}\rangle \,. \end{aligned} \tag{2.20}$$

Considering a homogeneus CB Gutzwiller wave function, $|\Phi_{\mathbf{R}}\rangle = |\Phi\rangle$, Eq. (2.20) can be approximated by

$$S(\mathbf{q}) \propto \left| \sum_{i\in\square} e^{-\mathrm{i}\mathbf{q}\mathbf{r}_i} \langle\Phi| \hat{\mathcal{O}}_i^\dagger |\Phi\rangle \right|^2 . \tag{2.21}$$

in the thermodynamic limit.

The CB Gutzwiller wave function leads to an explicit breaking of translational symmetry, which should be restored in the thermodynamic limit. Therefore, one cannot draw rigorous conclusions on the order of the phase transitions based solely on a fixed coarse graining. In order to assess the stability of the phases, several coarse grainings must be performed. As the size of the cluster simulated gets larger we get closer to the exact solution in the thermodynamic limit.

2.3 Composite boson Hartree-Bogoliubov approach

The homogeneus CB Gutzwiller wave function has the same variational energy as a *CB Coherent* wave function,

$$|\Psi\rangle = e^{b^\dagger_{\mathbf{K}=\mathbf{0},\mathtt{g}}} |0\rangle_B = \prod_{\mathbf{R}} e^{b^\dagger_{\mathbf{R}\mathtt{g}}} |0\rangle_B \,, \tag{2.22}$$

in the thermodynamic limit. In other words, the amplitudes $\{U^{\mathtt{g}}_{\mathbf{n}}\}$ satisfy the variational equations (2.18). The wave function (2.22) describes a BEC of $\mathtt{g}$ CBs in the $\mathbf{K}=\mathbf{0}$ mode of the superlattice Fourier space, and therefore it does not satisfy the

physical constraint (2.6). Nevertheless, the total density of the system is equal to unity,

$$\frac{1}{M}\sum_{\mathbf{R}}\sum_{\alpha}\langle\Psi|\, b^{\dagger}_{\mathbf{R}\alpha}b_{\mathbf{R}\alpha}\,|\Psi\rangle = 1, \tag{2.23}$$

where M labels the total number of superlattice sites in the system. By relaxing the constraint and imposing it globally we are assuming that the CB local density fluctuations are negligible. Although the wave function (2.22) does not satisfy exactly the physical constraint, the relation with the CB Gutzwiller wave function (2.17) allows us to include quantum fluctuations and compute collective excitations over the ground state self-consistently. With that purpose, we propose a *CB Coherent-Bogoliubov* wave function, which contains a Bogoliubov vacuum of CB quasi-particles orthogonal to the g flavor,

$$|\Psi\rangle = \mathcal{N}\exp\left[z b^{\dagger}_{\mathbf{0},\mathsf{g}} + \sum_{\mathbf{K}}\sum_{\alpha,\beta\neq\mathsf{g}} (Z_{\mathbf{K}})^{\alpha}_{\beta}\;\, b^{\dagger}_{\mathbf{K}\alpha}b^{\dagger}_{-\mathbf{K}\beta}\right]|0\rangle_{B}. \tag{2.24}$$

This Bogoliubov vacuum of CB quasi-particles accounts for the quantum fluctuations of the CB condensate described by the simple CB Coherent wave function. In Eq. (2.24), $z=\sqrt{M}\sigma$ where σ^2 refers to the fraction of CBs belonging to the CB condensate (i.e. the *CB condensate fraction*), and $(Z_{\mathbf{K}})^{\alpha}_{\beta}$ are a set of variational amplitudes. The *condensate* and the *fluctuation* parts of the wave function (2.24) are orthogonal and we can thus rerwite it as a product,

$$|\Psi\rangle = |\Psi_{\mathsf{g}}\rangle \otimes |\Psi_{\mathsf{f}}\rangle, \tag{2.25}$$

where $|\Psi_{\mathsf{g}}\rangle$ refers to the CB coherent ansatz and $|\Psi_{\mathsf{f}}\rangle$ to the CB Bogoliubov ansatz corresponding to the fluctuations of the CB condensate.

With this wave function, we are assuming that the relevant quantum correlations are already contained within the clusters, and that the remaining quantum fluctuations can be described as CB collective quasi-particles, in a similar way as magnons are collective excitations over magnetically ordered ground states. In fact, the Linear Spin Wave approximation (LSWT) is contained in a particular limit of (2.24) when CBs are constructed from one site hard-core bosonic states.

As a consequence of the manifest violation of the physical constraint, this wave function induces mixtures with states belonging to the unphysical subspace. This is a common issue present in all slave-particle theories when treated by mean-field approximations [1, 24, 25]. Nevertheless, when using clusters as the basic degrees of freedom, this mixture is expected to be less severe with increasing cluster sizes, such

that in the limit of very large clusters it might be negligible. Imposing the global constraint (2.23) we obtain a relation among the CB condensate fraction and the collective excitations,

$$\sigma^2 + \frac{1}{M}\sum_{\mathbf{K}}\sum_{\alpha\neq \mathtt{g}} \langle \Psi_{\mathrm{f}}|\, b^{\dagger}_{\mathbf{K}\alpha} b_{\mathbf{K}\alpha}\, |\Psi_{\mathrm{f}}\rangle = 1. \tag{2.26}$$

Due to relation (2.26), the condensate fraction (σ^2) is therefore bounded, $0 \leq \sigma^2 \leq 1$. In the limit where no CB fluctuations are present ($\sigma^2 = 1$), we recover the CB Gutzwiller result, whereas the maximally fluctuating case is characterized by vanishing CB condensate fraction. Therefore, the condensate fraction gives us a measure of the CB fluctuations over a CB Gutzwiller ground state, which contains true correlations together with mixures with unphysical states. Consequently, it qualitatively assesses the validity of the CB coherent ansatz (2.24).

In order to derive the set of self-consistent variational equations that will determine the amplitudes of the CB coherent-Bogoliubov ansatz (2.24), let us first Fourier transform the CB boson operators assuming that the system is uniform in the superlattice,

$$b^{\dagger}_{\mathbf{R}\alpha} = \frac{1}{\sqrt{M}}\sum_{\mathbf{K}} e^{-\mathrm{i}\mathbf{K}\cdot\mathbf{R}}\; b^{\dagger}_{\mathbf{K}\alpha}. \tag{2.27}$$

We can rewrite Hamiltonian (2.10) in the superlattice Fourier space as

$$H^B = \sum_{\mathbf{K}} T^{\alpha}_{\beta} b^{\dagger}_{\mathbf{K}\alpha} b_{\mathbf{K}\beta} + \frac{1}{M}\sum_{\mathbf{K}_1\mathbf{K}_2\mathbf{Q}} (V_{\mathbf{Q}})^{\alpha\alpha'}_{\beta\beta'}\; b^{\dagger}_{\mathbf{K_1}\alpha} b^{\dagger}_{\mathbf{K_2}+\mathbf{Q},\alpha'} b_{\mathbf{K_1}+\mathbf{Q},\beta} b_{\mathbf{K_2}\beta'}, \tag{2.28}$$

where repeated greek indices sum. In Eq. (2.28) we have a assumed a uniform ground state, which implies that $\hat{T}_{\mathbf{R}} = \hat{T}$ and that $\hat{V}_{\mathbf{R}\mathbf{R}'}$ just depends on the distance $|\mathbf{R}'-\mathbf{R}|$. In particular, for a Hamiltonian with terms involving nearest neighbours,

$$(V_{\mathbf{Q}})^{\alpha\alpha'}_{\beta\beta'} = \sum_{\hat{\mathbf{u}}} (V_{\hat{\mathbf{u}}})^{\alpha\alpha'}_{\beta\beta'} e^{-\mathrm{i}\mathbf{Q}\cdot\hat{\mathbf{u}}}, \tag{2.29}$$

where the vector $\hat{\mathbf{u}}$ runs over the primitive vectors of the superlattice, and $(V_{\hat{\mathbf{u}}})^{\alpha\alpha'}_{\beta\beta'} = (V_{-\hat{\mathbf{u}}})^{\alpha'\alpha}_{\beta'\beta}$. Since the CB coherent-Bogoliubov wave function (2.24) can be expressed as a direct product (2.25), the evaluation of the CB Hamiltonian (2.28) and subsequent variational minimization can be done in several steps.

Let us first take the expectation value with respect to the condensate part, which is equivalent to replace $b^{(\dagger)}_{\mathbf{0g}} \to \sqrt{M}\sigma$, and arrange the terms of the CB Hamiltonian by the number of CB bosons orthogonal to $\mathtt{g}$ that they contain,

$$\langle \Psi_{\mathtt{g}}|\, H^B\, |\Psi_{\mathtt{g}}\rangle = H_0 + H_1 + H_2 + H_3 + H_4. \tag{2.30}$$

Since the terms with an odd number of CB operators will automatically vanish when taking the expectation value with $|\Psi_{\mathsf{f}}\rangle$, we can keep the ones that have an even number of CB operators,

$$
\begin{aligned}
H_0 &= M\left[(V_{\mathbf{0}})^{\mathsf{gg}}_{\mathsf{gg}}\sigma^4 + T^{\mathsf{g}}_{\mathsf{g}} - \lambda\right]\sigma^2, && (2.31)\\
H_2 &= \sum_{\mathbf{K}}\left(T^{\alpha}_{\beta} - \lambda\delta_{\alpha\beta}\right) b^{\dagger}_{\mathbf{K}\alpha} b_{\mathbf{K}\beta} \\
&\quad +\sigma^2\sum_{\mathbf{K}}\left[(V_{\mathbf{K}})^{\alpha\mathsf{g}}_{\mathsf{g}\beta} b^{\dagger}_{-\mathbf{K}\alpha} b_{-\mathbf{K}\beta} + (V_{\mathbf{K}})^{\mathsf{g}\alpha}_{\beta\mathsf{g}} b^{\dagger}_{\mathbf{K}\alpha} b_{\mathbf{K}\beta}\right] \\
&\quad +\sigma^2\sum_{\mathbf{K}}\left[(V_{\mathbf{0}})^{\alpha\mathsf{g}}_{\beta\mathsf{g}} b^{\dagger}_{-\mathbf{K}\alpha} b_{-\mathbf{K}\beta} + (V_{\mathbf{0}})^{\mathsf{g}\alpha}_{\mathsf{g}\beta} b^{\dagger}_{\mathbf{K}\alpha} b_{\mathbf{K}\beta}\right] \\
&\quad +\sigma^2\sum_{\mathbf{K}}\left[(V_{\mathbf{K}})^{\alpha\beta}_{\mathsf{gg}} b^{\dagger}_{-\mathbf{K}\alpha} b^{\dagger}_{\mathbf{K}\beta} + (V_{\mathbf{K}})^{\mathsf{gg}}_{\alpha\beta} b_{\mathbf{K}\alpha} b_{-\mathbf{K}\beta}\right], && (2.32)\\
H_4 &= \frac{1}{M}\sum_{\mathbf{K_1K_2Q}} (V_{\mathbf{Q}})^{\alpha\alpha'}_{\beta\beta'} b^{\dagger}_{\mathbf{K_1}\alpha} b^{\dagger}_{\mathbf{K_2}+\mathbf{Q},\alpha'} b_{\mathbf{K_1}+\mathbf{Q},\beta} b_{\mathbf{K_2}\beta'}, && (2.33)
\end{aligned}
$$

where repeated indices sum and greek indices correspond to cluster states orthogonal to g. The constant H_0 contains the free-term of the CB condensate and the interaction with itself; the H_2 term accounts for the interaction of the CB condensate with its collective fluctuations on the orthogonal subspace; and H_4 accounts for the interaction among these collective fluctuations. Taking the expectation value of (2.30) with $|\Psi_{\mathsf{f}}\rangle$ and deriving with respect to the variational parameters is equivalent to mean-field decouple H_4 applying Wick's theorem for bosons [26],

$$
\begin{aligned}
(H_4)_{mf} &= \frac{1}{M}\sum_{\mathbf{KQ}} (V_{\mathbf{Q}-\mathbf{K}})^{\alpha\alpha'}_{\beta\beta'}\left(b^{\dagger}_{\mathbf{K}\alpha} b^{\dagger}_{-\mathbf{K}\alpha'} K^{*}_{-\mathbf{Q}\beta';\mathbf{Q}\beta} + b_{\mathbf{Q}\beta} b_{-\mathbf{Q}\beta'} K_{\mathbf{K}\alpha;-\mathbf{K}\alpha'}\right) \\
&\quad +\frac{1}{M}\sum_{\mathbf{KQ}} (V_{\mathbf{Q}-\mathbf{K}})^{\alpha\alpha'}_{\beta\beta'}\left(b^{\dagger}_{\mathbf{K}\alpha} b_{\mathbf{K}\beta'} P_{\mathbf{Q}\alpha';\mathbf{Q}\beta} + b^{\dagger}_{\mathbf{K}\alpha'} b_{\mathbf{K},\beta} P_{\mathbf{Q}\alpha;\mathbf{Q}\beta'}\right) \\
&\quad +\frac{1}{M}\sum_{\mathbf{KQ}} (V_{\mathbf{0}})^{\alpha\alpha'}_{\beta\beta'}\left(b^{\dagger}_{\mathbf{K}\alpha} b_{\mathbf{K}\beta} P_{\mathbf{Q}\alpha';\mathbf{Q}\beta'} + b^{\dagger}_{\mathbf{K}\alpha'} b_{\mathbf{K}\beta'} P_{\mathbf{Q}\alpha;\mathbf{Q}\beta}\right) && (2.34)
\end{aligned}
$$

obtaining a quadratic mean-field CB Hamiltonian of the form

$$
H^{B}_{mf} = H_0 + H_2 + (H_4)_{mf}. \tag{2.35}
$$

We then diagonalize (2.35) by means of a general Bogoliubov transformation under the self-consistency condition

$$
\begin{aligned}
P_{\mathbf{Q}\alpha;\mathbf{Q}\beta} &= \langle b^{\dagger}_{\mathbf{Q}\alpha} b_{\mathbf{Q}\beta}\rangle, && (2.36)\\
K_{\mathbf{Q}\alpha;-\mathbf{Q}\beta} &= \langle b^{\dagger}_{\mathbf{Q}\alpha} b^{\dagger}_{-\mathbf{Q}\beta}\rangle. && (2.37)
\end{aligned}
$$

The Bogoliubov transformation yields to an eigensystem that determines the variational parameters $\hat{Z}_{\mathbf{K}}$ in (2.24) and the dispersions of the collective excitations over the ground state. The technical details on the Bogoliubov diagonalization are given in Appendix 2.C.

2.3.1 Self-consistent computational procedure

The expansion of the Hamiltonian in CB fluctuations of the CB condensate (2.30) depends on the generic unitary transformation $\hat{U}$, which is determined upon minimization of the expectation value of the potential (2.35) with respect to the condensed CB structure $\{U^{\mathtt{g}}_{\mathbf{m}}\}$. The resulting equations determining $\hat{U}$ can be cast in a Hartree eigensystem equation similar to (2.18), but which now contains additional information about the fluctuations over the CB condensate ($\mathtt{g}$) through its dependance on the condensate fraction (σ^2) and on the *density matrix* (2.36) and *pairing tensor* (2.37). The self-consistent Hartree diagonalization provides the eigenvector defining the structure of the condensed CB ($U^{\mathtt{g}}$) and the corresponding lowest eigenvalue, which is the Lagrange multiplier λ. In addition, it provides a complete set of eigenstates that are orthogonal to the condensed CB ($U^{\alpha},\ \alpha \neq \mathtt{g}$). They define the orthogonal subspace where the Bogoliubov diagonalization will be performed.

We seek for a self-consistent solution of the Hartree matrix, which fixes the unitary transformation $\hat{U}$ and the Langrange multiplier λ; the Bogoliubov eigensystem, that provides the density matrix (2.36) and pairing tensor (2.37) and the quasi-particle dispersions (see Appendix 2.C); and the expectation value of the physical constraint (2.26) that determines the CB condensed fraction (σ^2).

Interestingly, the Linear Spin Wave approximation (LSWT) is recovered within this computational scheme in a certain limit. In particular, when we map hard-core bosons ($S = 1/2$ spins) to one-site CBs (Schwinger bosons). The computation of the spin-wave dispersions is obtained by a truncation of the procedure described above, i.e. not requiring self-consistency. Specifically, the Hartree matrix does not contain CB fluctuations, the condensate fraction is fixed to $\sigma^2 = 1$, and H_4 is neglected in the potential (2.35).

2.4 The composite fermion-boson mapping

Analogously to the CB mapping, we can think about representing the many-body cluster states of a fermionic lattice system by the action of a new set of operators

over a new vacuum. Due to the fermionic statistics, the new set of composite operators will contain composite fermionic and bosonic particles.

As we did in the bosonic case, let us start our derivation by decomposing the original lattice into a perfectly tiled cluster superlattice. The Fock space of the complete system $\mathbb{F}$ is a direct product of the Fock spaces of each cluster $\mathbb{F}_{\mathbf{R}}$, where $\mathbf{R}$ denotes the position of the cluster in the superlattice. The states in $\mathbb{F}_{\mathbf{R}}$ contain the complete set of many-body states up to the maximum number of fermions that the cluster can accommodate. Each cluster Fock space is decomposed into two subspaces with odd and even number of fermions, which are denoted by $\mathbb{F}^o_{\mathbf{R}}$ and $\mathbb{F}^e_{\mathbf{R}}$. Each state of $\mathbb{F}^o_{\mathbf{R}}$ and $\mathbb{F}^e_{\mathbf{R}}$ can be represented by the action of a *composite fermion* (CF) and a *composite boson* (CB) operators, respectively, over the corresponding vacuum,

$$|\mathbf{R}\alpha\rangle \rightarrow a^\dagger_{\mathbf{R}\alpha}|0\rangle_F, \qquad |\mathbf{R}\beta\rangle \rightarrow b^\dagger_{\mathbf{R}\beta}|0\rangle_B, \tag{2.38}$$

where α (β) labels clusters states with an odd (even) number of fermions, respectively. The formal mapping which relates the physical fermionic operators with the new composite particles reads

$$c^\dagger_{j\sigma} = \sum_{\alpha\beta}\langle \mathbf{R}\alpha|c^\dagger_{j\sigma}|\mathbf{R}\beta\rangle\ a^\dagger_{\mathbf{R}\alpha}b_{\mathbf{R}\beta} + \sum_{\alpha\beta}\langle \mathbf{R}\beta|c^\dagger_{j\sigma}|\mathbf{R}\alpha\rangle\ b^\dagger_{\mathbf{R}\beta}a_{\mathbf{R}\alpha}, \quad c_{j\sigma} = (c^\dagger_{j\sigma})^\dagger \tag{2.39}$$

where the site j of the original lattice is contained within the cluster $\mathbf{R}$ after the tiling. Notice that α and β states in the previous matrix elements differ by just one fermion. The CFB mapping (2.39) can be considered as a cluster extension of the Zou-Anderson mapping [12], which is the single-site limit. Similarly to the CB mapping of bosons, the CBs and CFs of the CFB mapping (2.39) must fulfill three conditions: *i)* satisfaction of the physical constraint that defines the physically meaningfull subspace of the enlarged composite particle Fock space,

$$\sum_\alpha a^\dagger_{\mathbf{R}\alpha}a_{\mathbf{R}\alpha} + \sum_\beta b^\dagger_{\mathbf{R}\beta}b_{\mathbf{R}\beta} = 1, \tag{2.40}$$

at each superlattice site $\mathbf{R}$; *ii)* satisfaction of the commutation and anticommutation rules by the CBs and CFs, respectively,

$$\{a^\dagger_{\mathbf{R}\alpha}, a_{\mathbf{R}'\alpha'}\} = \delta_{\alpha,\alpha'}\delta_{\mathbf{R}\mathbf{R}'}, \qquad \{a^\dagger_{\mathbf{R}\alpha}, a^\dagger_{\mathbf{R}'\alpha'}\} = 0, \tag{2.41}$$

$$[b_{\mathbf{R}\beta}, b^\dagger_{\mathbf{R}'\beta'}] = \delta_{\beta\beta'}\delta_{\mathbf{R}\mathbf{R}'}, \qquad [b^\dagger_{\mathbf{R}\beta}, b^\dagger_{\mathbf{R}'\beta'}] = 0, \tag{2.42}$$

and commutation rules among each other,

$$[a_{\mathbf{R}\alpha}, b^\dagger_{\mathbf{R}\beta}] = 0; \tag{2.43}$$

and *iii)* satisfaction of the resolution of the identity,

$$\sum_{\beta} |\mathbf{R}\beta\rangle\langle\mathbf{R}\beta| + \sum_{\alpha} |\mathbf{R}\alpha\rangle\langle\mathbf{R}\alpha| = I. \tag{2.44}$$

The explicit deomonstration of the satisfaction of the original fermionic canonical relations relying on these three conditions is givenn in the Appendix 2.D.

As long as the complete set of bosonic and fermionic cluster states is used, one can map an arbitrary operator acting within a cluster $\mathbf{R}$ to a one-body composite operator of the general form

$$\begin{aligned}\hat{\mathcal{O}}_{\mathbf{R}} &= \sum_{\alpha\alpha'} \langle\mathbf{R}\alpha|\hat{\mathcal{O}}_{\mathbf{R}}|\mathbf{R}\alpha'\rangle a^{\dagger}_{\mathbf{R}\alpha} a_{\mathbf{R}\alpha'} + \sum_{\beta\beta'} \langle\mathbf{R}\beta|\hat{\mathcal{O}}_{\mathbf{R}}|\mathbf{R}\beta'\rangle b^{\dagger}_{\mathbf{R}\beta} b_{\mathbf{R}\beta'} \\ &\quad + \sum_{\alpha\beta} \langle\mathbf{R}\beta|\hat{\mathcal{O}}_{\mathbf{R}}|\mathbf{R}\alpha\rangle b^{\dagger}_{\mathbf{R}\beta} a_{\mathbf{R}\alpha} + \sum_{\alpha\beta} \langle\mathbf{R}\alpha|\hat{\mathcal{O}}_{\mathbf{R}}|\mathbf{R}\beta\rangle a^{\dagger}_{\mathbf{R}\alpha} b_{\mathbf{R}\beta}. \end{aligned} \tag{2.45}$$

The first line applies if the operator $\hat{\mathcal{O}}_{\mathbf{R}}$ preserves the number of fermions, or creates or annihilates an even number of fermions (even number parity). The second line applies if it creates or annihilates an odd number of fermions (odd number parity). Equivalently, any algebraic operator acting on n different clusters will be mapped to a general n-body CFB operator. Analogously as we did in the bosonic case (Sec. 2.1), this recipe allows us to map any many-body fermionic Hamiltonian in terms of the composite particles. The resulting CFB Hamiltonian may contain several terms accounting for the interaction among the composite bosonic and fermionic particles. For the sake of simplicity, let us restrict here to Hamiltonians of the Hubbard type, i.e. that contain a one-body kinetic energy terms and on-site density interactions. In this case, the composite particle Hamiltonian possess a particularly simple expression in terms of CBs and CFs,

$$\begin{aligned} H^{FB} &= \sum_{\mathbf{R}} \left[(T_{\mathbf{R}})^{\alpha}_{\alpha'} \, a^{\dagger}_{\mathbf{R}\alpha} a_{\mathbf{R}\alpha'} + (T_{\mathbf{R}})^{\beta}_{\beta'} \, b^{\dagger}_{\mathbf{R}\beta} b_{\mathbf{R}\beta'} \right] \\ &\quad + \sum_{\langle \mathbf{R}\mathbf{R}' \rangle} \left[(V_{\mathbf{R}\mathbf{R}'})^{\alpha\beta}_{\beta'\alpha'} \, a^{\dagger}_{\mathbf{R}\alpha} b^{\dagger}_{\mathbf{R}'\beta} b_{\mathbf{R}\beta'} a_{\mathbf{R}'\alpha'} + \text{H.c.} \right] \\ &\quad + \sum_{\langle \mathbf{R}\mathbf{R}' \rangle} \left[(V_{\mathbf{R}\mathbf{R}'})^{\alpha\alpha'}_{\beta\beta'} \, a^{\dagger}_{\mathbf{R}\alpha} a^{\dagger}_{\mathbf{R}'\alpha'} b_{\mathbf{R}\beta} b_{\mathbf{R}'\beta'} + \text{H.c.} \right], \end{aligned} \tag{2.46}$$

where repeated greek indices sum and the tensors

$$(T_{\mathbf{R}})^{\eta}_{\eta'} = \langle\mathbf{R}\eta|H^{\square}_{\mathbf{R}}|\mathbf{R}\eta'\rangle, \tag{2.47}$$

$$(V_{\mathbf{R}\mathbf{R}'})^{\zeta\zeta'}_{\eta\eta'} = \langle\mathbf{R}\zeta, \mathbf{R}'\zeta'|H^{\parallel}_{\mathbf{R}\mathbf{R}'}|\mathbf{R}\eta, \mathbf{R}'\eta'\rangle, \tag{2.48}$$

contain all the information about the original Hamiltonian, H. We have used the general labels η, ζ to refer to fermionic or bosonic states indistintinctly in a general basis. We have used the same notation as in the bosonic case (Sec. 2.1) to refer to the intra- and inter-cluster terms. For an hermitian Hamiltonian H, the kinetic tensor $\hat{T}$ and the interaction tensors $\hat{V}$ are symmetric under certain interchange of its indices,

$$(T_{\mathbf{R}})^{\eta}_{\zeta} = \left[(T_{\mathbf{R}})^{\zeta}_{\eta}\right]^* \tag{2.49}$$

$$(V_{\mathbf{R}\mathbf{R}'})^{\zeta\zeta'}_{\eta\eta'} = \left[(V_{\mathbf{R}\mathbf{R}'})^{\eta\eta'}_{\zeta\zeta'}\right]^* . \tag{2.50}$$

The composite particle Hamiltonian (2.46) can be treated by several mean-field schemes. In the following we will describe two, based on a composite particle ansatz that decouples the composite fermionic and bosonic sectors,

$$|\Psi\rangle = |\Psi^F\rangle \otimes |\Psi^B\rangle \, . \tag{2.51}$$

The fermionic sector may be approached by a Slater determinant within the standard Hartree-Fock or Hartree-Fock-Bogoliubov approaches, and the bosonic sector may be approached by the CB coherent or CB Bogoliubov described in Section 2.3. In particular, we will treat the CF sector by a Hartree-Fock-Bogoliubov scheme, and the CB sector either by a CB coherent (2.22), or by a CB coherent without CB condensation (*CB Bogoliubov*). In both cases, we assume that the system is translational invariant and thus we perform a discrete Fourier transform of the composite operators,

$$a^{\dagger}_{\mathbf{R}\alpha} = \frac{1}{\sqrt{M}} \sum_{\mathbf{K}\in BZ} e^{-\mathrm{i}\mathbf{K}\mathbf{R}} a^{\dagger}_{\mathbf{K}\alpha}, \tag{2.52}$$

$$b^{\dagger}_{\mathbf{R}\beta} = \frac{1}{\sqrt{M}} \sum_{\mathbf{K}\in BZ} e^{-\mathrm{i}\mathbf{K}\mathbf{R}} b^{\dagger}_{\mathbf{K}\beta}, \tag{2.53}$$

where M is the number of sites of the hypercubic superlattice of clusters with size L^d. The first Brillouin zone (BZ) is defined in the interval $(-\pi/L, \pi/L]$ in each direction of the hypercubic reciprocal space. Under this transformation, the Hamiltonian (2.46) can be written as

$$\begin{aligned} H^{FB} = & \sum_{\mathbf{K}} \left(T^{\beta}_{\beta'} b^{\dagger}_{\mathbf{K}\beta} b_{\mathbf{K}\beta'} + T^{\alpha}_{\alpha'} a^{\dagger}_{\mathbf{K}\alpha} a_{\mathbf{K}\alpha'} \right) \\ & + \frac{1}{M} \sum_{\mathbf{K_1}\mathbf{K_2}\mathbf{Q}} \left[(V_{\mathbf{Q}})^{\beta\alpha}_{\alpha'\beta'} b^{\dagger}_{\mathbf{K_1},\beta} a^{\dagger}_{\mathbf{K_2}+\mathbf{Q},\alpha} a_{\mathbf{K_1}+\mathbf{Q},\alpha'} b_{\mathbf{K_2},\beta'} + \mathrm{H.c.} \right] \\ & + \frac{1}{M} \sum_{\mathbf{K_1}\mathbf{K_2}\mathbf{Q}} \left[(V_{\mathbf{Q}})^{\alpha\alpha'}_{\beta\beta'} a^{\dagger}_{\mathbf{K_1},\alpha} a^{\dagger}_{\mathbf{K_2}+\mathbf{Q},\alpha'} b_{\mathbf{K_1}+\mathbf{Q},\beta} b_{\mathbf{K_2},\beta'} + \mathrm{H.c.} \right] \end{aligned} \tag{2.54}$$

where repeated Greek indices sum.

2.5 Composite fermion Bogoliubov approach

The composite particle ansatz (2.51) yields to an effective mean-field Hamiltonian that is quadratic in both the fermionic and bosonic sectors and can be diagonalized by two independent fermionic and bosonic Bogoliubov transformations. The two sectors are coupled via self-consistent boson and fermion mean-fields. In other words, by taking partial variations of the expectation value of H^{FB} with respect to the fermion and boson wave functions, the stationary condition implies that $|\Psi^F\rangle$ and $|\Psi^B\rangle$ are eigenfunctions of the effective fermion and boson Hamiltonians,

$$H^F = \langle\Psi^B|\, H^{FB}\, |\Psi^B\rangle\,, \tag{2.55}$$

$$H^B = \langle\Psi^F|\, H^{FB}\, |\Psi^F\rangle\,. \tag{2.56}$$

More precisely, the fermionic sector reads

$$\begin{aligned} H^F &= \sum_{\mathbf{K}} T^{\alpha}_{\alpha'} a^{\dagger}_{\mathbf{K}\alpha} a_{\mathbf{K}\alpha'} \\ &+ \frac{1}{M}\sum_{\mathbf{K},\mathbf{Q}} \Big[(V_{\mathbf{Q}-\mathbf{K}})^{\alpha\beta}_{\beta'\alpha'} a^{\dagger}_{\mathbf{K}\alpha} a_{\mathbf{K}\alpha'} \langle b^{\dagger}_{\mathbf{Q}\beta} b_{\mathbf{Q}\beta'}\rangle + \text{H.c.}\Big] \\ &+ \frac{1}{M}\sum_{\mathbf{K},\mathbf{Q}} \Big[(V_{\mathbf{Q}-\mathbf{K}})^{\alpha\alpha'}_{\beta\beta'} a^{\dagger}_{\mathbf{K}\alpha} a^{\dagger}_{-\mathbf{K}\alpha'} \langle b_{\mathbf{Q}\beta} b_{-\mathbf{Q}\beta'}\rangle + \text{H.c.}\Big]\,, \end{aligned} \tag{2.57}$$

and the bosonic sector is obtained by a counterpart mean-field decoupling,

$$\begin{aligned} H^B &= \sum_{\mathbf{K}} T^{\beta}_{\beta'} b^{\dagger}_{\mathbf{K}\beta} b_{\mathbf{K}\beta'} \\ &+ \frac{1}{M}\sum_{\mathbf{K},\mathbf{Q}} \Big[(V_{\mathbf{Q}-\mathbf{K}})^{\beta\alpha}_{\alpha'\beta'} b^{\dagger}_{\mathbf{K}\beta} b_{\mathbf{K}\beta'} \langle a^{\dagger}_{\mathbf{Q}\alpha} a_{\mathbf{Q}\alpha'}\rangle + \text{H.c.}\Big] \\ &+ \frac{1}{M}\sum_{\mathbf{K},\mathbf{Q}} \Big[(V_{\mathbf{Q}-\mathbf{K}})^{\beta\beta'}_{\alpha\alpha'} b^{\dagger}_{\mathbf{K}\beta} b^{\dagger}_{-\mathbf{K}\beta'} \langle a_{\mathbf{Q}\alpha} a_{-\mathbf{Q}\alpha'}\rangle + \text{H.c.}\Big]\,. \end{aligned} \tag{2.58}$$

The physical constraint implies that one-and-only-one state is allowed per cluster, however, the mean-field decoupling of Eqs. (2.57) and (2.58) leads to wave functions $|\Psi^F\rangle$ and $|\Psi^B\rangle$ which do not preserve the local physical constraint (2.40) exactly. Therefore, we relax it fixing a global constraint of the total composite particle density,

$$\frac{1}{M}\sum_{\mathbf{R}} \left(\sum_{\alpha} \langle a^{\dagger}_{\mathbf{R}\alpha} a_{\mathbf{R}\alpha}\rangle + \sum_{\beta} \langle b^{\dagger}_{\mathbf{R}\beta} b_{\mathbf{R}\beta}\rangle \right) = 1. \tag{2.59}$$

This latter condition is added to the effective bosonic and fermionic Hamiltonians via a unique Lagrange multiplier λ,

$$F^F = H^F - \lambda \sum_{\mathbf{K}} \sum_{\alpha} a^\dagger_{\mathbf{K}\alpha} a_{\mathbf{K}\alpha}, \tag{2.60}$$

$$F^B = H^B - \lambda \sum_{\mathbf{K}} \sum_{\beta} b^\dagger_{\mathbf{K}\beta} b_{\mathbf{K}\beta}. \tag{2.61}$$

When restricting to wave functions preserving the superlattice translational symmetry, the global physical constraint implies a local *on-average* constraint,

$$\sum_{\alpha} \langle a^\dagger_{\mathbf{R}\alpha} a_{\mathbf{R}\alpha} \rangle + \sum_{\beta} \langle b^\dagger_{\mathbf{R}\beta} b_{\mathbf{R}\beta} \rangle = 1, \tag{2.62}$$

for all clusters $\mathbf{R}$. Similarly to the bosonic case, fluctuations of the physical constraint induce mixtures with unphysical states. These unphysical processes are expected to decrease with increasing cluster sizes, vanishing in the infinite size limit. However, increasing sizes entail a combinatorial increase of the computational cost.

One can consider several candidate mean-field reference states. As the Hubbard Hamiltonian (2.54) has a quadratic form in both the bosonic and fermionic sector, we will Bogoliubov diagonalize the fermionic sector by means of a fermionic Bogoliubov diagonalization, whereas the bosonic sector will be either Bogoliubov diagonalized, or approximated by a CB coherent wave function (2.22).

2.5.1 Self-consistent computational procedure

In the first case, we replace the condensed CB by a $c-$number $b^{(\dagger)}_{\mathbf{0},\mathbf{g}} \to \sqrt{M}\sigma$, where σ^2 is the CB *condensate fraction*. Inserting this transformation into Eq.(2.61) and minimizing with respect to the variational amplitudes $U^{\mathbf{g}}$ leads to a Hartree eigensystem, where λ is the lowest eigenvalue, and $U^{\mathbf{g}}$ its corresponding eigenvector,

$$\sum_{\beta'} h_{\beta\beta'} U^{\mathbf{g}}_{\beta'} = \lambda U^{\mathbf{g}}_{\beta}, \tag{2.63}$$

The value of the condensate fraction σ^2 is obtained through the physical constraint,

$$\sigma^2 = 1 - \frac{1}{M} \sum_{\mathbf{K}\alpha} \langle a^\dagger_{\mathbf{K}\alpha} a_{\mathbf{K}\alpha} \rangle. \tag{2.64}$$

In the second approximation, both the fermionic and bosonic sectors are diagonalized by means of the general Bogoliubov transformation.

The convergence of the procedure is determined by the self-consistency between the fermion and boson Hamiltonians and their respective mean-field solutions. In

the scheme where we diagonalize both sectors by coupling the fermionic and bosonic Bogoliubov eigensystems self-consistently, the value of the Lagrange multiplier λ is varied smoothly until the density of composite particles equals one.

2.6 Composite particle gauge structure

Analogously to the different slave-particle formalisms which are present in the literature, the general composite particle Hamiltonians (2.10) and (2.46) possess an emergent lattice gauge structure *ad hoc* to the mapping. Local U(1) gauge transformations on the superlattice,

$$b_{\mathbf{R}\alpha} \rightarrow e^{\mathrm{i}\theta_{\mathbf{R}}}\ b_{\mathbf{R}\alpha}, \tag{2.65}$$

$$a_{\mathbf{R}\alpha} \rightarrow e^{\mathrm{i}\theta_{\mathbf{R}}}\ a_{\mathbf{R}\alpha}, \tag{2.66}$$

leave the composite particle Hamiltonians invariant. This is equivalent to say that the composite particle Hamiltonians conserve the number of composite particles at each superlattice site, which is an implication of the physical constraint. The fluctuations of the physical constraint which lead to the admixture of physical and unphysical states in the mean-field solution are related to the fluctuations of this emergent "artificial" gauge degree of freedom. Although a full integration of the gauge field is desirable, in practice, only a partial integration can be performed [24].

2.7 Summary

In this chapter, we have presented two canonical mappings applicable to bosonic and fermionic lattice systems where the original operators of the lattice are mapped to new *composite* operators representing quantum many-body states of clusters of the lattice. Starting from a perfect tiling of the lattice into a superlattice of clusters, the mappings allow us to reexpress a bosonic or fermionic lattice Hamiltonian in terms of new sets of composite bosonic and fermionic operators that can be treated by standard many-body techniques. We have presented various self-consistent schemes to treat a general composite operator Hamiltonian. Being the new Fock space of composite particles enlarged to the previous one, a physical constraint must be implemented to obtain physically meaningful solutions. Under the impossibility of implementing this constraint exactly, it is satisfied at a mean-field level. Same to any slave-particle

formalism, the physical constraint is indeed related to the artificial lattice gauge structure emerging from the mapping. Violations of the physical constraint are expected to be less severe with increasing sizes of the cluster.

Appendix

2.A Bosonic canonical relations

In this Appendix we prove that the composite boson mapping preserves the original bosonic commutation relations when the composite bosons satisfy conditions (2.4), (2.5) and (2.6).

Let us start by proving that the mapping preserves $[a_i, a_j] = 0$ when both sites are contained in the same cluster, i.e., $i, j \in \mathbf{R}$. Applying directly the mapping (2.3),

$$\begin{aligned}[a_i, a_j] &= \sum_{\alpha,\beta}\sum_{\alpha',\beta'}\langle \mathbf{R}\alpha|a_i|\mathbf{R}\beta\rangle\langle \mathbf{R}\alpha'|a_j|\mathbf{R}\beta'\rangle \\ &\quad\times\left(b^\dagger_{\mathbf{R}\alpha}b_{\mathbf{R}\beta}b^\dagger_{\mathbf{R}\alpha'}b_{\mathbf{R}\beta'} - b^\dagger_{\mathbf{R}\alpha'}b_{\mathbf{R}\beta'}b^\dagger_{\mathbf{R}\alpha}b_{\mathbf{R}\beta}\right). \qquad (2.67)\end{aligned}$$

Applying the canonical commutation relations of the CB bosons we arrive to

$$\begin{aligned}[a_i, a_j] &= \sum_{\alpha,\beta}\sum_{\alpha',\beta'}\langle \mathbf{R}\alpha|a_i|\mathbf{R}\beta\rangle\langle \mathbf{R}\alpha'|a_j|\mathbf{R}\beta'\rangle \\ &\quad\times[b^\dagger_{\mathbf{R}\alpha}\left(\delta_{\alpha',\beta} + b^\dagger_{\mathbf{R}\alpha'}b_{\mathbf{R}\beta}\right)b_{\mathbf{R}\beta'} - b^\dagger_{\mathbf{R}\alpha'}\left(\delta_{\alpha,\beta'} + b^\dagger_{\mathbf{R}\alpha}b_{\mathbf{R}\beta'}\right)b_{\mathbf{R}\beta}], \qquad (2.68)\end{aligned}$$

and using the resolution of the identity,

$$\begin{aligned}[a_i, a_j] &= \sum_{\alpha,\beta}\langle \mathbf{R}\alpha|a_ia_j|\mathbf{R}\beta\rangle b^\dagger_{\mathbf{R}\alpha}b_{\mathbf{R}\beta} - \sum_{\alpha\beta}\langle \mathbf{R}\alpha|a_ja_i|\mathbf{R}\beta\rangle b^\dagger_{\mathbf{R}\alpha}b_{\mathbf{R}\beta} \qquad (2.69)\\ &= \sum_{\alpha\beta}\langle \mathbf{R}\alpha|\,[a_i, a_j]\,|\mathbf{R}\beta\rangle\; b^\dagger_{\mathbf{R}\alpha}b_{\mathbf{R}\beta}, \qquad (2.70)\end{aligned}$$

that vanishes due to the commutation of the original boson operators. When $i \in \mathbf{R}$ and $j \in \mathbf{R}'$ the commutator trivially vanishes, as the CB operators commute for different clusters.

Equivalently, we show that the CB images of the elementary boson operators preserve the boson commutation relation, $[a_i, a^\dagger_j] = \delta_{ij}$. Applying directly the mapping

(2.3),

$$[a_i, a_j^\dagger] = \sum_{\alpha,\beta}\sum_{\alpha',\beta'}\langle \mathbf{R}\alpha|a_i|\mathbf{R}\beta\rangle\langle \mathbf{R}'\alpha'|a_j^\dagger|\mathbf{R}'\beta'\rangle \times \left(b^\dagger_{\mathbf{R}\alpha}b_{\mathbf{R}\beta}b^\dagger_{\mathbf{R}'\alpha'}b_{\mathbf{R}'\beta'} - b^\dagger_{\mathbf{R}'\alpha'}b_{\mathbf{R}'\beta'}b^\dagger_{\mathbf{R}\alpha}b_{\mathbf{R}\beta}\right), \tag{2.71}$$

and using the commutation relations of the CB bosons

$$\begin{aligned}[a_i, a_j^\dagger] = &\sum_{\alpha,\beta}\sum_{\alpha',\beta'}\langle \mathbf{R}\alpha|a_i|\mathbf{R}\beta\rangle\langle \mathbf{R}'\alpha'|a_j^\dagger|\mathbf{R}'\beta'\rangle \\ &\times[b^\dagger_{\mathbf{R}\alpha}\left(\delta_{\alpha',\beta}\delta_{\mathbf{R}\mathbf{R}'} + b^\dagger_{\mathbf{R}'\alpha'}b_{\mathbf{R}\beta}\right)b_{\mathbf{R}'\beta'} \\ &- b^\dagger_{\mathbf{R}'\alpha'}\left(\delta_{\alpha,\beta'}\delta_{\mathbf{R}\mathbf{R}'} + b^\dagger_{\mathbf{R}\alpha}b_{\mathbf{R}'\beta'}\right)b_{\mathbf{R}\beta}].\end{aligned} \tag{2.72}$$

If $i \in \mathbf{R}$ and $j \in \mathbf{R}'$ we can see that $[a_i, a_j^\dagger] = 0$ is trivially satisfied. For the case $i \in \mathbf{R}$, $j \in \mathbf{R}' = \mathbf{R}$, we use the resolution of the identity,

$$[a_i, a_j^\dagger] = \sum_{\alpha,\beta}\langle \mathbf{R}\alpha|a_i a_j^\dagger|\mathbf{R}\beta\rangle b^\dagger_{\mathbf{R}\alpha}b_{\mathbf{R}\beta} - \sum_{\alpha\beta}\langle \mathbf{R}\alpha|a_j^\dagger a_i|\mathbf{R}\beta\rangle b^\dagger_{\mathbf{R}\alpha}b_{\mathbf{R}\beta} \tag{2.73}$$

$$= \sum_{\alpha\beta}\langle \mathbf{R}\alpha|[a_i, a_j^\dagger]|\mathbf{R}\beta\rangle b^\dagger_{\mathbf{R}\alpha}b_{\mathbf{R}\beta}, \tag{2.74}$$

and using orthonormality of the CB basis and the physical constraint,

$$[a_i, a_j^\dagger] = \delta_{ij}\sum_\alpha b^\dagger_{\mathbf{R}\alpha}b_{\mathbf{R}\alpha} = \delta_{ij}. \tag{2.75}$$

We have demonstrated that the mapping is canonical if the resolution of the identity and the physical constraint are satisfied.

2.B Mapping of general bosonic operators

In this Appendix we show how different algebraic functions of the original operators map to a one-, two- and four-body CB operator depending on whether the sites belong to one, two, or four clusters, respectively. In particular we will map a hopping, a density-density interaction, and a ring-exchange term, all of them will be present throughout this thesis. Will always rely on the three conditions which must be satisfied by the CBs.

2.B.1 One-body composite boson operators

Let us start by mapping the hopping operator $a_i^\dagger a_j$ for the case in which it acts inside a cluster, i.e., $i,j \in \mathbf{R}$. Applying directly the mapping (2.3) we obtain

$$a_i^\dagger a_j = \sum_{\alpha\beta}\sum_{\alpha'\beta'} \langle \mathbf{R}\alpha|a_i^\dagger|\mathbf{R}\beta\rangle\langle \mathbf{R}\alpha'|a_j|\mathbf{R}\beta'\rangle b_{\mathbf{R}\alpha}^\dagger b_{\mathbf{R}\beta} b_{\mathbf{R}\alpha'}^\dagger b_{\mathbf{R}\beta'}, \tag{2.76}$$

using the commutation relations of CB bosons

$$a_i^\dagger a_j = \sum_{\alpha\beta}\sum_{\alpha'\beta'} \langle \mathbf{R}\alpha|a_i^\dagger|\mathbf{R}\beta\rangle\langle \mathbf{R}\alpha'|a_j|\mathbf{R}\beta'\rangle \; b_{\mathbf{R}\alpha}^\dagger \left(\delta_{\alpha'\beta} + b_{\mathbf{R}\alpha'}^\dagger b_{\mathbf{R}\beta}\right) b_{\mathbf{R}\beta'}, \tag{2.77}$$

and applying the resolution of the identity and the physical constraint we finally arrive to

$$a_i^\dagger a_j = \sum_{\alpha\beta} \langle \mathbf{R}\alpha|a_i^\dagger a_j|\mathbf{R}\beta\rangle b_{\mathbf{R}\alpha}^\dagger b_{\mathbf{R}\beta}, \tag{2.78}$$

which is a one-body CB operator.

Let us now map the density-density interaction term when it acts within a unique cluster, $n_i n_j = a_i^\dagger a_i a_j^\dagger a_j$, for $i,j \in R$. As we did before, we apply the bare mapping (2.3) directly

$$\begin{aligned} n_i n_j \;\; = \;\; & \sum_{\{\alpha,\beta\}} \langle \mathbf{R}\alpha_1|a_i^\dagger|\mathbf{R}\beta_1\rangle\langle \mathbf{R}\alpha_2|a_i|\mathbf{R}\beta_2\rangle\langle \mathbf{R}\alpha_3|a_j^\dagger|\mathbf{R}\beta_3\rangle\langle \mathbf{R}\alpha_4|a_j|\mathbf{R}\beta_4\rangle \\ & \times b_{\mathbf{R}\alpha_1}^\dagger b_{\mathbf{R}\beta_1} b_{\mathbf{R}\alpha_2}^\dagger b_{\mathbf{R}\beta_2} b_{\mathbf{R}\alpha_3}^\dagger b_{\mathbf{R}\beta_3} b_{\mathbf{R}\alpha_4}^\dagger b_{\mathbf{R}\beta_4}. \end{aligned} \tag{2.79}$$

Then, we commute two CB operators

$$\begin{aligned} n_i n_j \;\; = \;\; & \sum_{\{\alpha,\beta\}} \langle \mathbf{R}\alpha_1|a_i^\dagger|\mathbf{R}\beta_1\rangle\langle \mathbf{R}\alpha_2|a_i|\mathbf{R}\beta_2\rangle\langle \mathbf{R}\alpha_3|a_j^\dagger|\mathbf{R}\beta_3\rangle\langle \mathbf{R}\alpha_4|a_j|\mathbf{R}\beta_4\rangle \\ & \times b_{\mathbf{R}\alpha_1}^\dagger b_{\mathbf{R}\beta_1} b_{\mathbf{R}\alpha_2}^\dagger \left(\delta_{\alpha_3\beta_2} + b_{\mathbf{R}\alpha_3}^\dagger b_{\mathbf{R}\beta_2}\right) b_{\mathbf{R}\beta_3} b_{\mathbf{R}\alpha_4}^\dagger b_{\mathbf{R}\beta_4}, \end{aligned} \tag{2.80}$$

and we apply resolution of the identity and the physical constraint

$$\begin{aligned} n_i n_j \;\; = \;\; & \sum_{\alpha_1\beta_1}\sum_{\alpha_2\beta_3}\sum_{\alpha_4\beta_4} \langle \mathbf{R}\alpha_1|a_i^\dagger|\mathbf{R}\beta_1\rangle\langle \mathbf{R}\alpha_2|a_i a_j^\dagger|\mathbf{R}\beta_3\rangle\langle \mathbf{R}\alpha_4|a_j|\mathbf{R}\beta_4\rangle \\ & \times b_{\mathbf{R}\alpha_1}^\dagger b_{\mathbf{R}\beta_1} b_{\mathbf{R}\alpha_2}^\dagger b_{\mathbf{R}\beta_3} b_{\mathbf{R}\alpha_4}^\dagger b_{\mathbf{R}\beta_4}. \end{aligned} \tag{2.81}$$

Following this procedure repeatedly (use of commutation relations of the CB operators and application of the resolution of identity and the physical constraint) we arrive to the final result

$$n_i n_j = \sum_{\alpha\beta} \langle \mathbf{R}\alpha|a_i^\dagger a_i a_j^\dagger a_j|\mathbf{R}\beta\rangle b_{\mathbf{R}\alpha}^\dagger b_{\mathbf{R}\beta}, \tag{2.82}$$

which is a one-body CB operator.

2.B.2 Two-body composite boson operators

The hopping operator term $a_i^\dagger a_j$ transferring particles from one cluster to a neighbor cluster, $i \in \mathbf{R}$ and $j \in \mathbf{R}' \neq \mathbf{R}$, maps to a two-body CB term. Applying the mapping and normal ordering

$$a_i^\dagger a_j = \sum_{\alpha\beta} \sum_{\alpha'\beta'} \langle \mathbf{R}\alpha | \langle \mathbf{R}'\alpha' | a_i^\dagger a_j | \mathbf{R}\beta \rangle | \mathbf{R}'\beta' \rangle \; b_{\mathbf{R}\alpha}^\dagger b_{\mathbf{R}'\alpha'}^\dagger b_{\mathbf{R}\beta} b_{\mathbf{R}'\beta'}. \tag{2.83}$$

The interaction term $n_i n_j$ between two cluster $i \in \mathbf{R}$ and $j \in \mathbf{R}' \neq \mathbf{R}$, leading to a four-body CB term

$$\begin{aligned} n_i n_j \;\; = \;\; & \sum_{\{\alpha,\beta\}} \langle \mathbf{R}\alpha_1 | a_i^\dagger | \mathbf{R}\beta_1 \rangle \langle \mathbf{R}\alpha_2 | a_i | \mathbf{R}\beta_2 \rangle \langle \mathbf{R}'\alpha_3 | a_j^\dagger | \mathbf{R}'\beta_3 \rangle \langle \mathbf{R}'\alpha_4 | a_j | \mathbf{R}'\beta_4 \rangle \\ & \times b_{\mathbf{R}\alpha_1}^\dagger b_{\mathbf{R}\beta_1} b_{\mathbf{R}\alpha_2}^\dagger b_{\mathbf{R}\beta_2} b_{\mathbf{R}'\alpha_3}^\dagger b_{\mathbf{R}'\beta_3} b_{\mathbf{R}'\alpha_4}^\dagger b_{\mathbf{R}'\beta_4}. \end{aligned} \tag{2.84}$$

Following a similar procedure of commutation, resolution of the identity and application of the physical constraint, we finally arrive to a two-body CB interaction

$$n_i n_j = \sum_{\alpha\beta} \sum_{\alpha'\beta'} \langle \mathbf{R}\alpha | \langle \mathbf{R}'\alpha' | a_i^\dagger a_i a_j^\dagger a_j | \mathbf{R}\beta \rangle | \mathbf{R}'\beta' \rangle b_{\mathbf{R}\alpha}^\dagger b_{\mathbf{R}'\alpha'}^\dagger b_{\mathbf{R}\beta} b_{\mathbf{R}'\beta'}. \tag{2.85}$$

We have demonstrated that both the hopping operator and the density-density interaction within a cluster map to a one-body CB operator. Furthermore, we showed that when these operators act between neighbor clusters they are mapped into two-body CB operators.

2.B.3 Four-body composite boson operators

The ring-exchange term acting on a plaquette $\langle i,j,k,l \rangle$ which lies between four different clusters, $i \in \mathbf{R}_1,\ j \in \mathbf{R}_2,\ k \in \mathbf{R}_3$ and $l \in \mathbf{R}_4$, is directly mapped to a four-body CB operator,

$$\begin{aligned} a_i^\dagger a_j a_k^\dagger a_l \;\; = \;\; & \sum_{\{\alpha,\beta\}} \langle \mathbf{R}_1, \alpha_1 | a_i^\dagger | \mathbf{R}_1, \beta_1 \rangle \langle \mathbf{R}_2, \alpha_2 | a_j | \mathbf{R}_2, \beta_2 \rangle \\ & \times \langle \mathbf{R}_3, \alpha_3 | a_k^\dagger | \mathbf{R}_3, \beta_3 \rangle \langle \mathbf{R}_4, \alpha_4 | a_l | \mathbf{R}_4, \beta_4 \rangle \\ & \times b_{\mathbf{R}_1\alpha_1}^\dagger b_{\mathbf{R}_2\alpha_2}^\dagger b_{\mathbf{R}_3\alpha_3}^\dagger b_{\mathbf{R}_4\alpha_4}^\dagger b_{\mathbf{R}_1\beta_1} b_{\mathbf{R}_2\beta_2} b_{\mathbf{R}_3\beta_3} b_{\mathbf{R}_4\beta_4}, \end{aligned} \tag{2.86}$$

which can be rearranged as,

$$\begin{aligned} a_i^\dagger a_j a_k^\dagger a_l \;\; = \;\; & \sum_{\{\alpha,\beta\}} \langle \mathbf{R}_1, \alpha_1; \mathbf{R}_2, \alpha_2; \mathbf{R}_3, \alpha_3; \mathbf{R}_4, \alpha_4 | \\ & a_i^\dagger a_j a_k^\dagger a_l | \mathbf{R}_1, \beta_1; \mathbf{R}_2, \beta_2; \mathbf{R}_3, \beta_3; \mathbf{R}_4, \beta_4 \rangle \\ & \times b_{\mathbf{R}_1\alpha_1}^\dagger b_{\mathbf{R}_2\alpha_2}^\dagger b_{\mathbf{R}_3\alpha_3}^\dagger b_{\mathbf{R}_4\alpha_4}^\dagger b_{\mathbf{R}_1\beta_1} b_{\mathbf{R}_2\beta_2} b_{\mathbf{R}_3\beta_3} b_{\mathbf{R}_4\beta_4}, \end{aligned} \tag{2.87}$$

that is a four-body CB term.

2.C General Bogoliubov transformation

A general symmetry-preserving Bogoliubov transformation for quadratic Hamiltonians has the form [26],

$$\gamma^{\dagger}_{\mathbf{K}\eta} = \sum_{\eta'} X^{\mathbf{K}}_{\eta'\eta}\, p^{\dagger}_{\mathbf{K}\eta'} + \varepsilon \sum_{\eta'} Y^{\mathbf{K}}_{\eta'\eta}\, p_{-\mathbf{K}\eta'}, \tag{2.88}$$

where the operators $(p^{\dagger}_{\mathbf{K}\eta}, p_{\mathbf{K}\eta})$ refer to fermions ($\varepsilon = +1$) or bosons ($\varepsilon = -1$). Accordingly, the η labels either CF states α or CB states β. The amplitudes X and Y are obtained by solving the self-consistent matrix eigensystem of the form [26],

$$\begin{pmatrix} h^{\mathbf{K},\mathbf{K}} & \Delta^{\mathbf{K},-\mathbf{K}} \\ \varepsilon(\Delta^{-\mathbf{K},\mathbf{K}})^* & \varepsilon(h^{-\mathbf{K},-\mathbf{K}})^* \end{pmatrix} \begin{pmatrix} X^{\mathbf{K}} & (Y^{\mathbf{K}})^* \\ Y^{\mathbf{K}} & (X^{\mathbf{K}})^* \end{pmatrix} = \Omega^{\mathbf{K}} \begin{pmatrix} X^{\mathbf{K}} & (Y^{\mathbf{K}})^* \\ Y^{\mathbf{K}} & (X^{\mathbf{K}})^* \end{pmatrix} \tag{2.89}$$

where the positive eigenvalues of the diagonal matrix $\Omega^{\mathbf{K}} = \mathrm{Diag}(w^{\mathbf{K}}, -w^{\mathbf{K}})$ will determine the fermionic (bosonic) quasi-particle excitation dispersions. The matrix elements are straightforwardly obtained by identifying the grand canonical composite particle potentials given in (2.60) and (2.61) with the general expression

$$\begin{aligned} F &= \sum_{\mathbf{K}\eta\eta'} \left(h^{\mathbf{K},\mathbf{K}}_{\eta\eta'} p^{\dagger}_{\mathbf{K}\eta} p_{\mathbf{K}\eta'} + (h^{-\mathbf{K},-\mathbf{K}}_{\eta\eta'})^* p^{\dagger}_{-\mathbf{K}\eta} p_{-\mathbf{K}\eta'} \right) \\ &\quad + \sum_{\mathbf{K}\eta\eta'} \left(\Delta^{\mathbf{K},-\mathbf{K}}_{\eta\eta'} p^{\dagger}_{\mathbf{K}\eta} p^{\dagger}_{-\mathbf{K}\eta'} + (\Delta^{-\mathbf{K},\mathbf{K}}_{\eta'\eta})^* p_{-\mathbf{K}\eta} p_{\mathbf{K}\eta'} \right). \end{aligned} \tag{2.90}$$

The vacuum of the quasi-particles $\{\gamma^{\dagger}_{\mathbf{K}\eta}, \gamma_{\mathbf{K}\eta}\}$ is a coherent wave function of the form [26],

$$|\Psi\rangle = \exp\left[(Z_{\mathbf{K}})^{\eta}_{\eta'} p^{\dagger}_{\mathbf{K}\eta} p^{\dagger}_{-\mathbf{K}\eta'} \right] |0\rangle\,, \tag{2.91}$$

where repeated indices sum, $\hat{Z} = (X^{\dagger})^{-1} Y^{\dagger}$ and $|0\rangle$ is the vacuum of the composite particles $\{p^{\dagger}_{\mathbf{R}\eta}, p_{\mathbf{R}\eta}\}$. Upon inversion of the Bogoliubov transformation, we obtain the normal and pairing tensors

$$P_{\mathbf{K}\eta;\mathbf{K}\eta'} = \langle p^{\dagger}_{\mathbf{K}\eta} p_{\mathbf{K}\eta'} \rangle = \sum_{\zeta} Y^{\mathbf{K}}_{\eta\zeta} (Y^{\mathbf{K}}_{\eta'\zeta})^*, \tag{2.92}$$

$$K_{\mathbf{K}\eta;-\mathbf{K}\eta'} = \langle p^{\dagger}_{\mathbf{K}\eta} p^{\dagger}_{-\mathbf{K}\eta'} \rangle = \sum_{\zeta} Y^{\mathbf{K}}_{\eta\zeta} (X^{\mathbf{K}}_{\eta'\zeta})^*, \tag{2.93}$$

where we have used the normalized expectation value, $\langle \hat{O} \rangle = \langle \Psi | \hat{O} | \Psi \rangle \,/\, \langle \Psi | \Psi \rangle$. The density matrix is hermitian, $\hat{P} = \hat{P}^{\dagger}$, and that the pairing tensor is symmetric (anti-symmetric), $K_{\mathbf{Q}\alpha;-\mathbf{Q}\beta} = -\varepsilon K_{-\mathbf{Q}\beta;\mathbf{Q}\alpha}$ for bosons (fermions).

2.D Fermionic canonical relations

Let us now explore the conditions that should be fulfilled by transformation (2.39) in order to preserve the canonical fermionic anticommutation relations, $\{c_{i\sigma}, c^{\dagger}_{j\sigma'}\} = \delta_{ij}\delta_{\sigma\sigma'}$. For $i, j \in \mathbf{R}$, we insert the transformation (2.39) into the commutator and obtain,

$$\begin{aligned}
\{c_{i\sigma}, c^{\dagger}_{j\sigma'}\} &= \sum_{\alpha\alpha'}\sum_{\beta'}\langle \mathbf{R}\alpha|c_{i\sigma}|\mathbf{R}\beta'\rangle\langle \mathbf{R}\beta'|c^{\dagger}_{j\sigma'}|\mathbf{R}\alpha'\rangle\ a^{\dagger}_{\mathbf{R}\alpha}a_{\mathbf{R}\alpha'} \\
&+ \sum_{\beta\beta'}\sum_{\alpha'}\langle \mathbf{R}\beta|c_{i\sigma}|\mathbf{R}\alpha'\rangle\langle \mathbf{R}\alpha'|c^{\dagger}_{j\sigma'}|\mathbf{R}\beta'\rangle\ b^{\dagger}_{\mathbf{R}\beta}b_{\mathbf{R}\beta'} \\
&+ \sum_{\alpha\alpha'}\sum_{\beta'}\langle \mathbf{R}\alpha|c^{\dagger}_{j\sigma'}|\mathbf{R}\beta'\rangle\langle \mathbf{R}\beta'|c_{i\sigma}|\mathbf{R}\alpha'\rangle\ a^{\dagger}_{\mathbf{R}\alpha}a_{\mathbf{R}\alpha'} \\
&+ \sum_{\beta\beta'}\sum_{\alpha'}\langle \mathbf{R}\beta|c^{\dagger}_{j\sigma'}|\mathbf{R}\alpha'\rangle\langle \mathbf{R}\alpha'|c_{i\sigma}|\mathbf{R}\beta'\rangle\ b^{\dagger}_{\mathbf{R}\beta}b_{\mathbf{R}\beta'}. \qquad (2.94)
\end{aligned}$$

where we have used the commutation relations (2.41), (2.42), and applied the physical constraint (2.40). Using the resolution of the identity (2.44), and taking into account that the matrix elements $\langle \mathbf{R}\alpha|c^{\dagger}_{j\sigma}|\mathbf{R}\alpha'\rangle$, $\langle \mathbf{R}\alpha|c_{j\sigma}|\mathbf{R}\alpha'\rangle$, $\langle \mathbf{R}\alpha|c^{\dagger}_{j\sigma}|\mathbf{R}\alpha'\rangle$ and $\langle \mathbf{R}\beta|c_{j\sigma}|\mathbf{R}\beta'\rangle$ vanish, equation (2.94) reduces to

$$\begin{aligned}
\{c_{i\sigma}, c^{\dagger}_{j\sigma'}\} &= \sum_{\alpha\alpha'}\langle \mathbf{R}\alpha|\{c_{i\sigma}, c^{\dagger}_{j\sigma'}\}|\mathbf{R}\alpha'\rangle a^{\dagger}_{\mathbf{R}\alpha}a_{\mathbf{R}\alpha'} \\
&+ \sum_{\beta\beta'}\langle \mathbf{R}\beta|\{c_{i\sigma}, c^{\dagger}_{j\sigma'}\}|\mathbf{R}\beta'\rangle b^{\dagger}_{\mathbf{R}\beta}b_{\mathbf{R}\beta'}, \qquad (2.95)
\end{aligned}$$

and, applying the fermionic commutation rules of the original fermions,

$$\{c_{i\sigma}, c^{\dagger}_{j\sigma'}\} = \delta_{i,j}\delta_{\sigma,\sigma'}\left(\sum_{\alpha} a^{\dagger}_{\mathbf{R}\alpha}a_{\mathbf{R}\alpha} + \sum_{\beta} b^{\dagger}_{\mathbf{R}\beta}b_{\mathbf{R}\beta}\right). \qquad (2.96)$$

Applying the physical constraint (2.40), we recover the fermionic anticommutation rules. The anticommutation relation $\{c_{i\sigma}, c^{\dagger}_{j\sigma'}\} = 0$ for $i \in \mathbf{R}, j \in \mathbf{R}' \neq \mathbf{R}$ is trivially satisfied by using the commutation relations (2.41), (2.42) and (2.43).

2.E Mapping a general fermionic operator

We will exemplify be mapping the hopping term when it is acting within a cluster. Applying directly the mapping (2.39), we arrive to

$$\begin{aligned}
c^{\dagger}_{i\sigma}c_{j\sigma} &= \sum_{\alpha\beta}\left(\langle\alpha|\, c^{\dagger}_{i\sigma}\,|\beta\rangle\, a^{\dagger}_{\alpha}b_{\beta} + \langle\beta|\, c^{\dagger}_{i\sigma}\,|\alpha\rangle\, b^{\dagger}_{\beta}a_{\alpha}\right) \\
&\times \sum_{\alpha'\beta'}\left(\langle\alpha'|\, c_{j\sigma}\,|\beta'\rangle\, a^{\dagger}_{\alpha'}b_{\beta'} + \langle\beta'|\, c_{j\sigma}\,|\alpha'\rangle\, b^{\dagger}_{\beta'}a_{\alpha'}\right). \qquad (2.97)
\end{aligned}$$

Applying the physical constraint, we are left with

$$\begin{aligned} c_{i\sigma}^{\dagger} c_{j\sigma} &= \sum_{\alpha\beta} \sum_{\alpha'\beta'} \langle\alpha|\, c_{i\sigma}^{\dagger}\, |\beta\rangle \, \langle\beta'|\, c_{j\sigma}\, |\alpha'\rangle \, a_{\alpha}^{\dagger} b_{\beta} b_{\beta'}^{\dagger} a_{\alpha'} \\ &\quad + \sum_{\alpha\beta} \sum_{\alpha'\beta'} \langle\beta|\, c_{i\sigma}^{\dagger}\, |\alpha\rangle \, \langle\alpha'|\, c_{j\sigma}\, |\beta'\rangle \, b_{\beta}^{\dagger} a_{\alpha} a_{\alpha'}^{\dagger} b_{\beta'} \end{aligned} \tag{2.98}$$

Applying the commutation relations of the CBs and CFs,

$$\begin{aligned} c_{i\sigma}^{\dagger} c_{j\sigma} &= \sum_{\alpha\beta\alpha'} \langle\alpha|\, c_{i\sigma}^{\dagger}\, |\beta\rangle \, \langle\beta|\, c_{j\sigma}\, |\alpha'\rangle \, a_{\alpha}^{\dagger} a_{\alpha'} \\ &\quad + \sum_{\alpha\beta\beta'} \langle\beta|\, c_{i\sigma}^{\dagger}\, |\alpha\rangle \, \langle\alpha|\, c_{j\sigma}\, |\beta'\rangle \, b_{\beta}^{\dagger} b_{\beta'} \end{aligned} \tag{2.99}$$

and using the resolution of the identity, $\sum_{\alpha} |\alpha\rangle \langle\alpha| = 1 - \sum_{\beta} |\beta\rangle \langle\beta|$, and the fact that that the matrix elements $\langle\alpha|\, c_{i\sigma}^{(\dagger)}\, |\alpha'\rangle = 0 = \langle\beta|\, c_{i\sigma}^{(\dagger)}\, |\beta'\rangle$,

$$c_{i\sigma}^{\dagger} c_{j\sigma} = \sum_{\alpha} \langle\alpha|\, c_{i\sigma}^{\dagger} c_{j\sigma}\, |\alpha\rangle \, a_{\alpha}^{\dagger} a_{\alpha} + \sum_{\beta} \langle\beta|\, c_{i\sigma}^{\dagger} c_{j\sigma}\, |\beta\rangle \, b_{\beta}^{\dagger} b_{\beta}. \tag{2.100}$$

The Hubbard on-site interaction can be mapped in the same way, applying repeatedly the process of proyecting out unphysical states by using the physical constraint (2.40), using the commutation relations (2.41), (2.42) and (2.43) and the resolution of the identity (2.44).

Chapter 3

Hard-core bosons with frustrated ring-exchange

In this Chapter we study the zero temperature phase diagram of two-dimensional hard-core bosons on a square lattice with nearest neighbour and plaquette (ring-exchange) hoppings, at arbitrary densities, by means of the CB Gutzwiller ansatz. After reviewing the results obtained within the classical approximation (or CB Gutzwiller 1×1) we use 2×2 and 4×4 clusters and show how the use of a simple cluster product wave function allows us to access several solid and superfluid phases both in the frustrated and unfrustrated regimes. In particular, in the frustrated regime, we find a rich phase diagram where exotic states with nonzero chirality emerge. Among them, novel insulating phases characterized by nonzero bond-chirality and plaquette order are found over a large region of the parameter space. In the unfrustrated regime, the CB Gutzwiller approach improves over the standard mean-field treatment, as it is able to capture the transition from a superfluid to a valence bond state upon increasing the strength of the ring-exchange term, in qualitative agreement with quantum Monte Carlo results.

3.1 The J-K model

In quantum systems multi-particle exchange competing interactions often play an important role in establishing complex thermodynamic phases with unconventional orders [27]. Those interactions are known to be relevant in certain bosonic and fermionic systems, such as solid ^{4}He and ^{3}He [28]. In particular, four-spin ring exchange processes have been argued to be necessary in explaining magnetic excitations in cuprate high-T_c superconductors [29]. Moreover, others claim that they can be essential in understanding the pseudogap phase in the cuprates.

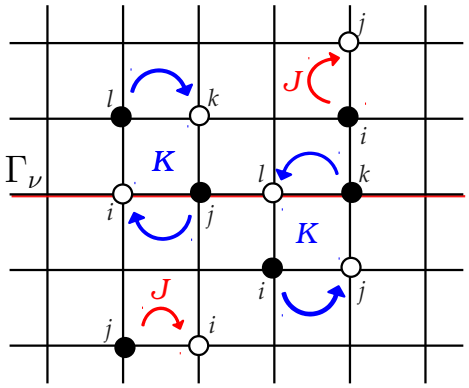

Figure 3.1: Graphical representation of the interaction terms in the J-K Hamiltonian. Filled circles stand for initial state and empty circles for the final state after a single-boson hopping of magnitude J or a ring-exchange process of magnitude K. The ring-exchange is a two-boson hopping from opposite corners of a plaquette to the other two. This latter process preserves the total number of bosons in every line and column of the lattice (see text). In the frustrated regime ($K > 0$), it favors bond-chiral order.

Different kinds of ring-exchange interactions have been proposed in the literature. In the present chapter we are interested in a particular ring-exchange process competing with a single-particle kinetic energy term. We investigate the quantum phase diagram of the so-called J-K model defined by [30, 31]

$$H = -J \sum_{\langle ij \rangle} \hat{B}_{ij} + K \sum_{\langle ijkl \rangle} \hat{P}_{ijkl} - \mu \sum_j n_j, \tag{3.1}$$

where $n_j = a_j^\dagger a_j$ is the density operator, and

$$\hat{B}_{ij} = a_i^\dagger a_j + a_j^\dagger a_i, \tag{3.2}$$

$$\hat{P}_{ijkl} = a_i^\dagger a_k^\dagger a_j a_l + a_l^\dagger a_j^\dagger a_k a_i, \tag{3.3}$$

are the hopping and plaquette operators written in terms of creation, $a_j^\dagger$, and annihilation, a_j, hard-core boson operators at site j of a square lattice with $L_x \times L_y$ sites. The nearest-neighbor hopping amplitude is $J > 0$, μ is the chemical potential controlling the density of the system, and K is the strength of the ring-exchange process where two hard-core bosons on (diagonally) opposite corners of a plaquette $\langle ijkl \rangle$ hop simultaneously to the other two corners, as schematically represented in Fig. 3.1. The J-K model (3.1) can be equivalently written as an (easy-plane) XY

model with a four-spin interaction, via the Matsubara-Matsuda transformation [32],

$$\begin{aligned} H &= -2J\sum_{\langle ij\rangle}\left(S_i^xS_j^x+S_i^yS_j^y\right)-\mu\sum_j\left(S_j^z+\frac{1}{2}\right) \\ &\quad +2K\sum_{\langle ijkl\rangle}(S_i^xS_j^xS_k^xS_l^x+S_i^yS_j^yS_k^yS_l^y+S_i^xS_j^xS_k^yS_l^y \\ &\qquad +S_i^yS_j^yS_k^xS_l^x+S_i^yS_j^xS_k^xS_l^y+S_i^xS_j^yS_k^yS_l^x \\ &\qquad -S_i^xS_j^yS_k^xS_l^y-S_i^yS_j^xS_k^yS_l^x), \end{aligned} \tag{3.4}$$

where $S_j^x=(S_j^+ + S_j^-)/2$ and $S_j^y=(S_j^+ - S_j^-)/2\mathrm{i}$.

The J-K model is not $SU(2)$ invariant, as it is the case of the J-Q [20, 33] and related ring-exchange models [34], but displays a lower global $U(1)$ symmetry. Moreover, for $J=0$, the J-K model has $d=1$ $U(1)$ gauge-like symmetries [35], a total of L_x+L_y unitary operators

$$\hat{\mathcal{O}}_\nu = e^{\mathrm{i}\phi\sum_{j\in\Gamma_\nu}n_j} \tag{3.5}$$

where Γ_ν represents any horizontal or vertical line of the lattice, of length L_x or L_y, respectively (see Fig. 3.1). These $d=1$ symmetries, leading to dimensional reduction [35], constrain the dynamics of the model, as already indicated for a soft-core bosonic version [36], and leads to stripe-like correlations. This K-only model

$$H_K = K\sum_{\langle ijkl\rangle}\hat{P}_{ijkl}, \tag{3.6}$$

also displays a chiral symmetry, with a unitary operator

$$\mathcal{C} = e^{\mathrm{i}\frac{\pi}{2}\sum_{j\in A}n_j} \tag{3.7}$$

that anti-commutes with H_K, and where the sum is performed over sites j of one of the disjoint sublattices A of the original bipartite lattice. This, in turn, implies that the eigenvalue spectrum of H_K is symmetric around zero with the operator $\mathcal{C}$ connecting the ground state of H_K with that of H_{-K}, i.e.,

$$|\Psi_0(-K)\rangle = \mathcal{C}|\Psi_0(K)\rangle. \tag{3.8}$$

This means that correlation functions involving density operators are trivially related. For example,

$$\langle\Psi_0(K)|n_in_j|\Psi_0(K)\rangle = \langle\Psi_0(-K)|n_in_j|\Psi_0(-K)\rangle, \tag{3.9}$$

with the remarkable consequence that long-range order in any density correlation function is independent of the sign of K. One can show that the Hamiltonian H_K has a zero energy eigenspace that can be exactly determined by all those tilings of the lattice with plaquette configurations that exclude the two (out of sixteen) involving only two particles occupying opposite sites of a diagonal. This eigenspace is massively degenerate.

It is interesting to remark that H_K is invariant under transmutation of exchange statistics. This means that one can write H_K in terms of hard-core *anyons* [10] (which includes spinless fermions when the statistical angle is π) and the resulting eigenspectrum remains invariant. The origin of this invariance is, precisely, the existence of the $d = 1$ gauge-like symmetries mentioned above.

For $K > 0$, the ring exchange term dynamically frustrates the usual hopping J. This fact is at the root of the sign problem encountered in quantum Monte Carlo (QMC) simulations of the model. The J-K model has been studied by QMC techniques in the unfrustrated region ($K < 0$), at half filling (μ=0) [30] and away from half filling [31]. These studies have been motivated by the proposal of a new gapless Bose liquid phase dubbed exciton Bose liquid [36]. In addition, the frustrated region ($K > 0$) has been explored at half filling by a semiclassical approximation [37] revealing the emergence of a bond-chiral superfluid (CSF) phase at $K \geq 2$ characterized by nonvanishing condensate and superfluid densities and a nonzero bond-chirality.

In the present Chapter, we determine the quantum phase diagram of the J-K model (3.1) in the frustrated regime of the ring-exchange interaction ($K > 0$) by means of the CB Gutzwiller ansatz using clusters of size 1×1, 2×2 and 4×4. As discussed in Chapter 2, 1×1 is no other but the classical approximation or the standard mean-field. When using clusters larger than a single site, $L \times L$ CB Gutzwiller allows for the existence of solid phases with bond and plaquette orders which cannot be accounted for by the classical approximation.

We obtain various superfluid and solid phases, some of them characterized by the presence of bond-chiral order. In the frustrated regime ($K > 0$), we find a conventional uniform superfluid (SF) and fully occupied (FO) or empty (VAC) phases, as well as a less conventional bond-chiral superfluid (CSF) and two novel insulating valence bond-chiral solid phases (CVBS$_\rho$) at densities $\rho = 1/2$ and $\rho = 5/8$. The latter are characterized by an alternating pattern of the expectation values of the hopping (3.2), plaquette (3.3), and bond-chiral operators defined below. Contrary to other chiral fluid or solid phases [38, 39], the bond-chiral phases encountered here do

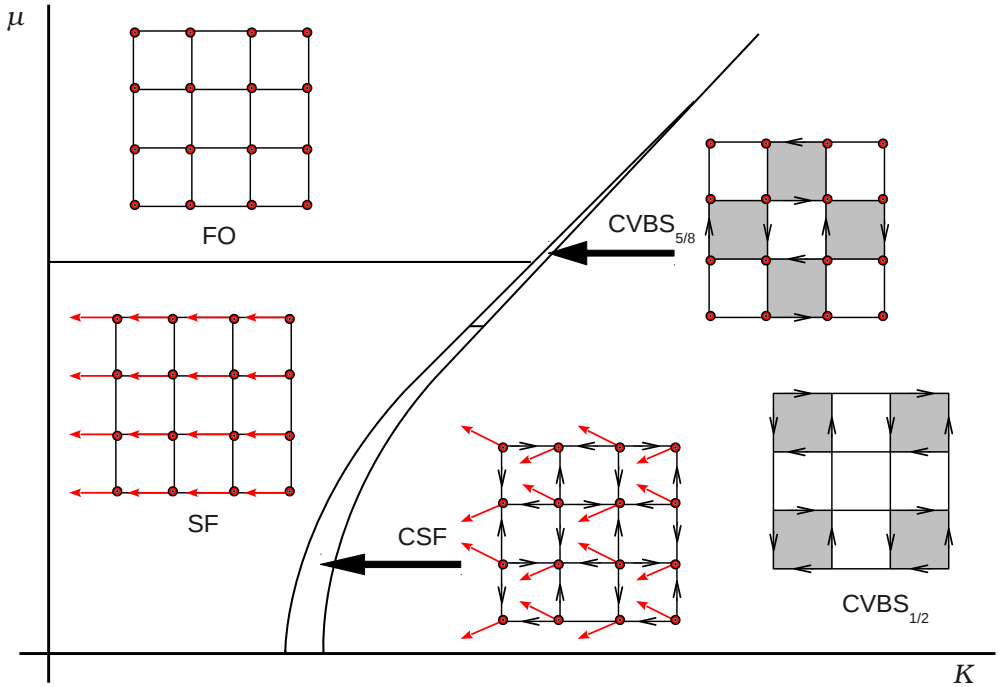

Figure 3.2: Schematic representation of the superfluid and solid phases obtained by means of the CB Gutzwiller 4×4 for the J-K model in the frustrated regime ($K \geq 0$) and with an external chemical potential ($\mu \geq 0$). Phases are pictorially represented in the spin language: filled red arrows indicate the x-y projection of the expectation value of the spin operator $\langle \mathbf{S} \rangle$ at each site, while dots indicate the projection along the z-axis. Empty black arrows along the bonds of the lattice indicate the bond-chirality. The bosonic language is utilized to name the phases (see text). Shaded and white plaquettes correspond to the alternating strength pattern of the plaquette operator characteristic of the CVBS$_\rho$ phases. The phase diagram is symmetric with respect to the $\mu = 0$ line due to particle-hole symmetry. Under this symmetry, the fully occupied region (FO) transforms onto the vacuum of hard-core bosons.

not develop spontaneous loop currents. Instead, they form *source-and-drain* patterns, as it is shown schematically in Figure 3.2.

Studying how quantum phases evolve as the size of the clusters increases allows us to assess the stability of the solution obtained in the previous steps. As an example, the stability of the CSF phase obtained within the classical approximation reduces to a region between the uniform superfluid and the new half filled CVBS$_{1/2}$ phase when computed with clusters of size 2×2. Moreover, a novel CVBS$_{5/8}$ phase of density $\rho = 5/8$ emerges when clusters of size 4×4 are utilized, thus reducing the region of stability of the CSF phase. We cannot rule out the appearance of new commensurate

CVBS$_\rho$ phases, with even larger characteristic correlation length, when larger clusters are used.

3.2 Classical approximation

As a first approach to the phase diagram of the Hamiltonian (3.1), we study in this section the ground state phases within the classical limit. In this limit, the $SU(2)$ spin operator $\mathbf{S}_j = \left(S_j^x, S_j^y, S_j^z\right)$ can be approximated by a classical spin vector, that is,

$$\vec{S}_j = S\left(\sin\theta_j \cos\phi_j, \sin\theta_j \sin\phi_j, \cos\theta_j\right). \tag{3.10}$$

Applying this approximation to the Hamiltonian (3.4), the classical energy (having fixed $J = 1$) is a function of the classical spin angles $\{\theta_j, \phi_j\}$,

$$\begin{aligned} \mathcal{E} &= -2S^2 \sum_{\langle ij \rangle} \sin\theta_i \sin\theta_j \cos(\phi_i - \phi_j) - \mu \sum_j \left(S\cos\theta_j + \frac{1}{2}\right) \\ &\quad +2KS^4 \sum_{\langle ijkl \rangle} \sin\theta_i \sin\theta_j \sin\theta_k \sin\theta_l \cos(\phi_i - \phi_j + \phi_k - \phi_l). \end{aligned} \tag{3.11}$$

For $S = 1/2$, the case of interest here, the energy (3.11) can be equivalently obtained by taking the expectation value of Hamiltonian (3.1) with a product wave function in which the spins of the lattice are in a Bloch sphere representation [40],

$$|\Psi_0\rangle = \prod_j \left[\sin\left(\frac{\theta_j}{2}\right) e^{\mathrm{i}\frac{\phi_j}{2}} |\downarrow\rangle + \cos\left(\frac{\theta_j}{2}\right) e^{-\mathrm{i}\frac{\phi_j}{2}} |\uparrow\rangle\right]. \tag{3.12}$$

By virtue of the Matsubara-Matsuda mapping, the bosonic counterpart is straightforwardly obtained by replacing $|\uparrow\rangle \rightarrow |1\rangle$ and $|\downarrow\rangle \rightarrow |0\rangle$. Therefore, minimizing expression (3.11) with respect to the variational parameters $\{\theta_j, \phi_j\}$ leads to the classical solution or, equivalently, to a variational approximation with the trial wave function (3.12). We assume a trial two-sublattice product wave function where the two sublattices, A and B, form a checkerboard structure. Within this approximation, the variational ansatz (3.12) has four variational parameters $(\theta_A, \phi_A, \theta_B, \phi_B)$. However, by fixing a global phase we can choose $\phi_A = -\phi_B = \phi$ without loss of generality. This ansatz is able to describe a wide range of two-sublattice bosonic phases, namely: charge density-wave (CDW) with $\mathbf{q} = (\pi, \pi)$ ordering wave vector, checkerboard supersolid (CSS) and bond-chiral superfluid (CSF); apart from the uniform ones: superfluid (SF) and fully occupied (FO) or empty (VAC). Their semiclassical

wave functions are characterized by

$$\begin{aligned}
\text{FO} &: \ \theta_A = \theta_B = 0; && (3.13)\\
\text{VAC} &: \ \theta_A = \theta_B = \pi; && (3.14)\\
\text{SF} &: \ 0 < \theta_A = \theta_B < \pi, \ \phi = 0; && (3.15)\\
\text{CSF} &: \ 0 < \theta_A = \theta_B < \pi, \ 0 < \phi < \pi/2; && (3.16)\\
\text{CDW} &: \ \theta_A = 0, \ \theta_B = \pi; && (3.17)\\
\text{CSS} &: \ \theta_A \neq \theta_B, \ \theta_A \neq 0, \pi, \ \theta_B \neq 0, \pi. && (3.18)
\end{aligned}$$

In terms of spins, the FO phase of hard-core bosons corresponds to a fully polarized ferromagnet. The SF phase is characterized by the Bose-Einstein condensation (BEC) of hard-core bosons at momentum $\mathbf{k} = (0, 0)$, which breaks the global $U(1)$ symmetry of the Hamiltonian (3.1). It corresponds to a ferromagnet with nonzero projection over the x-y plane and nonzero spin stiffness. The CSF phase, characterized by nonzero bond-chirality and a two-component BEC at $\mathbf{k} = (0, 0)$ and (π, π), corresponds to a canted magnet with staggered azimuth orientation of the spins (ϕ). The (π, π) CDW, corresponds to the Néel phase in which "up" and "down" spins alternate forming a checkerboard pattern. The CSS, characterized by the coexistence of (π, π) CDW order and BEC at $\mathbf{k} = (0, 0)$, corresponds to a staggered magnet with two sublattices having different projections over the z axis.

Substituting $S = 1/2$ in (3.11), the classical energy takes the form

$$\begin{aligned}
\mathcal{E}/N \ = \ & -\sin\theta_A \sin\theta_B \cos(2\phi) \\
& + \frac{K}{8} \sin^2\theta_A \sin^2\theta_B \cos(4\phi) \\
& - \frac{\mu}{4} \left(\cos\theta_A + \cos\theta_B + 2\right), \qquad (3.19)
\end{aligned}$$

where N is the number of sites of a square lattice with periodic boundary conditions (PBC). Minimization of (3.19) with respect to the angle parameters gives rise to three of the five phases described above (3.13)-(3.18), depending on the region of the parameter space (K, μ): FO, SF and CSF. In the three cases, the ground state wave functions satisfy $\theta_A = \theta_B = \theta$. Both SF and CSF display phase coherence, i.e. a rigid phase ϕ which is either constant $\phi = 0$ in the SF state or staggered ($\phi = \phi_A = -\phi_B$) in the CSF, where it satisfies

$$\cos(2\phi) = \frac{2}{K \sin^2\theta}. \qquad (3.20)$$

3.2.1 Order parameters

To characterize these phases, we compute two different order parameters (OPs): the condensate density associated to a bosonic superfluid and the bond-chiral OP.

The condensate density is derived from the single-particle density matrix, i.e., $\rho_{ij} = \langle \Psi_0 | a_i^\dagger a_j | \Psi_0 \rangle$, which, for a translational invariant system, is diagonal in momentum space

$$\rho_{\mathbf{k}} = \frac{1}{N^2} \sum_{ij} e^{-\mathrm{i}\mathbf{k}(\mathbf{r}_i - \mathbf{r}_j)} \rho_{ij}. \tag{3.21}$$

In the thermodynamic limit, a macroscopic eigenvalue of the single-particle density matrix signals the onset of BEC and defines the condensate density. Within the SF phase, we find a unique macroscopic eigenvalue, at momentum $\mathbf{k} = (0, 0)$,

$$\rho_0 = \frac{1}{4} \sin^2 \theta, \tag{3.22}$$

whereas a second macroscopic eigenvalue appears at $\mathbf{k} = (\pi, \pi)$ within the CSF phase. In this case, the condensate density has two components given by,

$$\rho_0 = \frac{1}{4} \sin^2 \theta \cos^2 \phi \tag{3.23}$$

and

$$\rho_\pi = \frac{1}{4} \sin^2 \theta \sin^2 \phi. \tag{3.24}$$

Notice that the CSF phase displays BEC fragmentation, although the uniform component ($\mathbf{k} = (0, 0)$) remains dominant over the staggered one ($\mathbf{k} = (\pi, \pi)$) at any finite K with $\rho_0 = \rho_\pi + (2K)^{-1}$ for $2 \leq K < \infty$. However, such a BEC fragmentation observed within the classical treatment is not expected to survive to interactions and quantum fluctuations [41].

The bond-chiral operator is defined as the z-component of the vector chirality, i.e., $\hat{\Omega}_{ij} = (\mathbf{S}_i \times \mathbf{S}_j)_z$ [37], which can be written in the bosonic language as

$$\hat{\Omega}_{ij} = \frac{\mathrm{i}}{2} \left(a_i^\dagger a_j - a_j^\dagger a_i \right), \tag{3.25}$$

where i stands for the imaginary unit and i, j are two nearest neighbour sites. The bond-chiral operator (3.25) is proportional to the current density of charged bosons, which is defined as [38],

$$\mathbf{I}_{ij} = \mathrm{i} \left(a_i^\dagger a_j - a_j^\dagger a_i \right) (q/\hbar) \hat{\mathbf{r}}_{ij}, \tag{3.26}$$

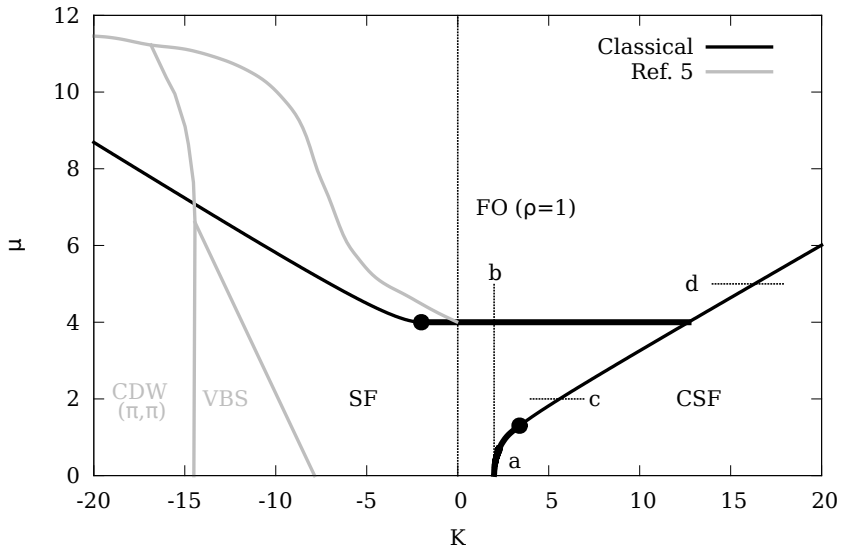

Figure 3.3: Classical phase diagram (black) and schematic phase diagram obtained by means of QMC ($K < 0$) from Ref. [31] (gray). The dashed line at $K = 0$ marks the division between the unfrustrated ($K < 0$) and the frustrated region ($K > 0$), where QMC is not applicable. Thin (thick) solid black lines correspond to first (second) order phase transitions. Four cuts (a, b, c and d) across the phase transitions are also indicated with dashed lines. The filled (black) circles indicate potential tricritical points (TCP).

where q is the charge of a boson and $\hat{\mathbf{r}}_{ij} = (\mathbf{r}_j - \mathbf{r}_i)\,/|\mathbf{r}_j - \mathbf{r}_i|$. We define the bond-chiral OP as

$$\Omega = \frac{1}{N_b} \sum_{\langle ij \rangle} |\langle \hat{\Omega}_{ij} \rangle|, \tag{3.27}$$

where $N_b = 2N$ is the total number of bonds on the square lattice. Computing (3.27) with the CSF wave function (3.16) we find

$$\Omega = \frac{1}{4} \sin\theta \sin(2\phi). \tag{3.28}$$

Differently from other chiral superfluids [39], the CSF does not present spontaneous currents around closed loops in the lattice. On the contrary, the system forms a checkerboard pattern of *source-and-drain* sites, as it is schematically represented in Fig. 3.2.

3.2.2 Phase diagram

Fig. 3.3 shows the classical phase diagram obtained by minimizing the classical energy (3.19) in the parameter space (K, μ). The phases are characterized by the

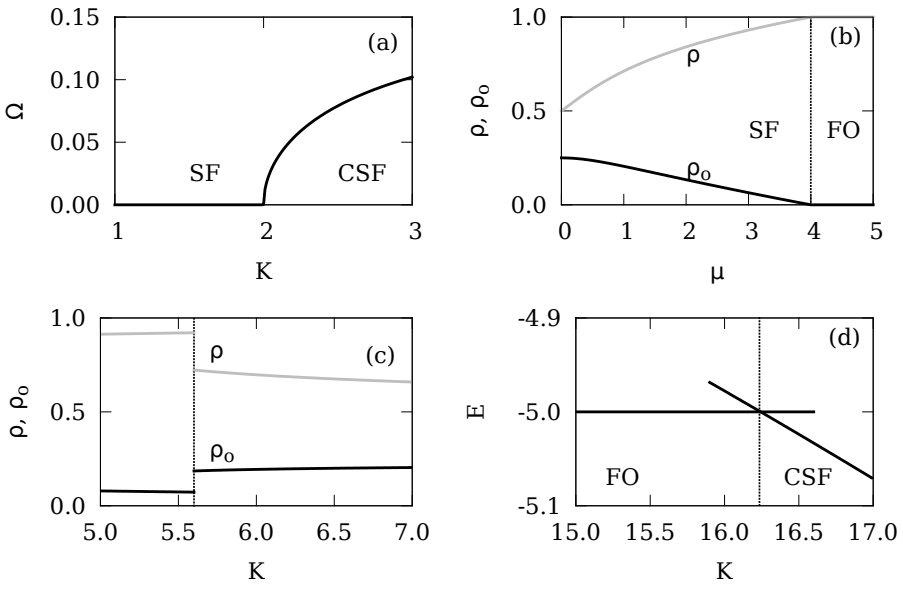

Figure 3.4: Energy (E), bond-chiral OP (Ω), condensate density (ρ_o) and total density (ρ) across four cuts in the classical phase diagram (Fig. 3.3). Panel (a): Bond-chiral OP across the SF-CSF transition at $\mu = 0$. Panel (b): Total density and condensate density for $K = 2$. Panel (c): Total density and condensate density for the CSF (black) and SF (gray) solutions along $\mu = 2$. The dashed line at $K = 5.6$ indicates the point at which the first order transition occurs. Panel (d): Energy crossing of the FO and CSF phases along $\mu = 5$.

OPs introduced above. First order phase transitions take place at an energy crossing of two different trial wave functions resulting in a discontinuity of the OPs. Second order phase transitions are determined at those points in the parameter space where the OPs vanish continuously. Also displayed in this figure is the schematic phase diagram derived from QMC results in Ref. [31] for the unfrustrated region ($K < 0$); the frustrated region ($K > 0$) is problematic for QMC due to the "sign problem". For $K < 0$ we find two phases, the FO and the SF. The VBS cannot be obtained within the single site product wave function approximation (3.12). We find a saddle point of the variational energy for the (π, π) CDW wave function (3.17), however it possesses higher energy than the SF solution. For $K > 0$ we find three different phases: FO, SF, and CSF. At half filling ($\mu = 0$) and up to $\mu \simeq 1.3$ the transition from SF to CSF is of second order type, while it is first order for $\mu \gtrsim 1.3$, suggesting the existence of a tricritical point (TCP) at $\mu \simeq 1.3$. The SF to FO transition is of second order type in all the frustrated region ($K > 0$) while it is first order for the unfrustrated regime till $K \simeq -2$, where a potential TCP exists.

In Figure 3.4 we show the energy, condensate density, total density and bond-chiral OP for the four cuts (a, b, c and d) displayed in the phase diagram of Figure 3.3. Panels are labeled according to the corresponding cuts. Panel (a) shows the continuous vanishing of the bond-chiral OP along the half filling line, signaling a second order phase transition at $K_c = 2$. Panel (b) shows the total density and the condensate density across the SF to FO transition along $K = 2$. The condensate density vanishes continuously at $\mu_c = 4$ characterizing a second order phase transition. For $\mu \gtrsim 1.3$, the SF to CSF transition is of first order type. Panel (c) displays the condensate and total densities along the $\mu = 2$ line. Both quantities present a discontinuity at $K = 5.6$, signaling a first order phase transitions. Panel (d) displays the crossing of the FO and CSF energies determining a first order phase transition.

3.3 CB Gutzwiller: 2×2 and 4×4 clusters

As it was detailed in the previous Chapter 2, by virtue of the composite boson mapping, the exact image of the J-K model in terms of the CBs will have one-, two- and four-body CB terms,

$$\begin{aligned} H^B &= \sum_{\mathbf{R}} (T_{\mathbf{R}})^{\alpha}_{\beta}\, b^{\dagger}_{\mathbf{R}\alpha} b_{\mathbf{R}\beta} \\ &+ \sum_{\langle \mathbf{R}_1 \mathbf{R}_2 \rangle} (V_{\mathbf{R}_1\mathbf{R}_2})^{\alpha_1\alpha_2}_{\beta_1\beta_2}\, b^{\dagger}_{\mathbf{R}_1\alpha_1} b^{\dagger}_{\mathbf{R}_2\alpha_2} b_{\mathbf{R}_1\beta_1} b_{\mathbf{R}_2\beta_2} \\ &+ \sum_{\langle \mathbf{R}_1\mathbf{R}_2\mathbf{R}_3\mathbf{R}_4 \rangle} (W_{\mathbf{R}_1\mathbf{R}_2\mathbf{R}_3\mathbf{R}_4})^{\alpha_1\alpha_2\alpha_3\alpha_4}_{\beta_1\beta_2\beta_3\beta_4} \\ &\times b^{\dagger}_{\mathbf{R}_1\alpha_1} b^{\dagger}_{\mathbf{R}_2\alpha_2} b^{\dagger}_{\mathbf{R}_3\alpha_3} b^{\dagger}_{\mathbf{R}_4\alpha_4} b_{\mathbf{R}_1\beta_1} b_{\mathbf{R}_2\beta_2} b_{\mathbf{R}_3\beta_3} b_{\mathbf{R}_4\beta_4}, \end{aligned} \tag{3.29}$$

where we have written it in a general basis. The specific form of the tensors T, V and W is given in the Appendix. The energy per site computed with a *homogeneus* CB Gutzwiller wave function (2.17) is

$$E = \left(T^{\mathtt{g}}_{\mathtt{g}} + 2V^{\mathtt{gg}}_{\mathtt{gg}} + W^{\mathtt{gggg}}_{\mathtt{gggg}}\right)/L^2. \tag{3.30}$$

Minimization of the energy (3.30) with the normalization constriction for the amplitudes, $\sum_{\mathbf{n}} U^{\mathtt{g}*}_{\mathbf{n}} U^{\mathtt{g}}_{\mathbf{n}} = 1$, leads to a Hartree like equation of the form (2.18),

$$\hat{h} \cdot U^{\mathtt{g}} = \lambda U^{\mathtt{g}}. \tag{3.31}$$

As it was explained in Chapter (2), solving a Hartree eigensystem is equivalent to perform the exact diagonalization of a cluster of size $L \times L$ with OBC and a set

of self-consistently defined auxiliary fields acting on its boundaries, which mimic the environment in the mean-field approximation. The Hartree matrix $\hat{h}$ can be expressed as a sum of intra- and inter-cluster terms,

$$\hat{h} = \hat{h}^{\square} + \hat{h}^{\parallel} + \hat{h}^{\times}. \tag{3.32}$$

The intra-cluster terms are all hopping, ring-exchange and chemical potential terms which act within the $L \times L$ cluster (all parameters in units of J),

$$\begin{aligned} \hat{h}^{\square} &= -\sum_{\langle ij\rangle \in \square} (a_i^{\dagger} a_j + h.c.) - \mu \sum_{j \in \square} n_j \\ &\quad + K \sum_{\langle ijkl\rangle \in \square} (a_i^{\dagger} a_k^{\dagger} a_j a_l + h.c.). \end{aligned} \tag{3.33}$$

The mean-field interaction among two nearest neighbour clusters leads to

$$\begin{aligned} \hat{h}^{\parallel} &= -\sum_{\langle ij\rangle \in \parallel} (a_i^{\dagger} \psi_j + a_i \psi_j^*) \\ &\quad + K \sum_{\langle ijkl\rangle \in \parallel} (a_i^{\dagger} a_j \varphi_{kl}^* + a_j^{\dagger} a_i \varphi_{kl}), \end{aligned} \tag{3.34}$$

where the sums are restricted to bonds, in the first case, and plaquettes, in the second (see Fig. 3.5). That is, creation (annihilation) hard-core bosonic operators act on sites lying on the boundaries of the cluster while the auxiliary fields are evaluated on the boundaries of the neighbouring cluster. In the same way, the ring-exchange interaction among four clusters leads to

$$\hat{h}^{\times} = K \sum_{\langle ijkl\rangle \in \times} (a_i^{\dagger} \psi_j \psi_k^* \psi_l + a_i \psi_j^* \psi_k \psi_l^*), \tag{3.35}$$

where now the sum reduces to the four plaquettes which touch the four corners of the cluster (see Fig. 3.5). Bosonic creation (annihilation) operators act on the four corners of the cluster and are coupled to three external auxiliary fields evaluated at the corners of the corresponding neighbouring clusters. The auxiliary fields are self-consistently defined by

$$\psi_j^* = \langle \Phi | a_j^{\dagger} | \Phi \rangle = \sum_{\mathbf{n}'} U^{\mathtt{g}*}_{\{1_j\}} U^{\mathtt{g}}_{\{0_j\}}, \tag{3.36}$$

$$\varphi_{ij}^* = \langle \Phi | a_i^{\dagger} a_j | \Phi \rangle = \sum_{\mathbf{n}'} U^{\mathtt{g}*}_{\{1_i 0_j\}} U^{\mathtt{g}}_{\{0_i 1_j\}}, \tag{3.37}$$

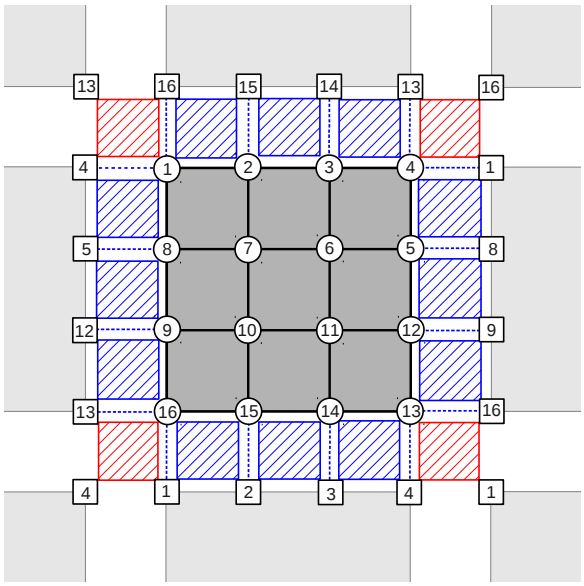

Figure 3.5: (Color online) Sketch showing a 4×4 cluster with OBC embedded in its mean-field environment. Numbers label the sites within the cluster (circles) and its vicinity (squares). Exact hopping and ring-exchange interactions within the cluster are represented by solid lines and dark shade. The chemical potential term acts on sites within the cluster. The auxiliary fields $(\psi_i^*, \psi_i, \varphi_{ij}^*, \varphi_{ij})$, which account for the mean-field embedding (see text), are evaluated on the squared sites belonging to the boundaries of the nearby clusters. The mean-field ring-exchange among four (two) neighbouring clusters is represented by red (blue) grid plaquettes, and symbolized within the formalism by $h^{\times}$ $(h^{\parallel})$. The mean-field hopping interaction is represented by dotted lines.

where $|\Phi_R\rangle = |\Phi\rangle$ is the cluster wave function defined in Eq. (2.17), and $\{1_i, 0_j\} \equiv (n_1, \ldots, 1_i, 0_j, \ldots, n_{L^2})$ refers to a cluster configuration $\mathbf{n}$ with the occupation of sites i and j fixed to be 1 and 0, respectively. The sums in (3.36) and (3.37) run over the configurations of all sites within the cluster except those at which the field is evaluated.

The energy per site (3.30) in units of J can be equivalently written in terms of the lowest eigenvalue λ of the Hartree eigensystem (3.31) and the auxiliary fields $\{\psi, \varphi\}$ as

$$\begin{aligned} E &= \frac{1}{L^2}[\lambda + \frac{1}{2}\sum_{\langle ij\rangle\in\parallel}\left(\psi_i^*\psi_j + \psi_j^*\psi_i\right) - \frac{K}{2}\sum_{\langle ijkl\rangle\in\parallel}\left(\varphi_{ij}^*\varphi_{kl} + \varphi_{kl}^*\varphi_{ij}\right) \\ &\quad - \frac{3K}{4}\sum_{\langle ijkl\rangle\in\times}\left(\psi_i^*\psi_k^*\psi_j\psi_l + \psi_j^*\psi_l^*\psi_i\psi_k\right)], \end{aligned} \tag{3.38}$$

where we subtract to the Hartree eigenvalue λ double counting terms coming from

the two- and four-cluster interactions.

In the limit $L = 1$, the superlattice and the original lattice are exactly the same and this approach is equivalent to the classical approximation derived in Sec.3.2, account taken of the two-sublattice structure, i.e., with $U_j^* = U_i$ for $i \in A,\ j \in B$. In this limit, the composite boson mapping (2.3) applied to hard-core bosons reduces to the Schwinger boson mapping of $SU(2)$ spin operators [4] written in the bosonic language. As we have seen, the matrix $\hat{U}$ automatically splits the ground state flavor (g) from its orthogonal space at each superlattice site. Within linear spin-wave theory (LSWT), the relevant quantum fluctuations over a semiclassical ground state are assumed to reside in its orthogonal space. Thus, HMFT offers a convenient algebraic scheme for computing low-lying excitations over multiple-sublattice classical ground states of spin Hamiltonians with highly non-trivial interaction terms, as it is the case for the CSF phase present in our ring-exchange model. In Appendix 3.B we provide details of the computation of LSWT excitations of the classical phase diagram derived in Section 3.2 by means of this method.

3.3.1 Order parameters and observables

In order to characterize the phases we compute within CB Gutzwiller ($L = 2, 4$) the (π, π) CDW order parameter and the two OPs already defined in the previous section, i.e., the condensate density at $\mathbf{k} = (0, 0)$ (3.21) and the bond-chiral OP (3.27). We also compute the expectation values of the hopping (3.2) and plaquette (3.3) operators over the lattice to characterize the various solid phases obtained.

The condensate density computed with the Gutzwiller wave function (2.17) in the thermodynamic limit is

$$\rho_0 = \frac{1}{N^2}\left(\sum_R \sum_{i\neq j} \langle a_i^\dagger a_j\rangle + \sum_{R\neq R'} \sum_{i\neq j} \langle a_i^\dagger\rangle\langle a_j\rangle\right), \tag{3.39}$$

where i, j lie within the same cluster R in the first term, and $i \in R$ and $j \in R' \neq R$ in the second. The first term vanishes in the thermodynamic limit for clusters of finite size, leading to

$$\rho_0 = \frac{1}{L^4}\sum_{i\in\square}\langle a_i^\dagger\rangle \sum_{j\in\square}\langle a_j\rangle = \frac{1}{L^4}|\sum_{i\in\square}\psi_i^*|^2, \tag{3.40}$$

where we took into account that the number of clusters is $M = N/L^2$ and used the definition of the auxiliary field ψ_j^* in (3.36).

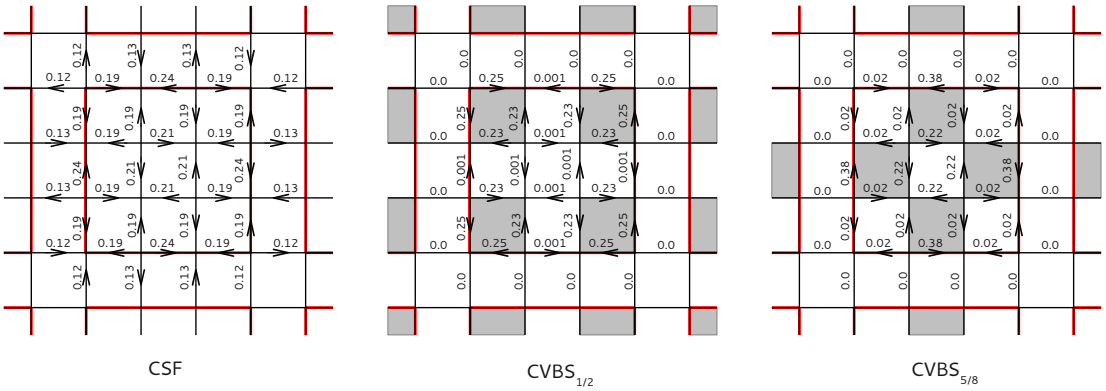

Figure 3.6: (Color online) Schematic picture showing the CSF, $\text{CVBS}_{1/2}$ and $\text{CVBS}_{5/8}$ bond-chiral phases (from left to right). The arrows indicate the bond-currents and the numbers the magnitude of the bond-chiral expectation value for each intra- and inter-cluster bond computed with 4×4 CB Gutzwiller at $\mu = 0,\ K = 2.3$ (CSF), $\mu = 0,\ K = 10$ ($\text{CVBS}_{1/2}$) and $\mu = 3.5,\ K = 5.6$ ($\text{CVBS}_{5/8}$). Grey squares highlight the underlying plaquette structure of the two CVBS phases. The magnitude of the bond-chiral order is almost uniform in the CSF phase while it has an alternating plaquette pattern in the solid phases.

The bond-chiral OP computed within the Gutzwiller approximation leads to a sum of intra- and inter-cluster terms

$$\Omega = \frac{1}{N_b}\left(\sum_{\langle ij\rangle} |\hat{\Omega}^{\square}_{ij}| + \sum_{\langle ij\rangle} |\hat{\Omega}^{\parallel}_{ij}|\right). \tag{3.41}$$

where $N_b = 2N$ is the total number of bonds. The first sum runs over all bonds lying within the clusters and the second one over all bonds linking two different clusters. The expectation value of the bond-chiral operator (3.25) acting on a bond $\langle ij\rangle$ lying within a cluster is

$$\langle \hat{\Omega}^{\square}_{ij}\rangle = -\Im(\varphi^*_{ij}), \tag{3.42}$$

where $\Im(z)$ refers to the imaginary part of a complex scalar z and φ^*_{ij} is the auxiliary field defined in (3.37). The expectation value of the bond-chiral operator (3.25) acting on a bond $\langle ij\rangle$ which links two neighbouring clusters is

$$\langle \hat{\Omega}^{\parallel}_{ij}\rangle = -\Im(\psi^*_i\psi_j), \tag{3.43}$$

where ψ^*_i is the auxiliary field defined in (3.36).

The (π,π) CDW order parameter is defined as the normalized spin structure factor at wave vector $\mathbf{q} = (\pi,\pi)$,

$$M_s^2 = S(\pi,\pi)/N, \tag{3.44}$$

where the spin structure factor is defined as the two-point correlator of S^z at equal momentum, i.e., $S(\mathbf{q}) = \sum_{ij} e^{\mathrm{i}(\mathbf{r}_i - \mathbf{r}_j)\mathbf{q}} \langle S_i^z S_j^z \rangle / N$. Following similar arguments as we did for the computation of the condensate density (3.39), Eq. (3.44) simplifies, in the thermodynamic limit, to

$$M_s = \frac{1}{L^2} \sum_{j \in \square} e^{\mathrm{i}(\pi,\pi)\mathbf{r}_j} \langle n_j - 1/2 \rangle, \tag{3.45}$$

where $\mathbf{r}_i$ is the position of site i within the cluster and we have rewritten S^z in the bosonic language.

Equivalently, the expectation values of the hopping and plaquette operators depend on whether they act on sites inside a cluster or connecting different clusters. Thus, for the hopping operator, we are led to the expressions

$$\langle \hat{B}_{ij}^{\square} \rangle \;=\; 2\Re(\varphi_{ij}^*) \tag{3.46}$$

and

$$\langle \hat{B}_{ij}^{\parallel} \rangle \;=\; 2\Re(\psi_i^* \psi_j), \tag{3.47}$$

depending on whether the bond $\langle ij \rangle$ is inside a cluster or is shared by two clusters, respectively. We have labeled with $\Re(z)$ the real part of a complex scalar z and we have made use of the auxiliary fields ψ^* and φ^* defined in (3.36) and (3.37). Note that the expectation values of the hopping (3.2) and bond-chiral (3.25) operators are directly related to the real and imaginary parts of the expectation value of a single hopping process, i.e., $\langle a_i^\dagger a_j \rangle$.

Finally, the expectation values of the plaquette operator are

$$\langle P_{ijkl}^{\square} \rangle \;=\; 2\Re \left(\sum_{\mathbf{n}'} U^{\mathrm{g}*}_{\{1_i,0_j,1_k,0_l\}} U^{\mathrm{g}}_{\{0_i,1_j,0_k,1_l\}} \right), \tag{3.48}$$

$$\langle P_{ijkl}^{\parallel} \rangle \;=\; 2\Re(\varphi_{ij}^* \varphi_{kl}), \tag{3.49}$$

or

$$\langle P_{ijkl}^{\times} \rangle \;=\; 2\Re(\psi_i^* \psi_j \psi_k^* \psi_l), \tag{3.50}$$

depending on whether $\hat{P}_{ijkl}$ acts on a plaquette lying within the cluster (3.48), between two clusters (3.49) or connecting four clusters (3.50). In the first case, the sum is restricted to the configurations over all sites within the cluster except those belonging to the plaquette $\langle ijkl \rangle$ at which the operator $\hat{P}_{ijkl}$ is evaluated.

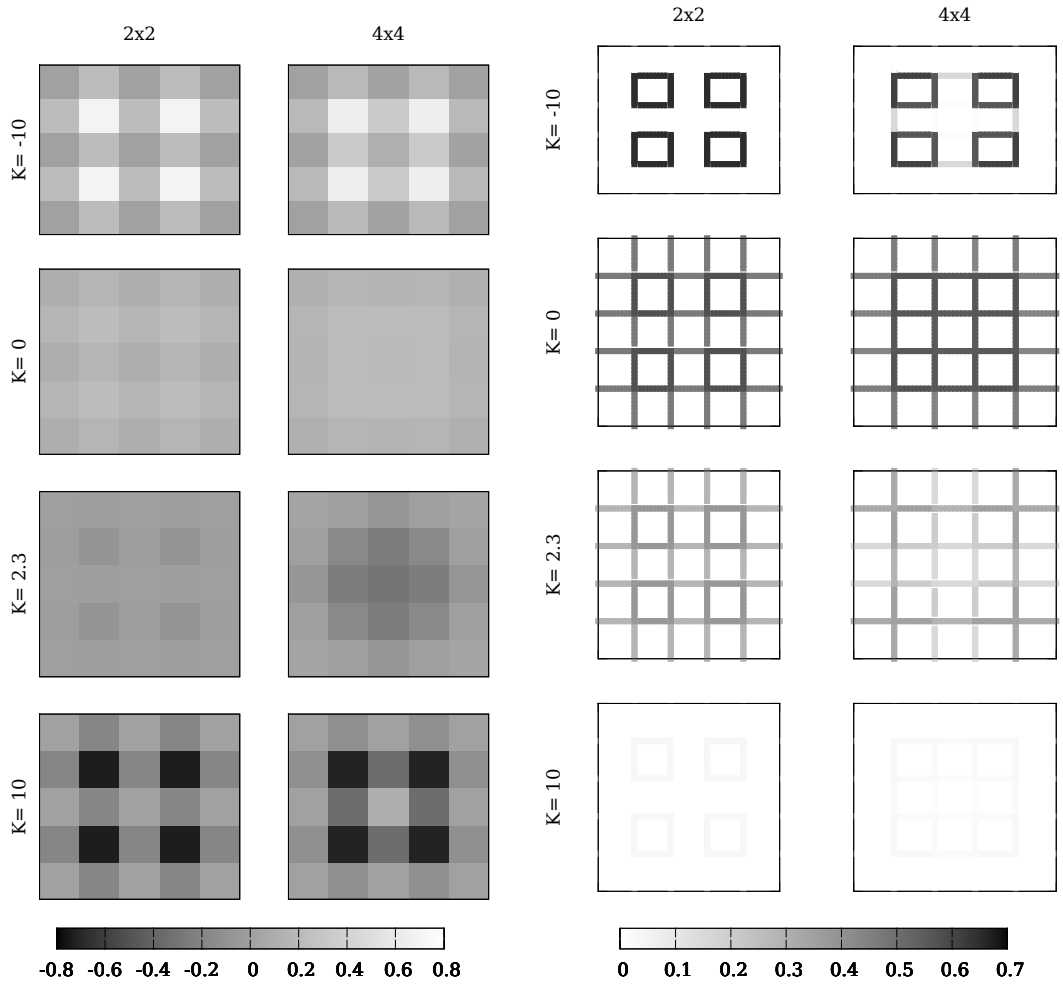

Figure 3.7: **Left:** Expectation value of the plaquette operator (3.3) computed within 2×2 (left) and 4×4 (right) CB Gutzwiller for several values of K along the half filling line ($\mu = 0$): $K = -10$ (VBS), $K = 0$ (SF), $K = 2.3$ (CSF), $K = 10$ ($\mathrm{CVBS}_{1/2}$). The panels display four 2×2 clusters surrounded by the inter-cluster plaquettes (left) and the corresponding 4×4 cluster surrounded by the inter-cluster plaquettes (right). **Right:** Expectation value of the hopping operator (3.2) computed within 2×2 (left) and 4×4 (right) CB Gutzwiller for several values of K along the half filling line ($\mu = 0$): $K = -10$ (VBS), $K = 0$ (SF), $K = 2.3$ (CSF), $K = 10$ ($\mathrm{CVBS}_{1/2}$). The panels display the bonds of four 2×2 clusters surrounded by the inter-cluster bonds (left) and the corresponding 4×4 cluster bonds surrounded by the inter-cluster bonds (right).

3.3.2 Valence bond phases

Using clusters of size 2×2 and 4×4 as the new degrees of freedom allows us to access several plaquette phases which cannot be described by standard mean-field tech-

niques. Apart from the three phases already obtained by means of the classical approximation (FO, SF and CSF), the CB Gutzwiller unveils three more phases: a valence bond solid phase for $K < 0$, and two novel valence bond-chiral solid phases for $K > 0$.

3.3.2.1 Valence bond solid $\rho = 1/2$ (VBS)

This phase is characterized by the alternating expectation value of the hopping and plaquette operators (3.46)-(3.50) along the x and y directions, fixed total density $\rho = 1/2$ and absence of bond-chiral, superfluid, or (π, π) CDW orders. Within the 2×2 approximation, the wave function obtained is a linear combination of just the $4!/2!2! = 6$ possible half filled configurations,

$$|\Phi^{2\times 2}\rangle = \alpha \left(\left| \boxed{\bullet\ \ \bullet} \right\rangle + \left| \boxed{\bullet\ \ \bullet} \right\rangle \right) + \beta \left(\left| \boxed{\bullet\bullet\ \ } \right\rangle + \left| \boxed{\bullet\ \ \bullet} \right\rangle + \left| \boxed{\bullet\ \ \bullet} \right\rangle + \left| \boxed{\bullet\bullet\ \ } \right\rangle \right), \qquad (3.51)$$

where the amplitudes α and β are real. In the spin language, this phase is paramagnetic, i.e., $\langle \mathbf{S}_j \rangle = 0$. It preserves the global $U(1)$ and C_4 symmetries of the Hamiltonian (3.1). However, it mixes the total number of bosons in each row and column, breaking the row/column ($d = 1$) $U(1)$ gauge-like symmetries (3.5).

3.3.2.2 Half filled valence bond-chiral solid ($\mathbf{CVBS}_{1/2}$)

This phase is a bond-chiral counterpart of the VBS previously described. It preserves the $U(1)$ symmetry of Hamiltonian (3.1) but breaks C_4 down to C_2, as it can also be inferred by its *source-and-drain* chiral pattern. Apart from alternating expectation values of the hopping and plaquette operators (3.46)-(3.50) and null superfluid and (π, π) CDW orders, it has nonzero bond-chiral order. The expectation value of the bond-chiral operator has a source-and-drain current pattern reminiscent of the CSF, as it is schematically represented in Fig. 3.6. In the spin language, this phase is a paramagnet, i.e., $\langle \mathbf{S}_j \rangle = 0$, with nonzero spin chirality. The cluster wave function obtained within 2×2 CB Gutzwiller is equivalent to the previous VBS (3.51), but with complex amplitudes in the diagonal configurations,

$$|\Phi^{2\times 2}\rangle = \alpha \left(e^{\mathrm{i}\varphi} \left| \boxed{\bullet\ \ \bullet} \right\rangle + e^{-\mathrm{i}\varphi} \left| \boxed{\bullet\ \ \bullet} \right\rangle \right) + \beta \left(\left| \boxed{\bullet\bullet\ \ } \right\rangle + \left| \boxed{\bullet\ \ \bullet} \right\rangle + \left| \boxed{\bullet\ \ \bullet} \right\rangle + \left| \boxed{\bullet\bullet\ \ } \right\rangle \right), \qquad (3.52)$$

where α and β are real and $0 < \varphi < \pi/2$. Moreover, in the K-only limit (3.6) both the VBS and $\mathrm{CVBS}_{1/2}$ wave functions have the same amplitudes, $\alpha = \sqrt{3/8}$ and $\beta = 1/4$, with a phase $\varphi = \pi/2$. This is consistent with the chiral symmetry of the K-only Hamiltonian (3.6) described in Sec.3.1.

Within the 4×4 CB Gutzwiller approximation, the cluster wave function obtained for both the VBS and $\mathrm{CVBS}_{1/2}$ phases live in the subspace of the $16!/8!8! = 12870$ half filled 4×4 cluster configurations. Similarly to 2×2 CB Gutzwiller, the amplitudes $U^{\mathbf{g}}_{\mathbf{n}}$ are real (complex) for the VBS ($\mathrm{CVBS}_{1/2}$) phase. Nevertheless, the 4×4 wave function preserves the alternating plaquette pattern already found by means of 2×2 CB Gutzwiller, indicating that it introduces minor quantitative corrections over the 2×2 description. Moreover, in the K-only limit, the number of nonzero amplitudes $U^{\mathbf{g}}_{\mathbf{n}}$ of the 4×4 CB Gutzwiller wave function is 1534. The leading amplitudes correspond to occupation configurations $\mathbf{n}$ which can be written as a direct product of four 2×2 diagonal configurations, i.e.,

$$|\Phi^{4\times4}\rangle = \widetilde{\alpha} \left(\left| \quad \right\rangle + \left| \quad \right\rangle \right) + \ldots, \tag{3.53}$$

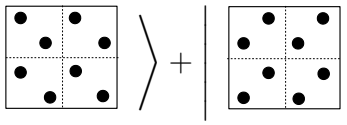

where $\ldots$ are the other relevant configurations. It is important to remark that at this K-only limit, the wave function obtained by exact diagonalization of a 4×4 cluster with PBC has only 82 configurations (out of the original 12870) with nonzero amplitudes, all of them satisfying the $d = 1$ gauge-like symmetries mentioned in Sec. 3.1.

3.3.2.3 Valence bond-chiral solid $\rho = 5/8$ ($\mathbf{CVBS}_{5/8}$)

The 4×4 CB Gutzwiller results slightly modify those already found with 2×2 CB Gutzwiller with the exception of a small region of the phase diagram (see Fig. 3.8) where another valence bond-chiral solid phase with total density $\rho = 5/8$ emerges. In the spin language, this is a magnetic phase, i.e., $\langle S^z_j \rangle = 1/8$, with nonzero bond-chiral order. This particular solid phase cannot be captured within 2×2 CB Gutzwiller scheme as it has a density which is non-commensurate with the 2×2 cluster size. The alternating plaquette pattern present in $\mathrm{CVBS}_{1/2}$ changes (see Fig. 3.6) and the number of bonds with appreciable intensity of the expectation value of the bond-chiral operator diminshes. This is a manifest consequence of the doping, which allows for less hopping and ring-exchange processes over the system, as it can be deduced by

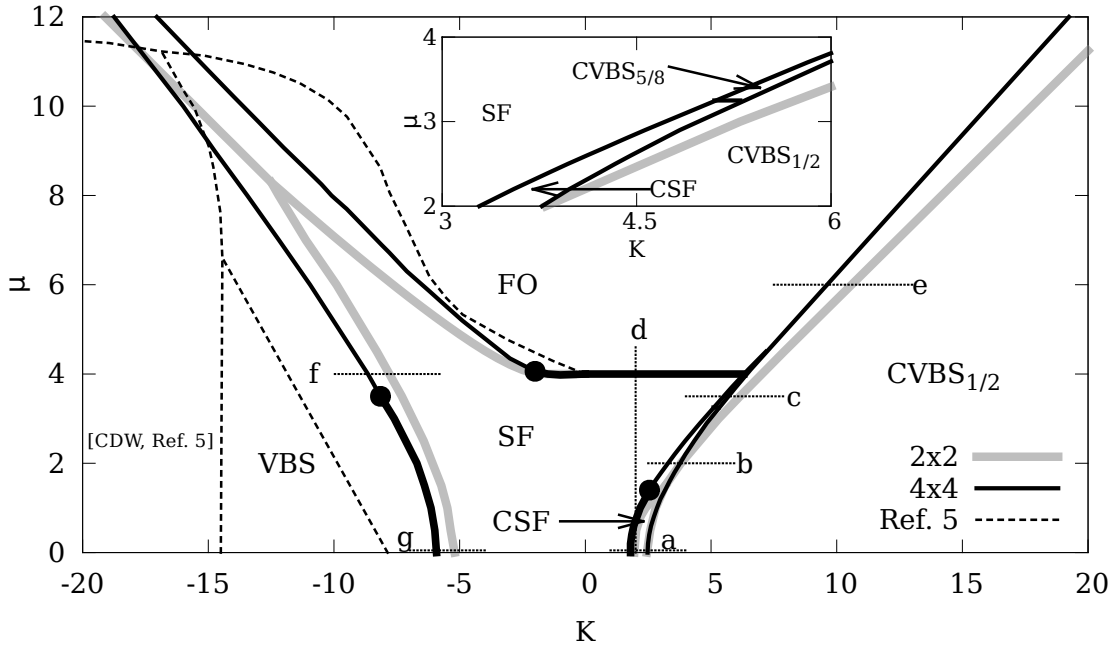

Figure 3.8: The $L\times L$ CB Gutzwiller phase diagram for $L = 2$ (gray) and $L = 4$ (black) together with QMC results from Ref. [31] (dashed line). Thick (thin) lines correspond to second (first) order phase transitions. Short dashed lines correspond to several cuts (lower case letters) for which we have examined the transition across the various phases obtained with CB Gutzwiller. The filled (black) circles correspond to potential tricritical points (TCP) within 4×4 CB Gutzwiller. The corresponding TCPs within the 2×2 CB Gutzwiller are indistinguishable in the SF-FO and SF-CSF transitions, while the SF-VBS transition is always first order. We cannot discard the possibility that some of the second order transitions are weakly first order (see text). Inset: zooming of the small region where the $\mathrm{CVBS}_{5/8}$ phase emerges.

inspecting the most relevant components of the resulting 4×4 cluster wave function,

$$|\Phi^{4\times 4}\rangle = \gamma \left(e^{\mathrm{i}\eta} \left| \right\rangle + e^{-\mathrm{i}\eta} \left| \right\rangle \right) + \dots \qquad (3.54)$$

where γ is real and $0 < \eta < \pi/2$. Notice that these configurations are related to the ones in (3.53) by the addition of two bosons at the corners of the cluster, thus maximizing the number of available ring-exchange processes within the 4×4 cluster while preserving the C_2 symmetry.

3.3.3 Phase diagram

In Fig. 3.8 the phase diagram obtained by means of $L \times L$ CB Gutzwiller ($L = 2, 4$) is displayed for both the frustrated and unfrustrated regions of the (K, μ) plane together

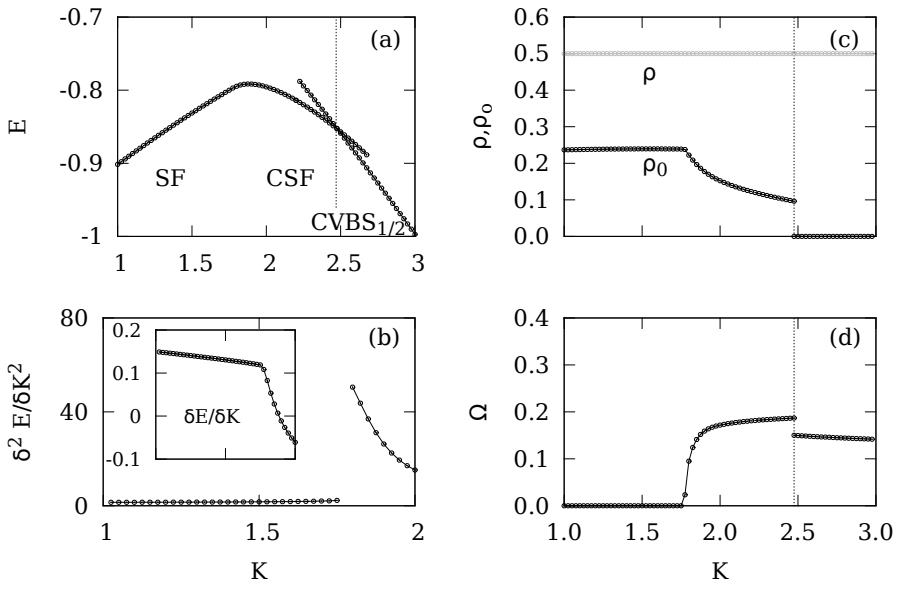

Figure 3.9: (a) Energy for the SF-CSF and CSF-CVBS$_{1/2}$ phases at $\mu = 0$ (cut a in Fig. 3.8). (b) Second and first (inset) derivatives of the energy. (c) Total (gray) and condensate (black) densities. (d) Bond-chiral order. Dotted lines mark the first order transition between CSF and CVBS$_{1/2}$ phases. Solid lines are guides to the eye. The SF-CSF phase transition is continuous, presumibly of second order.

with several cuts for which we analyze in detail the phase transitions within 4×4 CB Gutzwiller. Except for the tiny region in which the CVBS$_{5/8}$ phase emerges, the majority of the phase diagram is unveiled using 2×2 clusters as the basic degree of freedom. As it is shown in Fig. 3.7, the use of 2×2 clusters already permits us to correctly describe the essential features of all the phases, while 4×4 CB Gutzwiller includes minor quantitative corrections. In particular, we observe a uniform pattern of the plaquette and hopping expectation values (3.46)-(3.50) within the uniform SF and CSF phases, as well as the alternating plaquette pattern characteristic of the VBS and CVBS$_{1/2}$ as already described by the 2×2 approximation. Notice that within the CVBS$_{1/2}$ phase, the expectation value of the hopping operator (3.46)-(3.47) is negligible over the whole system, while the expectation value of the bond-chiral operator (3.25) has a plaquette pattern similar to the one displayed by the hopping operator within the VBS phase (not shown). In the unfrustrated region ($K < 0$), the phase diagram obtained by CB Gutzwiller presents a significant improvement as compared to a standard single site mean-field (Sec. 3.2), where the classical solution was either uniform SF or FO. The CB Gutzwiller allows for stabilization of the gapped VBS phase for large enough negative K, in qualitative agreement with QMC results

[31]. Interestingly, for $\mu = 0$ the transition point is found at $K_c^{2\times2} = -5.1$ and $K_c^{4\times4} = -5.9$, showing a slow convergence to the QMC result, $K_c^{QMC} \simeq -7.9$. Although the CB Gutzwiller is able to capture phases with (π, π) CDW order [20], we have not found any sign of long-range CDW order. In particular, we have computed the staggered magnetization OP (3.45) obtaining $M_s = 0$ over the whole diagram. Furthermore, both the VBS and $\text{CVBS}_{1/2}$ solutions are stable under the application of an external staggered magnetic field, or under the addition of a small repulsive density-density interaction term to the Hamiltonian (3.1). However, the normalized spin structure factor (3.44) for a 4×4 cluster is in agreement with previous works [30, 42, 43], and we observe stronger quantum CDW fluctuations closer to the K-only limit, regardless of the sign of K. Note in passing that Sandvik and co-workers found using QMC simulations [30, 44], on the unfrustrated side of the phase diagram, a VBS-CDW transition at $K \simeq -14.5$.

Figure 3.9 displays the energy, total and condensate densities and the bond-chiral OP across the SF-CSF and CSF-$\text{CVBS}_{1/2}$ transitions at half filling ($\mu = 0$) in the frustrated regime ($K > 0$) (cut a in Fig. 3.8). Also displayed are the first and second-order derivatives of the energy across the SF-CSF transition. The continuity of the order parameters and the derivatives of the energy across the SF-CSF transition suggest that it is of the second order type, while the jump of the order parameters and the energy crossing along the CSF-$\text{CVBS}_{1/2}$ transition indicates that it is of the first order type.

Figure 3.10 displays the energy, total and condensate densities and the bond-chiral OP across the SF-CSF-$\text{CVBS}_{1/2}$ and SF-$\text{CVBS}_{5/8}$-$\text{CVBS}_{1/2}$ transitions at $\mu = 2$ (cut b in Fig. 3.8) and $\mu = 3.5$ (cut c in Fig. 3.8), respectively. In all cases, the phase transitions are of the first order type, as they are signaled by discontinuities in the order parameters and the level-crossing of the energies. At $\mu \simeq 1.5$, a potential TCP exists in the SF-CSF boundary.

Figure 3.11 displays the CSF-SF and SF to FO transitions along $K = 2$ (cut d in Fig. 3.8). The two transitions are continuous, presumably of the second order type, as they are signaled by the energy derivatives and the continuous vanishing of the order parameters.

Figure 3.12 displays the energy and the bond-chiral OP for the FO to $\text{CVBS}_{1/2}$ along $\mu = 6$ for the frustrated regime $K > 0$ (cut e in Fig. 3.8). Both the crossing of the energy and the discontinuity of the order parameter indicates a first order phase transition. Figure 3.13 displays the energy and its first and second-order derivatives for the SF-VBS transition at $\mu = 0$ (cut f in Fig. 3.8) and $\mu = 4$ (cut g

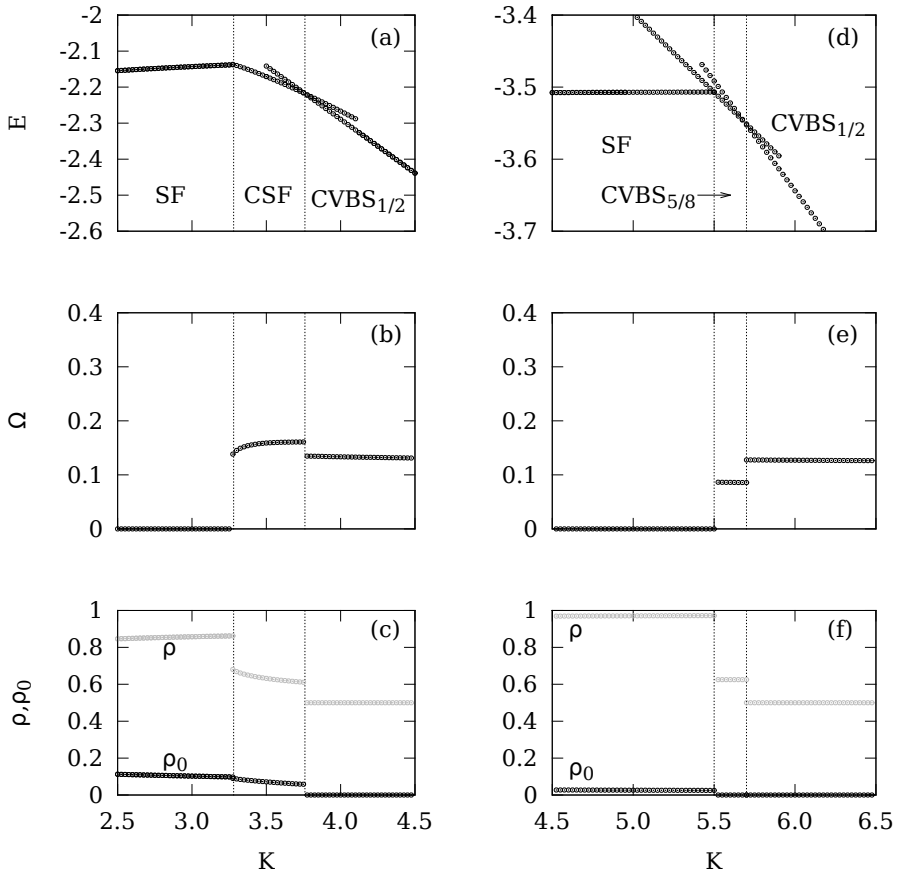

Figure 3.10: Energy, bond-chiral order, and total and condensate densities for $\mu = 2$ (cut b in Fig. 3.8) are shown in panels (a), (b), and (c), respectively. The same observables, for $\mu = 3.5$ (cut c in Fig. 3.8) are shown in panels (d), (e), and (f). Dotted lines mark the first order phase transitions.

in Fig. 3.8) for the unfrustrated regime ($K < 0$). In the first case, the continuous vanishing of the condensate density and the energy derivatives suggest a continuous phase transition. In this particular case, based on the cluster sizes used, we cannot definitively conclude whether the phase transition remains continuous or becomes weakly first order in the thermodynamic limit. In the second case, the first derivative of the energy and the vanishing of the condensate density suggest a first order phase transition. At approximately $\mu \simeq 3.5$, a potential TCP exists, which separates the first and the second order phase transition along the VBS-SF boundary.

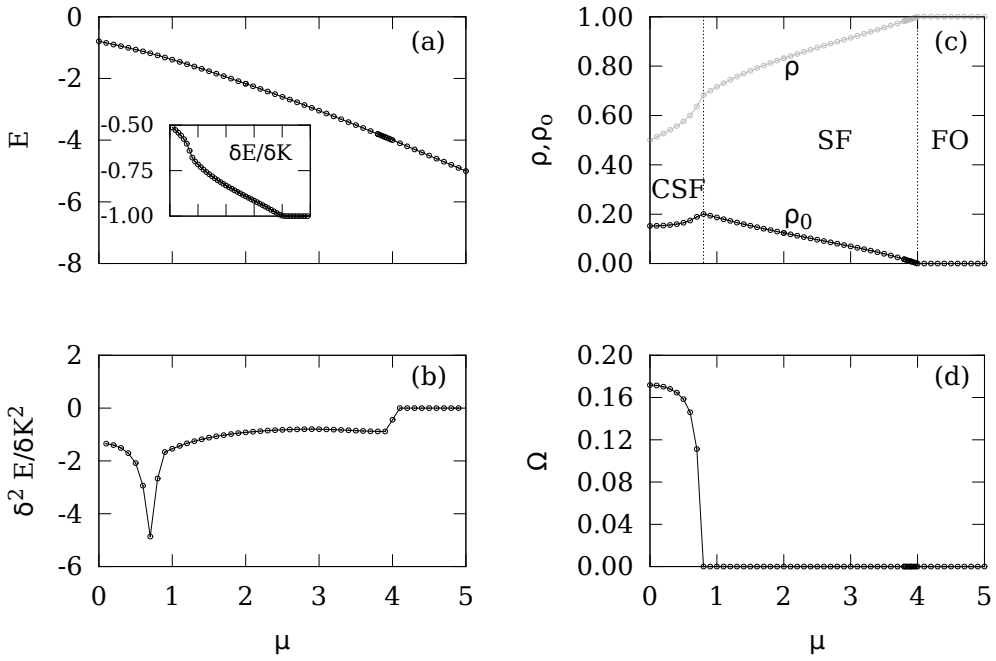

Figure 3.11: (a) Energy and its first derivative (inset), (b) second-order derivative, (c) total and condensate densities, and (d) bond-chiral order for $K = 2$ (cut d in Fig. 3.8).

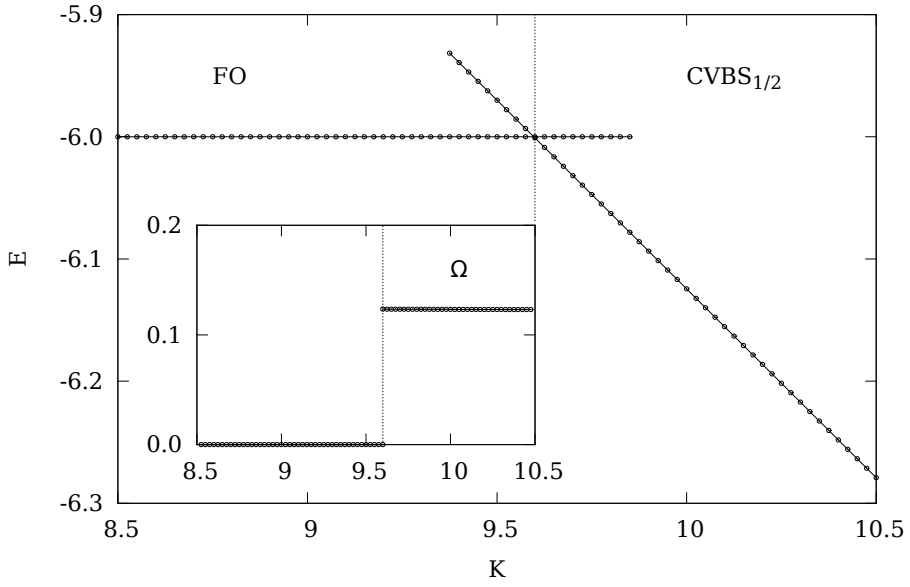

Figure 3.12: Energy and bond-chiral order parameter (inset) across the FO to $\mathrm{CVBS}_{1/2}$ first order phase transition (cut e in Fig. 3.8).

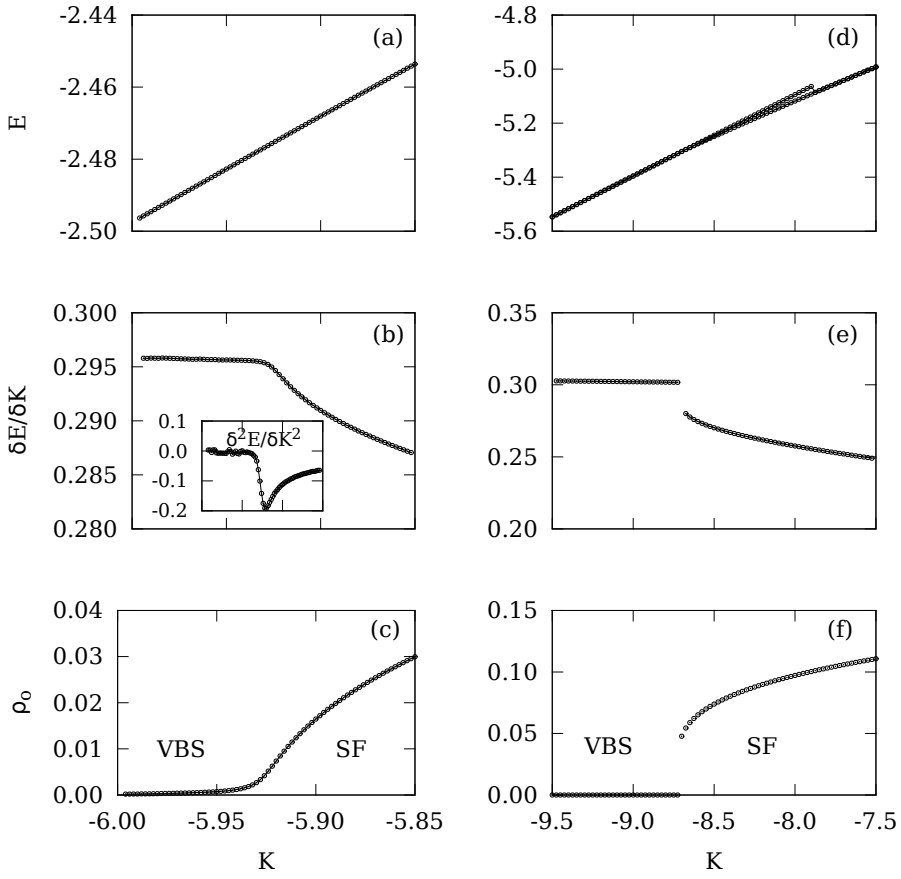

Figure 3.13: (a) Energy, (b) its first and second-order (inset) derivatives, and (c) condensate density across the VBS-SF transition at $\mu = 0$ (cut g in Fig. 3.8). The second derivative suggests that it is a continuous quantum phase transition, although we cannot discard the possibility of a weakly first order transition. (d) Energy, (e) its first derivative, and (f) condensate density across the VBS-SF transition at $\mu = 4$ (cut e in Fig. 3.8). It represents a first order phase transition, as it can be deduced from the discontinuity present both in the first derivative of the energy and in the condensate density order parameter.

3.4 Summary

In this chapter we studied the quantum phase diagram of the J-K model, for arbitrary densities, by means of the CB Gutzwiller ansatz, following the lines of previous HMFT studies on spin models [19, 20, 21].

Using $L \times L$ clusters of sizes $L = 2, 4$ as the new degrees of freedom, we have obtained a rich phase diagram where several superfluid and solid phases are characterized by emerging bond-chiral orders. Apart from the uniform superfluid and the

trivial fully occupied (empty) phases, we have encountered a bond-chiral superfluid and two novel valence bond-chiral solid phases characterized by an alternating expectation values of the plaquette and hopping operators along the x and y directions. Our main result is summarized in the phase diagram of Fig. 3.8 with quantum phases schematically depicted in Fig. 3.2.

We have shown how the use of clusters larger than a single site permits to unveil various solid phases which cannot be obtained by standard (single site) mean-field techniques. In particular, the classical approximation fails to correctly describe the ground state phase diagram of this model for ring-exchange intensities $K \geq |2|$. In the frustrated region, this approximation predicts a bond-chiral superfluid phase for $K > 2$ which reduces to a tiny region when using $L{\times}L$ CB Gutzwiller ($L = 2, 4$) giving rise to a new bond-chiral $\mathrm{CVBS}_{1/2}$ phase.

The phase diagram is mostly unveiled by means of 2×2 CB Gutzwiller. The use of 4×4 clusters includes minor quantitative corrections over 2×2 CB Gutzwiller results, with the exception of a tiny region of the CSF phase where a novel valence bond-chiral solid of density $\rho = 5/8$, $\mathrm{CVBS}_{5/8}$, emerges. Although the limited size of the clusters may mask unusual phases characterized by correlations lengths greater than the ones comprised in a 4×4 cluster, our results suggest that the structure of the phase diagram will remain in the thermodynamic limit. Computing with larger clusters (e.g. 6×6, 8×8,...) might lead to the appearance of a mosaic of solid phases with commensurate densities in the narrow region mentioned above. Numerical studies with larger clusters would allow us to perform a rigorous finite-size scaling, however, this is highly demanding from a computational standpoint.

As the original and the cluster degrees of freedom are related by a canonical mapping, the composite particle algebraic framework offers the possibility to compute low-lying excitations within a unified framework. In particular, being 1×1 CB Gutzwiller equivalent to the classical approximation, we have also shown that the method offers a convenient way to compute spin-wave dispersions over a multiple-sublattice classical ground state of a Hamiltonian with non-trivial interactions, such as the CSF ground state present in the J-K Hamiltonian.

We have also computed the phase diagram in the unfrustrated regime obtaining results in qualitative agreement with previous QMC calculations [30, 31, 44]. However, we have not found the (π, π) CDW phase and its phase transition to VBS predicted by QMC, within any of the approximations (classical, 2×2 and 4×4 CB Gutzwiller), even if all these approximations have been able to capture this kind of phase in several

other models. This discrepancy could be related to an abnormal intrinsic correlation length greater than the dimensions of the 4×4 cluster utilized in our approach.

Appendix

3.A 2×2 and 4×4 CB Matrix elements

In this Appendix we derive the specific form of the one-, two-, and four-body tensors of the CB Hamiltonian (3.29) which results from the mapping of the J-K model. Let us start with the one-body tensor. As explained in Chapter. 2, one-body CB terms account for all the original interactions which act within a cluster labeled by the index R. Taking this into account, the explicit form of the one-body CB tensor is

$$\begin{aligned}(T_{\mathbf{R}})^{\alpha}_{\beta} &= -\mu \sum_{\mathbf{n}} \sum_{j \in \mathbf{R}} n_j U^{\alpha *}_{\mathbf{R}\mathbf{n}} U^{\beta}_{\mathbf{R}\mathbf{n}} \\ &+ \sum_{\mathbf{n}'} \sum_{\langle ij \rangle \in \mathbf{R}} \left(U^{\alpha *}_{\mathbf{R}\{1_i,0_j\}} U^{\beta}_{\mathbf{R}\{0_i,1_j\}} + U^{\alpha *}_{\mathbf{R}\{0_i,1_j\}} U^{\beta}_{\mathbf{R}\{1_i,0_j\}} \right) \\ &+ K \sum_{\mathbf{n}'} \sum_{\langle ijkl \rangle \in \mathbf{R}} (U^{\alpha *}_{\mathbf{R}\{1_i,0_j,1_k,0_l\}} U^{\beta}_{\mathbf{R}\{0_i,1_j,0_k,1_l\}} + U^{\alpha *}_{\mathbf{R}\{1_i,0_j,1_k,0_l\}} U^{\beta}_{\mathbf{R}\{0_i,1_j,0_k,1_l\}}),\end{aligned} \tag{3.55}$$

where we have used the notation $\{1_i, 0_j\} \equiv (\ldots, 1_i, 0_j, \ldots)$ to label any cluster state $\mathbf{n}$ with the occupation of sites $i, j \in \mathbf{R}$ fixed to 1 and 0, respectively. The sums $\sum_{\mathbf{n}'}$ run over all configurations of the remaining sites. In the same way, the two-body CB tensor is,

$$\begin{aligned}(V_{\mathbf{R}_1\mathbf{R}_2})^{\alpha_1\alpha_2}_{\beta_1\beta_2} &= \sum_{\mathbf{n_1}', \mathbf{n_2}'} \sum_{\langle ij \rangle} (U^{\alpha_1 *}_{\mathbf{R}_1\{0_i\}} U^{\alpha_2 *}_{\mathbf{R}_2\{1_j\}} U^{\beta_1}_{\mathbf{R}_1\{1_i\}} U^{\beta_2}_{\mathbf{R}_2\{0_j\}} \\ &\qquad + U^{\alpha_1 *}_{\mathbf{R}_1\{1_i\}} U^{\alpha_2 *}_{\mathbf{R}_2\{0_j\}} U^{\beta_1}_{\mathbf{R}_1\{0_i\}} U^{\beta_2}_{\mathbf{R}_2\{1_j\}}) \\ &+ K \sum_{\mathbf{n_1}', \mathbf{n_2}'} \sum_{\langle ijkl \rangle} (U^{\alpha_1 *}_{\mathbf{R}_1\{1_i,0_j\}} U^{\alpha_2 *}_{\mathbf{R}_2\{0_k,1_l\}} U^{\beta_1}_{\mathbf{R}_1\{0_i,1_j\}} U^{\beta_2}_{\mathbf{R}_2\{1_k,0_l\}} \\ &\qquad + U^{\alpha_1 *}_{\mathbf{R}_1\{0_i,1_j\}} U^{\alpha_2 *}_{\mathbf{R}_2\{1_k,0_l\}} U^{\beta_1}_{\mathbf{R}_1\{1_i,0_j\}} U^{\beta_2}_{\mathbf{R}_2\{0_k,1_l\}}),\end{aligned} \tag{3.56}$$

where in the first sum $i \in \mathbf{R}_1$ and $j \in \mathbf{R}_2$ and, in the second one, $i, j \in \mathbf{R}_1$ and $k, l \in \mathbf{R}_2$. Finally, the explicit form of the four-body tensor accounts for the double hopping of bosons from the corners of two next-nearest neighbour clusters to the

corners of the two opposite diagonal clusters,

$$(W_{\mathbf{R}_1\mathbf{R}_2\mathbf{R}_3\mathbf{R}_4})^{\alpha_1\alpha_2\alpha_3\alpha_4}_{\beta_1\beta_2\beta_3\beta_4} = K \sum_{\langle ijkl\rangle} \sum_{\mathbf{n}'_1\mathbf{n}'_2\mathbf{n}'_3\mathbf{n}'_4} (U^{\alpha_1 *}_{\mathbf{R}_1\{1_i\}} U^{\alpha_2 *}_{\mathbf{R}_2\{0_j\}} U^{\alpha_3 *}_{\mathbf{R}_3\{1_k\}} U^{\alpha_4 *}_{\mathbf{R}_4\{0_l\}} U^{\beta_1}_{\mathbf{R}_1\{0_i\}} U^{\beta_2}_{\mathbf{R}_2\{1_j\}} U^{\beta_3}_{\mathbf{R}_3\{0_k\}} U^{\beta_4}_{\mathbf{R}_4\{1_l\}} + U^{\alpha_1 *}_{\mathbf{R}_1\{0_i\}} U^{\alpha_2 *}_{\mathbf{R}_2\{1_j\}} U^{\alpha_3 *}_{\mathbf{R}_3\{0_k\}} U^{\alpha_4 *}_{\mathbf{R}_4\{1_l\}} U^{\beta_1}_{\mathbf{R}_1\{1_i\}} U^{\beta_2}_{\mathbf{R}_2\{0_j\}} U^{\beta_3}_{\mathbf{R}_3\{1_k\}} U^{\beta_4}_{\mathbf{R}_4\{0_l\}}). \quad (3.57)$$

3.B Linear Spin-Wave theory via Schwinger bosons

Linear Spin-Wave Theory (LSWT) is a semiclassical approach which takes into account the quantum fluctuations around the classical solution on the assumption that these are small compared to the expectation value of the spin and, therefore, the classical ground state is a good approximation to the quantum ground state. The general procedure followed, when applying LSWT to a spin Hamiltonian, consists of the following steps: (*i*) rotate the spin basis at each site aligning the quantization axis with the classical spin, (*ii*) perform a Holstein-Primakoff (HP) approximation in which the Hamiltonian is expanded in terms of HP canonical boson operators up to order $1/S$, and (*iii*) diagonalize the resulting quadratic Hamiltonian by means of a Bogoliubov transformation. By this means, we automatically obtain the quantum corrections to the classical energy and the Bogoliubov eigenvalues provide the magnon dispersion relation. The $1/S$ correction to other thermodynamic quantities (total density, condensate density, etc) is automatically accounted for by taking derivatives of the corrected ground state energy with respect to the variational and physical parameters (chemical potential, transverse field, etc) and evaluating them at the zero-point.

However, if we were interested in quantities which cannot be directly derived from the ground state energy, i.e., expectation values of observables other than the Hamiltonian, a more subtle analysis has to be done. For a detailed discussion on how to correctly compute the $O(1/S)$ corrections to expectation values in the semiclassical approach, see Ref. [45]. This analysis goes beyond the scope of the present thesis, as we will be only interested in the SW magnon dispersion relation and corrections to the classical energy.

The general procedure described previously can be straightforwardly applied to the J-K model when accounting for quantum fluctuations over the SF ground state. It becomes lengthy and tedious, however, when the ground state is the CSF. For this reason, we will work within the $L\times L$ composite boson framework described above, and show that it is exactly equivalent to the usual procedure, although more advantageous when treating Hamiltonians with complex many-body interacting terms. For the

particular case of 1×1, the CB mapping (2.3) is equivalent to the Schwinger boson mapping in the bosonic language.

First, let us express Hamiltonian (3.1) in terms of Schwinger bosons $\{b_{j0}^{(\dagger)}, b_{j1}^{(\dagger)}\}$, which create (annihilate) an empty (0) or occupied (1) state at site j of the original lattice,

$$\begin{aligned} H &= -\sum_{\langle i,j\rangle}\left(b_{i1}^{\dagger}b_{j0}^{\dagger}b_{i0}b_{j1} + \text{H.c.}\right) - \mu\sum_{j} b_{j1}^{\dagger}b_{j1} \\ &\quad + K\sum_{\langle ijkl\rangle}\left(b_{i0}^{\dagger}b_{j1}^{\dagger}b_{k0}^{\dagger}b_{l1}^{\dagger}b_{i1}b_{j0}b_{k1}b_{l0} + h.c.\right) \\ &\quad - \lambda\left(b_{j0}^{\dagger}b_{j0} + b_{j1}^{\dagger}b_{j1} - 1\right), \end{aligned} \tag{3.58}$$

where we have added the physical constraint, $\sum_{n=0,1} b_{jn}^{\dagger}b_{jn} = 1$, via a Lagrange multiplier λ, playing the role of an effective chemical potential. The relevant quantum fluctuations accounted for by the LSWT and which lead to low-lying excitations of the classical ground states reside in the space orthogonal to the one determined by the classical solution at each site of the lattice. Let us re-express Hamiltonian (3.58) in a new basis in which the ground state is enconded in one flavor (g) and the orthogonal space in the other (f). As seen before, the CSF has a two-sublattice structure where the azimuth angle of the pseudospin takes the values $\pm\phi$ depending on the sublattice. Therefore, the canonical transformation among the new CBs has to include this information about the ground state,

$$b_{j\alpha}^{\dagger} = \sum_{n} U_{n}^{\alpha}\, b_{jn}^{\dagger}\ , \text{ for } j \in A, \tag{3.59}$$

$$b_{j\alpha}^{\dagger} = \sum_{n} (U_{n}^{\alpha})^{*}\, b_{jn}^{\dagger}\ , \text{ for } j \in B, \tag{3.60}$$

where α takes just two values g and p, and $n = 0, 1$. We know from Section 3.2 that its explicit form is

$$\hat{U} = \begin{pmatrix} \sin(\theta/2)\, e^{\mathrm{i}\frac{\phi}{2}} & -\cos(\theta/2)\, e^{\mathrm{i}\frac{\phi}{2}} \\ \cos(\theta/2)\, e^{-\mathrm{i}\frac{\phi}{2}} & \sin(\theta/2)\, e^{-\mathrm{i}\frac{\phi}{2}} \end{pmatrix}, \tag{3.61}$$

where the first column (U_{n}^{g}), accounts for the classical solution (3.12) and the second column (U_{n}^{p}) accounts for the orthogonal space. Applying transformations (3.59) and

(3.60) to the Hamiltonian (3.58),

$$\begin{aligned} H &= -\mu \sum_{j\in A} T^{\alpha}_{\beta} \left(b^{\dagger}_{j\alpha} b_{j\beta} + b^{\dagger}_{j+\hat{\mathbf{x}},\alpha} b_{j+\hat{\mathbf{x}},\beta} \right) \\ &\quad - \sum_{j\in A} \sum_{\mathbf{u}} V^{\alpha\beta}_{\alpha'\beta'} b^{\dagger}_{j\alpha} b^{\dagger}_{j+\mathbf{u},\beta} b_{j\alpha'} b_{j+\mathbf{u},\beta'} \\ &\quad + \frac{1}{2} K \sum_{j\in A} \sum_{\mathbf{u},\mathbf{v}} W^{\alpha\beta\gamma\delta}_{\alpha'\beta'\gamma'\delta'} b^{\dagger}_{j,\alpha} b^{\dagger}_{j+\mathbf{u},\beta} b^{\dagger}_{j+\mathbf{u}+\mathbf{v},\gamma} b^{\dagger}_{j+\mathbf{v},\delta} b_{j,\alpha'} b_{j+\mathbf{u},\beta'} b_{j+\mathbf{u}+\mathbf{v},\gamma'} b_{j+\mathbf{v},\delta'} \\ &\quad - \lambda \sum_{j\in A} \left(b^{\dagger}_{j\alpha} b_{j\beta} + b^{\dagger}_{j+\hat{\mathbf{x}},\alpha} b_{j+\hat{\mathbf{x}},\beta} - 2 \right), \end{aligned} \tag{3.62}$$

where $\hat{\mathbf{x}}, \hat{\mathbf{y}}$ are unit vectors, $\mathbf{u}$ involves a sum over $\pm\hat{\mathbf{x}}, \pm\hat{\mathbf{y}}$ in the second line, and $\mathbf{u}$ ($\mathbf{v}$) a sum over $\pm\hat{\mathbf{x}}$ ($\pm\hat{\mathbf{y}}$) in the third line. The matrix elements T^{α}_{β}, $V^{\alpha\beta}_{\alpha'\beta'}$ and $W^{\alpha\beta\gamma\delta}_{\alpha'\beta'\gamma'\delta'}$ contain all the information about the original Hamiltonian (3.1) and the classical ground state. These matrix elements are explicitly given by

$$T^{\alpha}_{\beta} = \sum_{n} n U^{\alpha *}_{n} U^{\beta}_{n} = \sum_{n} n U^{\alpha}_{n} U^{\beta *}_{n}, \tag{3.63}$$

$$V^{\alpha\beta}_{\alpha'\beta'} = U^{\alpha *}_{0} U^{\beta}_{1} U^{\alpha'}_{1} U^{\beta' *}_{0} + U^{\alpha *}_{1} U^{\beta}_{0} U^{\alpha'}_{0} U^{\beta' *}_{1}, \tag{3.64}$$

$$\begin{aligned} W^{\alpha\beta\gamma\delta}_{\alpha'\beta'\gamma'\delta'} &= U^{\alpha *}_{1} U^{\beta}_{0} U^{\gamma *}_{1} U^{\delta}_{0} U^{\alpha'}_{0} U^{\beta' *}_{1} U^{\gamma'}_{0} U^{\delta' *}_{1} \\ &\quad + U^{\alpha *}_{0} U^{\beta}_{1} U^{\gamma *}_{0} U^{\delta}_{1} U^{\alpha'}_{1} U^{\beta' *}_{0} U^{\gamma'}_{1} U^{\delta' *}_{0}. \end{aligned} \tag{3.65}$$

By construction, they "keep memory" of the bipartite nature of the CSF ground state and they are therefore link-dependent.

3.B.1 CB Gutzwiller 1×1

In this new basis, the CSF product wave function (3.12) can be rewritten in a CB Gutzwiller form,

$$|\Psi\rangle = \prod_{j} b^{\dagger}_{j\mathsf{g}} |0\rangle. \tag{3.66}$$

The expectation value of (3.62) with this wave function is the classical energy (3.11), which expressed in terms of the matrix elements T, V and W can be written in the following compact form,

$$\mathcal{E} = 2M \left(-\mu T^{\mathsf{g}}_{\mathsf{g}} - 2J V^{\mathsf{gg}}_{\mathsf{gg}} + K W^{\mathsf{gggg}}_{\mathsf{gggg}} \right), \tag{3.67}$$

where $M = N/2$ is the number of sites on sublattice A (half of the original lattice). It will be computationally convenient to cast the variational equations in the Hartree

matrix form (2.18). For this purpose, we can rewrite the unitary transformation (3.61) as

$$\hat{U} = \begin{pmatrix} x\,[z_{\rm r} + {\rm i}z_{\rm i}] & -y\,[z_{\rm r} + {\rm i}z_{\rm i}] \\ y\,[z_{\rm r} - {\rm i}z_{\rm i}] & x\,[z_{\rm r} - {\rm i}z_{\rm i}] \end{pmatrix}, \tag{3.68}$$

where $x, y, z_{\rm r}, z_{\rm i} \in \mathbb{R}$, and compute derivatives with respect to the variational parameters, $x,\ y,\ z_{\rm r},$ and $z_{\rm i}$, under the unitarity constraint. We split the *amplitude* ($x = \sin(\theta/2),\ y = \cos(\theta/2)$) and *phase* ($z_{\rm r} + {\rm i}z_{\rm i} = e^{{\rm i}\phi/2}$) parts for computational convenience. The Hartree equation therefore reduces to two coupled matrix equations

$$\hat{h}^{\theta}\mathbf{x} = \lambda\mathbf{x}, \tag{3.69}$$

$$\hat{h}^{\phi}\mathbf{z} = \eta\mathbf{z}, \tag{3.70}$$

where $\mathbf{x} = (x, y)$, $\mathbf{z} = (z_{\rm r}, z_{\rm i})$, and η is a Lagrange multiplier enforcing $z_{\rm r}^2 + z_{\rm i}^2 = 1$. Note that λ works as a chemical potential which fixes to unity the total density of the Schwinger boson system, while η has no physical relevance. The explicit form of $\hat{h}^{\theta}$ is

$$\hat{h}^{\theta} = \begin{pmatrix} 0 & h_{12}^{\theta} \\ h_{12}^{\theta} & -\mu \end{pmatrix}, \tag{3.71}$$

where $h_{12}^{\theta} = -4\,(xy)\cos(2\phi) + 4K\,(xy)^3\cos(4\phi)$, while $\hat{h}^{\phi}$ is given by

$$\hat{h}^{\phi} = \begin{pmatrix} h_{11}^{\phi} & h_{12}^{\phi} \\ h_{12}^{\phi} & h_{22}^{\phi} \end{pmatrix}, \tag{3.72}$$

with matrix elements

$$h_{11}^{\phi} = -4\,(xy)^2 + 4K\,(xy)^4\,z_{\rm r}^2, \tag{3.73}$$

$$h_{12}^{\phi} = -12K\,(xy)^4\,z_{\rm r}z_{\rm i}, \tag{3.74}$$

$$h_{22}^{\phi} = 4\,(xy)^2 + 4K\,(xy)^4\,z_{\rm i}^2. \tag{3.75}$$

3.B.2 Holstein-Primakoff approximation

To compute the LSWT corrections to the energy and find the magnon dispersion relations over each classical ground state, we apply the HP transformation to the bosonic Hamiltonian (3.62). As we have already expressed it in terms of the ground state (g) and its orthogonal space (f), the HP transformation simply reads [4]

$$b_{j\mathsf{f}}^{\dagger}b_{j\mathsf{f}} = b_j^{\dagger}b_j, \tag{3.76}$$

$$b_{j\mathsf{g}}^{\dagger}b_{j\mathsf{g}} = 1 - b_j^{\dagger}b_j, \tag{3.77}$$

$$b_{j\mathsf{g}}^{\dagger}b_{j\mathsf{f}} = \sqrt{1 - b_j^{\dagger}b_j}\ b_j, \tag{3.78}$$

$$b_{j\mathsf{f}}^{\dagger}b_{j\mathsf{g}} = b_j^{\dagger}\sqrt{1 - b_j^{\dagger}b_j}. \tag{3.79}$$

The HP bosons $\{b_j^\dagger, b_j\}$ obey standard canonical commutation relations. Assuming that the fluctuations over the classical ground state are small, one can expand the Hamiltonian up to terms quadratic in the HP bosons and then Fourier transform,

$$b_{\mathbf{r}_j}^\dagger = \frac{1}{\sqrt{L^2/2}} \sum_{\mathbf{k}\in BZ} e^{-\mathrm{i}\mathbf{k}.\mathbf{r}_j}\ b_{\mathbf{k}}^\dagger, \tag{3.80}$$

$$b_{\mathbf{r}_j+\mathbf{u}}^\dagger = \frac{1}{\sqrt{L^2/2}} \sum_{\mathbf{k}\in BZ} e^{-\mathrm{i}\mathbf{k}.(\mathbf{r}_j+\mathbf{u})}\ \tilde{b}_{\mathbf{k}}^\dagger, \tag{3.81}$$

where we keep track of the two sublattices by adding a tilde for sublattice B. The first Brillouin zone (BZ), is defined as a square with vertices $(\pm\pi, 0)$ and $(0, \pm\pi)$. Finally, the Hamiltonian takes the form $H = \mathcal{E} + H_2 + \ldots$, equivalently to (2.30),where the second order part of the Hamiltonian can be cast in matrix form [26],

$$H_2 = \sum_{\mathbf{k}} \left(\beta_{\mathbf{k}}^\dagger, \beta_{-\mathbf{k}}\right) \begin{pmatrix} \hat{A}_{\mathbf{k}} & \hat{B}_{\mathbf{k}} \\ \hat{B}_{\mathbf{k}}^* & \hat{A}_{\mathbf{k}} \end{pmatrix} \begin{pmatrix} \beta_{\mathbf{k}} \\ \beta_{-\mathbf{k}}^\dagger \end{pmatrix} - \sum_{\mathbf{k}} \mathrm{tr}\left(\hat{A}_{\mathbf{k}}\right) \tag{3.82}$$

where we have defined $\beta_{\mathbf{k}}^{(\dagger)} = (b_{\mathbf{k}}^{(\dagger)}, \tilde{b}_{\mathbf{k}}^{(\dagger)})$ and $\hat{A}$ and $\hat{B}$ are 2×2 matrices with components

$$A_{\mathbf{k}}^{11} = A_{\mathbf{k}}^{22} = -\frac{1}{2}(\mu T + \lambda) - 2JV_1 + 2KW_1(1 + \cos k_x \cos k_y) \tag{3.83}$$

$$A_{\mathbf{k}}^{12} = (A_{\mathbf{k}}^{21})^* = (-JV_2 + 2KW_2)\,\gamma_{\mathbf{k}} \tag{3.84}$$

$$B_{\mathbf{k}}^{11} = (B_{\mathbf{k}}^{22})^* = 2KW_2 \cos k_x \cos k_y \tag{3.85}$$

$$B_{\mathbf{k}}^{12} = B_{\mathbf{k}}^{21} = (-JV_1 + 2KW_1)\,\gamma_{\mathbf{k}}, \tag{3.86}$$

where $\gamma_{\mathbf{k}} = \cos k_x + \cos k_y$ and

$$T = x^2 \tag{3.87}$$

$$V_1 = -2y^2x^2\cos(2\phi) \tag{3.88}$$

$$V_2 = x^4 e^{\mathrm{i}2\phi} + y^4 e^{-\mathrm{i}2\phi} \tag{3.89}$$

$$W_1 = -2x^4y^4\cos(4\phi) \tag{3.90}$$

$$W_2 = x^2y^2\left(x^4e^{\mathrm{i}4\phi} + y^4e^{-\mathrm{i}4\phi}\right). \tag{3.91}$$

Note that $T, V_1, W_1 \in \mathbb{R}$ and $V_2, W_2 \in \mathbb{C}$. Expression (3.82) can be diagonalized by a Bogoliubov transformation, $\beta_{\mathbf{k}}^\dagger = X_{\mathbf{k}}\gamma_{\mathbf{k}}^\dagger + Y_{\mathbf{k}}\gamma_{-\mathbf{k}}$, leading to a Bogoliubov eigenvalue equation of the form[26],

$$\begin{pmatrix} \hat{A}_{\mathbf{k}} & \hat{B}_{\mathbf{k}} \\ -\hat{B}_{\mathbf{k}}^* & -\hat{A}_{\mathbf{k}}^* \end{pmatrix} \begin{pmatrix} X_{\mathbf{k}}^{(n)} \\ Y_{\mathbf{k}}^{(n)} \end{pmatrix} = w_{\mathbf{k}}^{(n)} \begin{pmatrix} X_{\mathbf{k}}^{(n)} \\ Y_{\mathbf{k}}^{(n)} \end{pmatrix}, \tag{3.92}$$

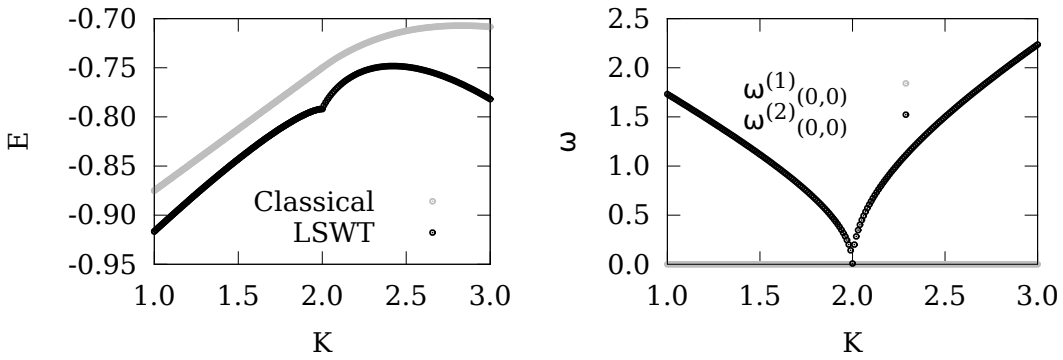

Figure 3.14: Left: Classical energy (black) and LSWT energy (gray) for $\mu = 0$ across the SF-CSF second order phase transition. Right: $w^{(1)}_{(0,0)}$ (gray) and $w^{(2)}_{(0,0)}$ (black) Bogoliubov modes across the same transition.

where SW dispersion relations are given by the two positive Bogoliubov eigenvalues, $w^{(2)}_{\mathbf{k}} \geq w^{(1)}_{\mathbf{k}} \geq 0$. Note that X and Y are 2×2 matrices. The LSWT correction to the classical energy is simply,

$$E_{SW} = \mathcal{E} - \sum_{\mathbf{k}} \mathrm{tr}\hat{A}_{\mathbf{k}} + \sum_{\mathbf{k}} \left(w^{(1)}_{\mathbf{k}} + w^{(2)}_{\mathbf{k}} \right). \tag{3.93}$$

In Fig. 3.14 we show the computed SW correction to the energy for the SF-CSF transition at $\mu = 0$. We observe that the transition becomes first order when adding the SW corrections, as we can distinguish a clear discontinuity in the first derivative of the energy. Note that the transition point is still placed at the very same value as it was in the classical approach, that is, at $K_c = 2$. Both the SF and the CSF are gapless ($w^{(1)}_{(0,0)} = 0$) and have a finite value of the $w^{(2)}_{(0,0)}$ excitation mode, which vanishes continuously at the critical point. Note that within the uniform SF phase, this $w^{(2)}_{(0,0)}$ mode would correspond to the (π, π) one-band SW dispersion mode, have not we performed a bipartition of the lattice.

Chapter 4

Benchmarking the Bose-Hubbard model

In this Chapter we present benchmark results of the CB Coherent ansatz (2.24) on the Bose-Hubbard model in the two-dimensinal square lattice. This simple model describes bosons moving over the lattice and interacting via repulsive contact interactions. An external chemical potential term regulates the total density of the system. It is the bosonic analog of the Hubbard model, which represents the prototypical example of a strongly correlated system characterized by the comptetion of the kinetic energy and strong repulsive interaction.

In the first section, we are introducing the model and studying the weakly and the strongly interacting limiting cases. In the former case, bosons delocalize and Bose condense in the $\mathbf{k} = \mathbf{0}$ forming a superfluid, while in the latter, the strong interaction prevents the bosons from condense leading to a Mott insulating phase characterized by the localization of bosons. For intermediate interactions the system undergoes a superfluid to insulator quantum phase transition. We present the celebrated phase diagram as a function of the chemical potential and hopping rate in units of the interaction, where the Mott phases present the characteristic lobe shape. We briefly review the relevant physics of both phases and comment on the low-lying Higgs and Goldstone excitations modes of the superfluid.

We present benchmark results of the first Mott lobe ($\rho = 1$) and show how the use of 2×2 clusters and the inclusion of CB fluctuations over the CB condensate improves the description of the phase diagram. The results are comptetitive with other state-of-the-art methods which imply the use of clusters, but at a fraction of their computational cost. We show how the CB Coherent wave function is able to capture the relevant physics of the Bose-Hubbard model. In particular, it well reproduces the particle-hole and Higgs-Goldstone excitation modes across the transition in

agreement with recent cold atom experimental results.

4.1 The Bose-Hubbard model

In the early days, the Bose-Hubbard model (BHM) was first proposed to describe ^{4}He atoms absorbed in porous media, or the dynamics of Cooper pairs hopping between superconducting grains via Josephson tunneling. More recently, it has become the paradigmatic example to describe cold atoms loaded in optical lattices, since the first cold atom implementation proposal [46]. The elementary degrees of freedom are spinless bosons and can be represented by a set of canonical bosonic operators, $\{a_i^\dagger, a_j\}$. The BHM has the form

$$H = -J \sum_{\langle ij \rangle} \left(a_i^\dagger a_j + \text{H.c.} \right) + \frac{U}{2} \sum_j n_j \left(n_j - 1 \right) - \mu \sum_j n_j, \tag{4.1}$$

where $n_j = a_j^\dagger a_j$ is the number operator. The first term in Eq. (4.1) accounts for the hopping of bosons between nearest neighbour sites of the lattice with tunneling amplitude J, the total density of the system is controlled by the chemical potential μ, and the contact on-site repulsive interaction has strength U. In the following, we will refer all quantities in units U.

The BHM conserves the total number of particles, $\hat{N} = \sum_j n_j$, and therefore it is invariant under a global $U(1)$ transformation with generator,

$$\hat{\mathcal{G}} = e^{\mathrm{i}\phi \sum_j n_j}. \tag{4.2}$$

In other words, the transformation of the creation and annihilation operators,

$$a_j^\dagger \to e^{-\mathrm{i}\phi} a_j^\dagger, \tag{4.3}$$

leaves (4.1) invariant.

The BHM is characterized by the competition of the hopping and on-site interaction. The hopping term favors the delocalization of bosons throughout the lattice and the onset of Bose-Einstein condensation (BEC), whereas the interaction favors a Mott insulating state where bosons are localized in each site of the lattice, preventing them to condense in the lowest energy mode ($\mathbf{k} = \mathbf{0}$). In particular, in the limit of vanishing hopping, $J \to 0$, the Hamiltonian is diagonal in the number occupation basis,

$$H = \frac{U}{2} \sum_j n_j \left(n_j - 1 \right) - \mu \sum_j n_j. \tag{4.4}$$

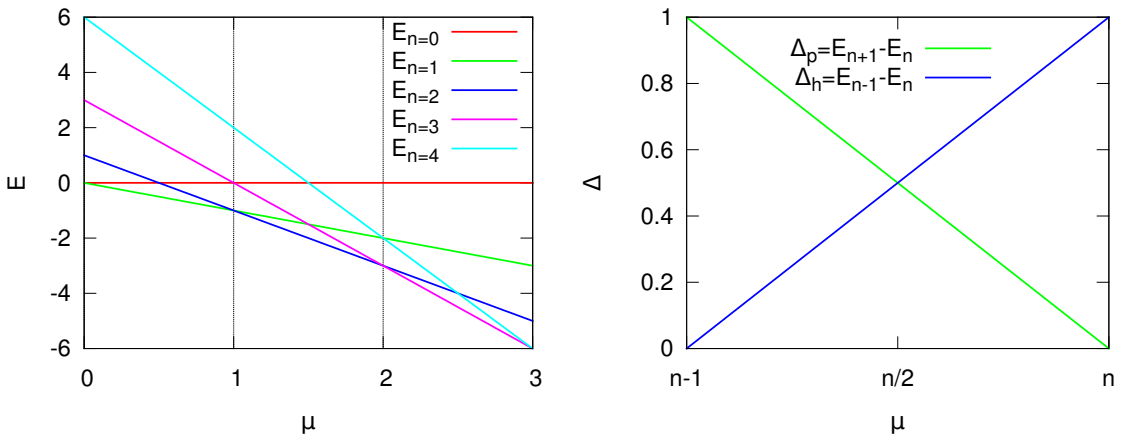

Figure 4.1: Left: Exact energies per site for various occupation numbers in the limit $J = 0$. Right: Particle and hole excitation gaps for the same limit. At half-integer values of the chemical potential, the gap is doubly degenerate.

The exact eigenstates of (4.4) are product states with an integer number of bosons per site,

$$|\Psi_n\rangle = \prod_j \frac{1}{\sqrt{n!}} \left(a_j^\dagger\right)^n |0\rangle. \tag{4.5}$$

Their corresponding eigenenergies are trivially obtained upon taking the expectation value of the Hamiltonian (4.4). In Fig. 4.1 we show the eigenenergies for different occupations as a function of the chemical potential. At integer values of the chemical potential, the two lowest eigenenergies cross, indicating a first order transition and a sudden change on the density of the system. The density remains constant within each Mott insulator phase, i.e., $\partial\rho/\partial\mu = 0$, and thus the system is incompressible. Also shown in Fig. 4.1 is the energy gap to the first excited state, which is either a particle- or a hole-like excitation. They have a lineal dependence with the chemical potential, and cross each other at half integer values of the chemical potential.

In the opposite limit of very weak interactions ($U/J \to 0$) the BHM (4.1) is diagonal in Fourier space,

$$H = \sum_{\mathbf{k}} \left(-2J\gamma_{\mathbf{k}} - \mu\right) n_{\mathbf{k}}, \tag{4.6}$$

where we have used $\gamma_{\mathbf{k}} = \cos(k_x) + \cos(k_y)$. In this limit, the exact ground state wave function is BEC in $\mathbf{k} = \mathbf{0}$ mode, where all atoms are spread over the whole system,

$$|\Psi_N\rangle = \frac{1}{\sqrt{N!}} \left(a_{\mathbf{k}=\mathbf{0}}^\dagger\right)^N |0\rangle. \tag{4.7}$$

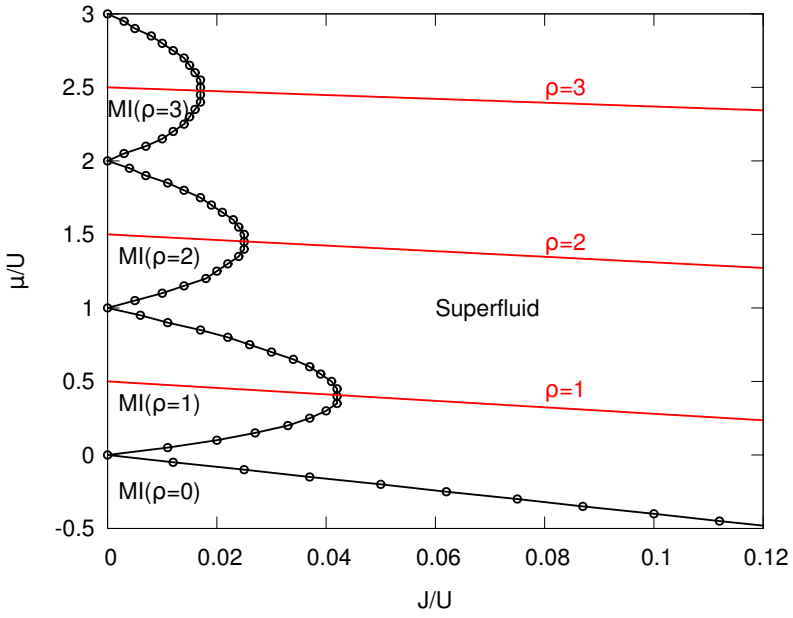

Figure 4.2: Phase diagram of the Bose-Hubbard model in two-dimensions as a function of the chemical potential (ordinates) and hopping amplitude (abscise) in units of the interaction strength obtained by standard mean-field (1×1 CB Gutzwiller). The integer density Mott insulator phases have a lobe shape. Straight red lines indicate the particle-hole symmetry line within the Mott phase and its extension to the integer density line in the superfluid (see text).

The energy per site of the wave function (4.7) is simply $E = (-4J - \mu)\rho$. In the thermodynamic limit, one can add a boson at an infinitesimally small cost in energy. In other words, it is gapless and compressible, i.e., $\partial\rho/\partial\mu \neq 0$.

Several analytical and numerical approaches have already been applied to the Bose-Hubbard model and given a thorough understanding of the physics of the Mott and superfluid phases and quantum phase transition. In particular, standard mean-field is able to obtain a qualitative phase diagram and the nature of the correlations within the Mott and superfluid phases [47, 48]. Fig. 4.2 displays the resulting phase diagram schematically. The Mott insulator phase extends over a superfluid region in a series of lobes around the $J = 0$ axis. Within each of these lobes, bosons tend to localize and to fill each lattice site with the same integer number of bosons. Nevertheless, except for the limit $J = 0$, there are quantum fluctuations on the local number of particles. Also shown in Fig. 4.2 is the *particle-hole symmetry line* (p-h line) that extends from the half-integer value of the chemical potential at $J = 0$ to the lobe tip in each of the Mott lobes. Along this line, the system particle- and hole-like

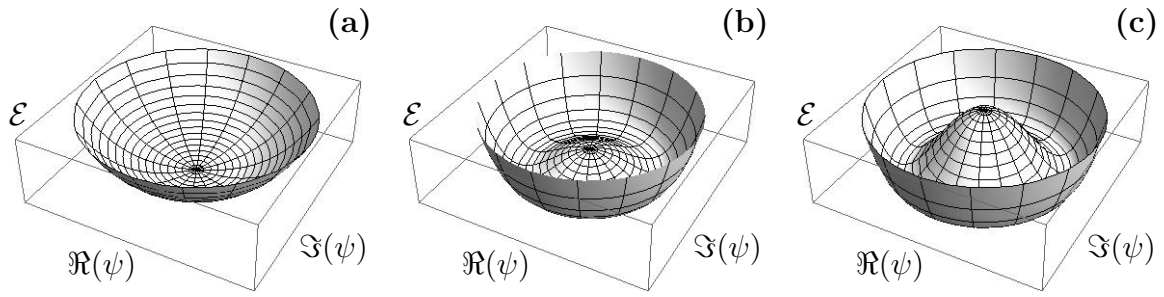

Figure 4.3: Effective energy ($\mathcal{E}$) of the effective $O(2)$ field theory describing the superfluid-to-Mott transition along the integer density line and particle-hole symmetry line as a function of the superfluid order parameter (ψ) in the complex plane $(\Re, \Im)$. (**a**): Deep in the Mott (symmetric) phase, $\psi = 0$ and the particle and hole excitations are degenerate. In the broken symmetry superfluid phase near the quantum critical point (**b**) and deep in the spuerfluid phase (**c**), the order parameter takes an arbitrary value of the degenerate minimum energy manifold.

excitations are degenerate. The p-h line extends over the superfluid region along a line of integer density, where the particle-hole symmetry does not hold anymore.

Along this line, the quantum phase transition is known to be of the XY universality class, while the rest of the phase borders belong to the ideal Bose gas [47]. The long wavelength physics of the superfluid-to-Mott transition along the integer density line can be effectively described by the family of $O(N)$ field theories with emergent particle-hole symmetry and Lorentz invariance [47, 49, 50, 51]. Being $O(2)$ the minimal model, one can write an effective action where the superfluid order parameter is a complex field with space and time dependence, $\psi(\mathbf{x}, t)$. In the broken symmetry phase (i.e., the superfluid), the effective energy has a "Mexican hat shape" as a function of the order parameter (see Fig.4.3). In the minimum, the order parameter acquires a nonzero value in the degenerate space. The excitation mode along the degenerate manifold is the costless Nambu-Goldstone mode, while the orthogonal and "costly" excitation is the amplitude or 'Higgs' mode. Reducing the hopping strength towards the quantum critical point along the constant density line, the Higgs excitation mode vanishes as we approach the critical point. In the symmetric phase (Mott), the order parameter is zero, and the two costly excitation modes (particle and hole) are degenerate.

In order to obtain quantitatively accurate descriptions of the phase diagram, different approaches have been considered. Specifically, dynamical mean-field theory [52], the cluster mean-field [53, 54], and more demanding numerical approaches, such as the variational cluster approximation [55, 56], and the numerically exact quantum

Monte Carlo [57]. The visibility of the Higgs mode near the quantum critical point has been studied in [58, 59, 60] by this latter technique. Experimentally, the superfluid to Mott transition has been probed in the laboratory by loading cold atoms in optical lattices [61]. Also in a cold atom experiment, the Higgs excitation mode has been recently unveiled [62].

In the following, we study the Bose-Hubbard model in the square lattice by means of the CB Coherent-Bogoliubov ansatz described in Chapter 2. We will see how the inclusion of the CB fluctuations over the simpler CB Gutzwiller ansatz increases the accuracy of the phase diagram, being competitive with other standard numerical techniques, and describes the collective exciation dispersions.

4.2 CB Coherent results

In this section we give results on the application of the CB coherent ansatz (2.24) to the Bose-Hubbard model on the square lattice. As explained in Chapter 2, we start by tiling the square lattice into clusters of shape $L \times L$ and then we map the Bose-Hubbard Hamiltonian (4.1) to the CB language. The CB Hamiltonian corresponing to the Bose-Hubbard model (4.1) has at most two-body CB terms. The one-body CB term comprises all on-site interactions, chemical potential, and hopping processes within the clusters. The two-body CB terms comprises uniquely the hopping processes between the edges of neighbouring clusters. The specific form of the $\hat{T}$ and $\hat{V}$ tensors of the Bose-Hubbard model (4.1) is written in Appendix 4.A.

In the following, we focus on the first Mott lobe and show the phase diagram, the densities and low-lying excitation dispersions using clusters of size 2×2. We benchmark the phase diagram with QMC results from Ref. [57], obtaining a good quantitative agreement. In addition, we compute the Higgs excitation mode along the constant density line, and the particle-hole excitation along the particle-hole symmetric line, in agreement with experimental results from Ref. [62].

4.2.1 Phase diagram

Within the Mott phase, the structure of the unitary transformation $\hat{U}$ and the CB condensed fraction σ^2 are independent of the chemical potential, μ. The structure of the condensed CB, which is dictated by the amplitudes $U^{\mathbf{g}}_{\mathbf{n}}$, is a linear combination of cluster states with total density equal to one,

$$|\mathbf{n}| = \sum_{i=1}^{L^2} n_i = L^2, \tag{4.8}$$

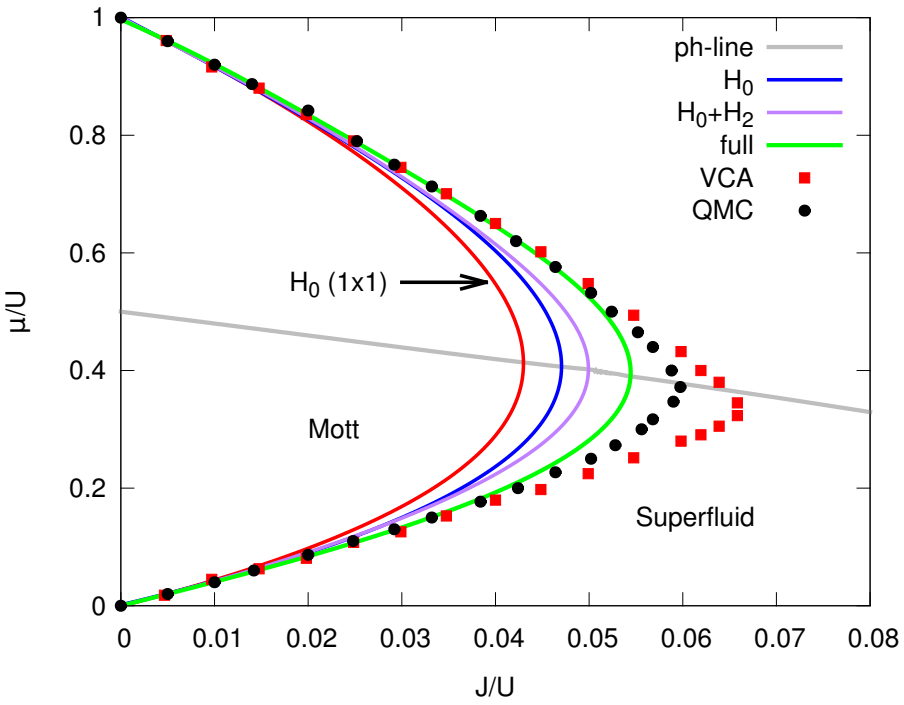

Figure 4.4: Phase diagram of the Bose-Hubbard model on the square lattice as a function of the hopping J and the chemical potential μ in units of the on-site interaction U obtained by means of the 2×2 CB Coherent-Bogoliubov wave function (2.24) in different approximations (see text), together with standard mean-field results (solid red line), QMC results from Ref. [57] (black circles) and VCA results from Ref. [55] (red squares). Also displayed is the particle-hole symmetric line, which continues along the constant density line in hte superfluid (solid gray).

where $\mathbf{n} = (n_1, \ldots, n_{L\times L})$ is a shorthand notation for a cluster configuration in the occupation basis. The relevant CB fluctuations which interact with the condensate flavor $\mathbf{g}$ are pairs of *particle* ($|\mathbf{n}| = L^2 + 1$) and *hole* ($|\mathbf{n}| = L^2 - 1$) cluster states. Particle- and hole-like excitation eigenvalues have a linear dependence on the chemical potential for fixed J, similar to the one shown in Fig. 4.1 for the exact limit $J = 0$. Both excitations cross each other at the *particle-hole (p-h) symmetry line*, where the gap is doubly degenerate. For a given value of J/U, the distance between the lower and upper phase border is double the value of the gap at the particle-hole symmetry line, which is placed at half this distance. The edges of the first Mott lobe are determined by the vanishing of the gap, indicating the appearance of a Goldstone mode at $\mathbf{k} = \mathbf{0}$ related to the $U(1)$ symmetry breaking in the superfluid, and the deviation from the total commensurate density $\rho = 1$.

In Fig. 4.4 we show the first Mott lobe of the Bose-Hubbard model in the square

lattice computed with the 2×2 CB Coherent-Bogoliubov wave function (2.24) with 2×2 clusters in three different levels of approximation, depending on the terms kept in the mean-field CB hamiltonian (2.35):

- H_0 corresponds to keep only the CB condensate terms (H_0) and neglect all CB fluctuations ($H_2 + H_4$). In this approximation, $\sigma^2 = 1$. It is equivalent to the 2×2 CB Gutzwiller approximation (see Sec. 2.3).

- $H_0 + H_2$ neglects two-body interactions among the CB fluctuations contained in the term H_4.

- $full$ refers to consider all terms in Eq. (2.35) and solve the full set of variational equations self-consistently, as described in Sec. 2.3.1. This approximation does not describe the gapless feature of the superfluid phase correctly. Although ways to correct this deficiency have been suggested [63], in the rest of the Chapter we will focus on the $H_0 + H_2$ approximation that strictly reproduces a gapless spectrum of the superfluid.

In addition, we have included for comparison the standard mean-field results, denoted by $H_0(1 \times 1)$ and QMC and VCA results from Ref.[57] and Ref. [55], respectively.

The 2×2 CB Gutzwiller approximation (H_0) reproduces the phase diagram obtained in Refs. [53, 54]. In this case, the edges of the Mott lobe are determined solely by a deviation from the commensurate density $\rho = 1$. The $H_0 + H_2$ approximation and the $full$ CB Coherent results go beyond the CB Gutzwiller or cluster mean-field approximations incorporating fluctuations by means of a self-consistent solution of the Bogoliubov and Hartree equations linked by the physical constraint, as explained in Section 2.3.1. As we include the self-consistent computation of CB fluctuations, the phase diagram obtained shows a clear convergence towards QMC results from Ref. [57]. VCA results, which were related in Ref. [55] to a linear approximate CB mapping, extend well beyond the QMC Mott lobe. Also shown in Fig. 4.4 is the extension of the particle-hole line into the superfluid phase characterized by density $\rho = 1$ and computed within the $H_0 + H_2$ approximation.

We have also computed the phase diagram with 1×1 CBs, that is equivalent to the standard mean-field result. The use of uncorrelated 2×2 clusters (H_0) already accounts for fluctuations which are not present in the 1×1 CB Gutzwiller approximation.

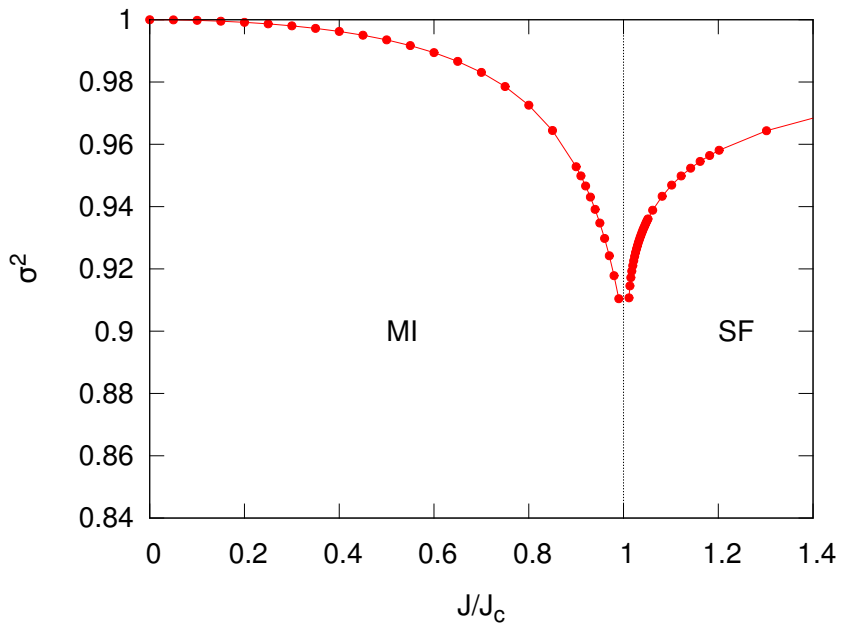

Figure 4.5: CB condensed fraction along the particle-hole symmetric line (MI) and its extension, the integer density ($\rho = 1$) line (SF) of the Bose-Hubbard model on the square lattice computed with 2×2 CB coherent ansatz in the $H_0 + H_2$ approximation.

4.2.2 CB Condensate fraction

In order to measure the amount of CB fluctuations over the CB condensate which are included by the 2×2 CB Coherent wave function in the $H_0 + H_2$ approximation we examine the CB condensed fraction along the particle-hole symmetry line within the Mott phase and its extension in the integer density line, within the superfluid phase. As $\sigma^2 = 1$ implies no CB fluctuations and the CB coherent wave function is equivalent to the CB Gutzwiller approximation which satisfies the physical constraint exactly, the deviation of σ^2 from unity will give us a qualitative measure of the degree of violation of the physical constraint when adding the CB fluctuations.

In Fig.4.5 we can see that the CB condensed fraction is of order $\sigma^2 \geq 0.95$ throughout almost the whole Mott lobe, while in the critical point (the lobe tip in Fig. 4.4) it suddenly collapses towards zero. At this point, the CB fluctuations diverge due to the diverging correlation length of both phases when approaching a critical point. It is remarkable that even in the superfluid phase the value of the condensed fraction is also in the order of $\sigma^2 \simeq 0.9$. This confirms that the most relevant fluctuations within the Mott lobe are already contained within the definition of the 2×2 CBs.

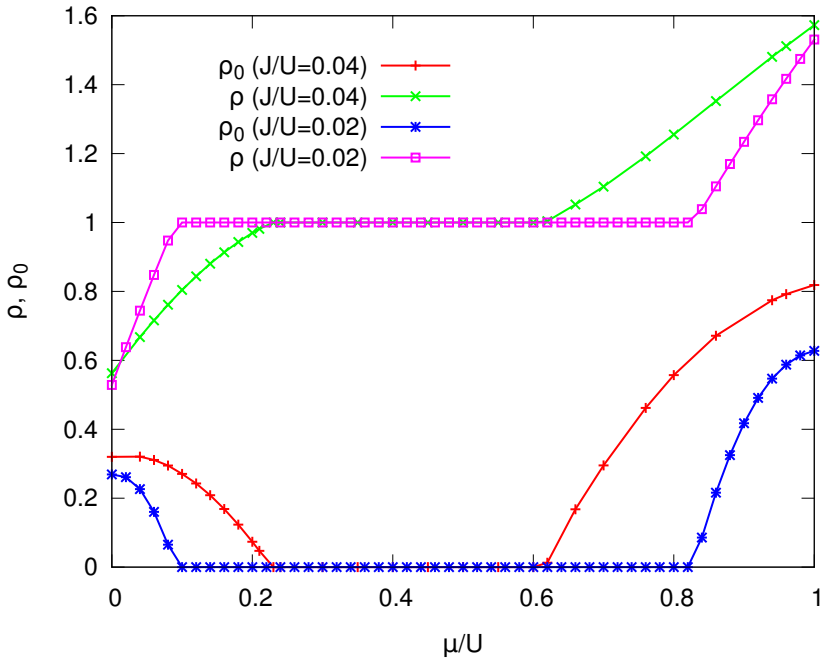

Figure 4.6: Total density and condensate density as a function of the chemical potential (μ) in units of the interaction strength for two values of the hopping rate $J/U = 0.02$ and $J/U = 0.04$. The condensate density vanishes within the Mott phase, and the total density presents a plateau at $\rho = 1$.

4.2.3 Total and condensate density

We also compute the total and condensate densities of the system, which gives us information about the order of the phase transition. In particular, we expect them to be continuous according to the previous theoretical predictions [47]. The condensate density is the order parameter signaling the onset of BEC and superfluid order.

The total density is $\rho = \sum_i \langle n_i \rangle / N$, which in terms of CBs,

$$\rho = \frac{1}{N} \sum_{\mathbf{R}} \sum_{i \in \mathbf{R}} \sum_{\alpha\beta} \langle \mathbf{R}\alpha | n_i | \mathbf{R}\beta \rangle \langle b^\dagger_{\mathbf{R}\alpha} b_{\mathbf{R}\beta} \rangle. \tag{4.9}$$

Assuming a uniform system and considering a C_4 symmetrized CB Coherent-Bogoliubov ansatz (2.24), the expectation value reduces

$$\rho = \langle \mathsf{g} | n_i | \mathsf{g} \rangle \sigma^2 + \frac{1}{M} \sum_{\mathbf{K}} \sum_{\alpha\beta \neq \mathsf{g}} \langle \alpha | n_i | \beta \rangle \langle b^\dagger_{\mathbf{K}\alpha} b_{\mathbf{K}\beta} \rangle, \tag{4.10}$$

where the site i of a 2×2 cluster can be chosen arbitrarily.

In the same way, we compute the density of bosons which condense in the $\mathbf{k} = \mathbf{0}$ mode, i.e., the *condensate density* $\rho_0 = \langle a^\dagger_{\mathbf{0}} a_{\mathbf{0}} \rangle / N$, which is the order parameter

which signals the onset of superfluidity. In the thermondynamic limit, it can be approximated by $\rho_0 = |\langle a_j^\dagger \rangle|^2$ which is, in terms of CBs,

$$\rho_0 \;=\; |\langle \mathsf{g}|a_i|\mathsf{g}\rangle \sigma^2 + \frac{1}{M}\sum_{\mathbf{K}}\sum_{\alpha\beta\neq\mathsf{g}} \langle\alpha|a_i|\beta\rangle \langle b^\dagger_{\mathbf{K}\alpha} b_{\mathbf{K}\beta}\rangle|^2 \tag{4.11}$$

where again the site i is chosen arbitrarily within the 2×2 cluster.

Fig. 4.6 displays the total and condensate densities for two fixed values of the hopping rate, $J/U = 0.02$ and $J/U = 0.04$. The plateau characterizing the Mott phase is reduced for larger J/U. Outside this region, the superfluid has non-commensurate density, except for the integer-density line (not shown). The condensate density of physical bosons, representing the coherence of the superfluid phase, vanishes in the Mott phase. VCA results for $J = 0.02$ [55, 56] compare well with our results.

4.2.4 Quasi-particle dispersions

The Bogoliubov diagonalization (2.89) provides us with information about the quasi-particle dispersions through its positive eigenvalues, $w^\alpha_{\mathbf{K}}$. Each of the flavors α corresponds to the dispersion band of an α quasi-particle. Thus, there are as many excitation bands as the number of cluster states kept in the computation within the cutoff.

In Fig. 4.7 we show the two lowest quasi-particle bands for three different points within the phase diagram Fig. 4.4 at hopping rate $J/U = 0.04$. In particular, at the p-h line in the Mott phase ($\mu_{ph} = 0.419$), away from the p-h line but still in the Mott phase ($\mu = 0.3$), and in the superfluid phase ($\mu = 0.12$). Within the Mott lobe, the two quasi-particle bands shown correspond to *particle*- and *hole*-like excitations. Notice the degeneracy of the particle and hole $\mathbf{K} = \mathbf{0}$ modes for the case $\mu_{ph} = 0.419$. Away from the p-h line and still in the Mott phase ($\mu = 0.3$), this degeneracy is broken and the hole band is favored against the particle band. Well inside the superfluid phase $\mu = 0.12$, we recognize the gapless mode (Goldstone) with the characteristic linear dispersion at low momentum $\mathbf{K}$, as well as a gapped band. Both are mixtures of particle- and hole-like excitations.

In Fig. 4.8 we display the particle-hole excitation gap $\Delta = w_{\mathbf{0}}^{(\mathsf{part.})} + w_{\mathbf{0}}^{(\mathsf{hole})}$ along the p-h line inside the Mott insulator and the Higgs excitation gap $\Delta = w_{\mathbf{0}}^{(\mathsf{H})}$ along the commensurate density $\rho = 1$ line in the superfluid computed with 2×2 CB Coherent wave function within the $H_0 + H_2$ approximation. Both the particle-hole and the Higgs gaps vanish at the critical point (tip lobe in Fig.4.4). In the superfluid region, the gapless Goldstone mode ($w_{\mathbf{0}}^G$) remains at zero (within numerical precision) while

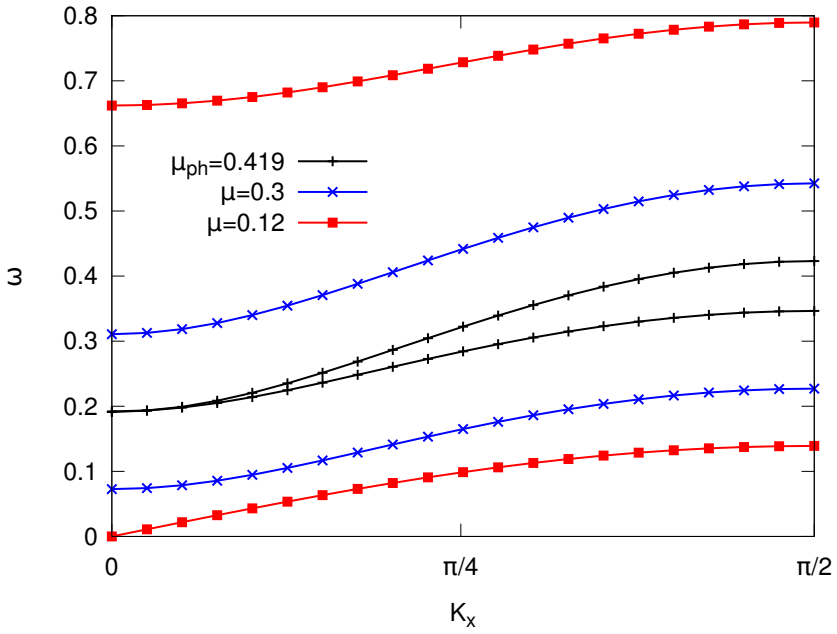

Figure 4.7: The two lowest-lying excitation dispersion bands for three different points in the phase diagram for a fixed hopping rate $J = 0.04$.

the Higgs grows for hopping rates $J/J_c > 1$, where $J_c = 0.499$ is the extrapolated value of the critical point computed with 2×2 CB Coherent wave function within the $H_0 + H_2$ approximation. Both modes are characterized by a structure that mixes particle- and hole-like states of the cluster.

4.3 Summary

In this chapter, we have shown benchmark results of the CB Coherent approach explained in Chapter 2 on the Bose-Hubbard model in two-dimensions. We have seen how the progressive inclusion of the CB fluctuations over the CB condensate yields the phase diagram to converge towards the QMC results. The use of clusters bigger than the single-site allows us to capture additional quantum correlations over the standard mean-field. Although the CB Coherent wave function does not preserve the physical constraint exactly, the CB fluctuations over the condensate are small both within the Mott and superfluid phases, as the condensate fraction remains close to $\sigma^2 \geq 0.9$. At the critical point, the CB fluctuations diverge and the CB approach is no longer valid. We have computed the low-excitation bands for several points within the Mott and superfluid phases. By inspecting the Bogoliubov eigenvectors we could

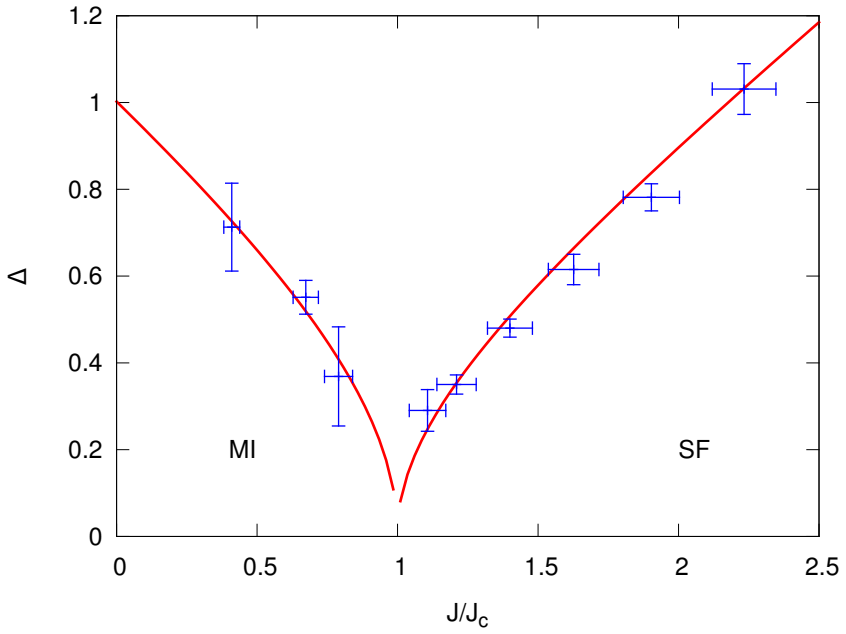

Figure 4.8: Higgs and Goldstone excitation modes across the superfluid to Mott transition along the integer density ($\rho = 1$) line in the superfluid (SF) and particle-hole symmetry line in the Mott insulator (MI). Solid red lines correspond to the 2×2 CB Coherent wave function within the $H_0 + H_2$ approximation (see text). The results obtained coincide (within error bars) with the experimental results from Ref. [62] displayed in blue points.

identify the nature of the excitations. In particular, the CB Coherent-Bogoliubov wave function (2.24) allows for the description of the Higgs and Goldstone modes across the transition, in remarkable agreement with experimental results.

Appendix

4.A CB Matrix elements of the Bose-Hubbard model

In this Appendix we give the explicit expression of the CB tensors $\hat{V}$ and $\hat{T}$ appearing in the CB Hamiltonian (2.10) for the Bose-Hubbard model (4.1) in two dimensions.

The two-body CB term in the Bose-Hubbard model is exclusively related to hopping processes between the edges of two nearest neighbour clusters. As the clusters comprises several lattice sites, $\hat{V}$ depends on the particular layout of the two clusters $\mathbf{R}$ and $\mathbf{R}'$ involved on the hopping process. Assuming that the ground state has no chiral order, we can take the unitary transformation $\hat{U}$ to be real, i.e. orthogonal. The specific form of the CB two-body tensor $\hat{V}$ for $L \times L$ clusters is

$$\begin{aligned}(V_{\mathbf{R}\mathbf{R}'})^{\alpha\alpha'}_{\beta\beta'} &= \sum_{\langle i\in\mathbf{R}, j\in\mathbf{R}'\rangle}\sum_{\mathbf{n},\mathbf{n}'}(\sqrt{n_i+1}\sqrt{n'_j}\; U^{\alpha}_{\mathbf{R}\{n_i+1\}}U^{\alpha'}_{\mathbf{R}'\{n'_j-1\}}U^{\beta}_{\mathbf{R}\mathbf{n}}U^{\beta'}_{\mathbf{R}'\mathbf{n}'} \\ &\quad + \sqrt{n_i}\sqrt{n'_j+1}\; U^{\alpha}_{\mathbf{R}\{n_i-1\}}U^{\alpha'}_{\mathbf{R}'\{n'_j+1\}}U^{\beta}_{\mathbf{R}\mathbf{n}}U^{\beta'}_{\mathbf{R}'\mathbf{n}'}), \end{aligned} \tag{4.12}$$

where $\sum_{\langle ij\rangle}$ runs over the L bonds between the edges of both clusters. Using compact notation, $\{n_i \pm 1\}$ corresponds to a configuration $\mathbf{n}$ with one more or one less boson at site i, that is, $\{n_i \pm 1\} \equiv (n_1, \ldots, n_i \pm 1, \ldots, n_{L^2})$.

For a general cluster of size $L \times L$, the intra-cluster matrix elements has both contributions, the hopping term and the Hubbard interaction,

$$\begin{aligned}(T_{\mathbf{R}})^{\alpha}_{\beta} &= \sum_{\mathbf{n}}\sum_{j\in\mathbf{R}}\left[\frac{1}{2}n_j\,(n_j-1) - \mu n_j\right]U^{\alpha}_{\mathbf{R}\mathbf{n}}U^{\beta}_{\mathbf{R}\mathbf{n}} \\ &\quad -J\sum_{\mathbf{n}}\sum_{\langle ij\rangle\in\mathbf{R}}(\sqrt{n_i+1}\sqrt{n_j}\; U^{\alpha}_{\mathbf{R}\{n_i+1,n_j-1\}}U^{\beta}_{\mathbf{R}\mathbf{n}} \\ &\quad + \sqrt{n_i}\sqrt{n_j+1}\; U^{\alpha}_{\mathbf{R}\{n_i-1,n_j+1\}}U^{\beta}_{\mathbf{R}\mathbf{n}}). \end{aligned} \tag{4.13}$$

Of course, for the limiting case of one-site cluster, no hopping proceses are present in the $\hat{T}$ matrix element. For a uniform and translational invariant system in the cluster superlattice, the unitary transformation U does not depend the on the cluster position $\mathbf{R}$.

4.B Hartree matrix

We have seen in Chapter 2 that the minimization of the free energy with respect to the condensed CB structure $U^{(\mathrm{g})}$ lead to the Hartree type eigensystem (2.18),

$$\sum_{\mathbf{n}} h_{\mathbf{m},\mathbf{n}}\, U^{\mathrm{g}}_{\mathbf{n}} \;=\; \sum_{\mathbf{n}} \Big[(h_0)_{\mathbf{m},\mathbf{n}} + (h_2)_{\mathbf{m},\mathbf{n}} \Big]\, U^{\mathrm{g}}_{\mathbf{n}} = \lambda U^{\mathrm{g}}_{\mathbf{m}}, \tag{4.14}$$

where we have made explicit distinction between the pure CB condensate contribution ($\hat{h}_0$) and the contribution comming from the interaction of the CB condensate with the CB fluctuations ($\hat{h}_2$). These come from the derivation of H_0 (3.67) and $\langle \hat{H}_2 \rangle$ (3.82) with respect to the variational parameters $U^{\mathrm{g}}_{\mathbf{n}}$, respectively. In particular, all the U^{g} dependence is contained in the tensors $\hat{T}$ (4.13) and $\hat{V}$ (4.12) of the Bose-Hubbard model.

Let us start by writing explicitly the matrix elements appearing in H_0 (3.67),

$$V^{\mathrm{gg}}_{\mathrm{gg}} \;=\; \frac{1}{2} \sum_{\langle i,j \rangle} \left(\sum_{\mathbf{n}} \sqrt{n_i + 1}\; U^{\mathrm{g}}_{\{n_i+1\}} U^{\mathrm{g}}_{\mathbf{n}} \right) \left(\sum_{\mathbf{n}'} \sqrt{n'_j + 1}\; U^{\mathrm{g}}_{\{n'_j+1\}} U^{\mathrm{g}}_{\mathbf{n}'} \right), \tag{4.15}$$

$$\begin{aligned} T^{\mathrm{g}}_{\mathrm{g}} \;=\; & \sum_{\mathbf{n}} \sum_{j} \left[\frac{1}{2} n_j \left(n_j - 1 \right) - \mu n_j \right] U^{\mathrm{g}}_{\mathbf{n}} U^{\mathrm{g}}_{\mathbf{n}} \\ & - J \sum_{\mathbf{n}} \sum_{\langle ij \rangle} (\sqrt{n_i + 1} \sqrt{n_j}\; U^{\mathrm{g}}_{\{n_i+1, n_j-1\}} U^{\mathrm{g}}_{\mathbf{n}} + \sqrt{n_i} \sqrt{n_j + 1}\; U^{\mathrm{g}}_{\{n_i-1, n_j+1\}} U^{\mathrm{g}}_{\mathbf{n}}). \end{aligned} \tag{4.16}$$

The corresponding derivatives with respect to the condensate CB structure U^{g} are

$$\begin{aligned} \frac{\partial}{\partial U^{\mathrm{g}}_{\mathbf{m}}} V^{\mathrm{gg}}_{\mathrm{gg}} \;=\; & \frac{1}{2} \sum_{\langle i,j \rangle} \left(\sqrt{m_i + 1}\; U^{\mathrm{g}}_{\{m_i+1\}} + \sqrt{m_i}\; U^{\mathrm{g}}_{\{m_i-1\}} \right) \left(\sum_{\mathbf{n}'} \sqrt{n'_j + 1}\; U^{\mathrm{g}}_{\{n'_j+1\}} U^{\mathrm{g}}_{\mathbf{n}'} \right) \\ & + \frac{1}{2} \sum_{\langle i,j \rangle} \left(\sum_{\mathbf{n}} \sqrt{n_i + 1}\; U^{\mathrm{g}}_{\{n_i+1\}} U^{\mathrm{g}}_{\mathbf{n}} \right) \left(\sqrt{m_j + 1}\; U^{\mathrm{g}}_{\{m_j+1\}} + \sqrt{m_j}\; U^{\mathrm{g}}_{\{m_j-1\}} \right) \\ \;=\; & \sum_{\langle i,j \rangle} \left(\sum_{\mathbf{n}} \sqrt{n_i + 1}\; U^{\mathrm{g}}_{\{n_i+1\}} U^{\mathrm{g}}_{\mathbf{n}} \right) \left(\sqrt{m_j + 1}\; U^{\mathrm{g}}_{\{m_j+1\}} + \sqrt{m_j}\; U^{\mathrm{g}}_{\{m_j-1\}} \right), \end{aligned} \tag{4.17}$$

and

$$\begin{aligned} \frac{\partial}{\partial U^{\mathrm{g}}_{\mathbf{m}}} T^{\mathrm{g}}_{\mathrm{g}} \;=\; & 2 \sum_{j} \left(\frac{1}{2} m_j \left(m_j - 1 \right) - \mu m_j \right) U^{\mathrm{g}}_{\mathbf{n}} \delta_{\mathbf{m},\mathbf{n}} \\ & - 2J \sum_{\langle ij \rangle} \left(\sqrt{m_i} \sqrt{m_j + 1}\; U^{\mathrm{g}}_{\{m_i-1, m_j+1\}} + \sqrt{m_i + 1} \sqrt{m_j}\; U^{\mathrm{g}}_{\{m_i+1, m_j-1\}} \right). \end{aligned} \tag{4.18}$$

Collecting terms, the CB condensate contribution to the Hartree matrix is

$$
\begin{aligned}
(h_0)_{\mathbf{m},\mathbf{n}} &= \sum_j \left[\frac{1}{2} m_j\,(m_j-1) - \mu m_j\right]\delta_{\mathbf{m},\mathbf{n}} \qquad (4.19)\\
&\quad -J\sum_{\langle ij\rangle}\left(\sqrt{m_i}\sqrt{m_j+1}\;\delta_{\mathbf{n},\{m_i-1,m_j+1\}} + \sqrt{m_i+1}\sqrt{m_j}\;\delta_{\mathbf{n},\{m_i+1,m_j-1\}}\right)\\
&\quad +\sigma^2\sum_{\langle ij\rangle}\left(\sum_{\mathbf{n}'}\sqrt{n'_i+1}\;U^{\mathtt{g}}_{\{n'_i+1\}}U^{\mathtt{g}}_{\mathbf{n}'}\right)\left(\sqrt{m_j+1}\;\delta_{\mathbf{n},\{m_j+1\}} + \sqrt{m_j}\;\delta_{\mathbf{n},\{m_j-1\}}\right).
\end{aligned}
$$

Following a similar procedure, we obtain the $\hat{h}_2$ contribution to the Hartree matrix (4.14). We write explicitly the $\hat{V}$ tensors and then their corresponding derivatives with respect to $U^{\mathtt{g}}$,

$$
\begin{aligned}
V^{\alpha\beta}_{\mathtt{g}\mathtt{g}} &= \frac{1}{4}\sum_{\langle ij\rangle}\sum_{\mathbf{n},\mathbf{n}'}(\sqrt{n_i+1}\sqrt{n'_j}\;U^{\alpha}_{\{n_i+1\}}U^{\beta}_{\{n'_j-1\}}U^{\mathtt{g}}_{\mathbf{n}}U^{\mathtt{g}}_{\mathbf{n}'}\\
&\qquad + \sqrt{n_i}\sqrt{n'_j+1}\;U^{\alpha}_{\{n_i-1\}}U^{\beta}_{\{n'_j+1\}}U^{\mathtt{g}}_{\mathbf{n}}U^{\mathtt{g}}_{\mathbf{n}'}), \qquad (4.20)\\
\frac{\partial}{\partial U^{\mathtt{g}}_{\mathbf{m}}}V^{\alpha\beta}_{\mathtt{g}\mathtt{g}} &= \frac{1}{4}\sum_{\langle ij\rangle}\sum_{\mathbf{n}}(\sqrt{n_i+1}\sqrt{m_j}\;U^{\alpha}_{\{n_i+1\}}U^{\beta}_{\{m_j-1\}}\\
&\qquad +\sqrt{n_i}\sqrt{m_j+1}\;U^{\alpha}_{\{n_i-1\}}U^{\beta}_{\{m_j+1\}} + [n\leftrightarrow m])U^{\mathtt{g}}_{\mathbf{n}}, \qquad (4.21)
\end{aligned}
$$

$$
\begin{aligned}
V^{\alpha\mathtt{g}}_{\mathtt{g}\beta} &= \frac{1}{4}\sum_{\langle ij\rangle}\sum_{\mathbf{n},\mathbf{n}'}(\sqrt{n_i+1}\sqrt{n'_j+1}\;U^{\alpha}_{\{n_i+1\}}U^{\mathtt{g}}_{\mathbf{n}'}U^{\mathtt{g}}_{\mathbf{n}}U^{\beta}_{\{n'_j+1\}}\\
&\qquad + \sqrt{n_i}\sqrt{n_j}\;U^{\alpha}_{\{n_i-1\}}U^{\mathtt{g}}_{\mathbf{n}'}U^{\mathtt{g}}_{\mathbf{n}}U^{\beta}_{\{n'_j-1\}}), \qquad (4.22)\\
\frac{\partial}{\partial U^{\mathtt{g}}_{\mathbf{m}}}V^{\alpha\mathtt{g}}_{\mathtt{g}\beta} &= \frac{1}{4}\sum_{\langle ij\rangle}\sum_{\mathbf{n}}(\sqrt{n_i+1}\sqrt{m_j+1}\;U^{\alpha}_{\{n_i+1\}}U^{\beta}_{\{m_j+1\}}\\
&\qquad + \sqrt{n_i}\sqrt{m_j}\;U^{\alpha}_{\{n_i-1\}}U^{\beta}_{\{m_j-1\}} + [n\leftrightarrow m])U^{\mathtt{g}}_{\mathbf{n}}, \qquad (4.23)
\end{aligned}
$$

$$
\begin{aligned}
V^{\alpha\mathtt{g}}_{\beta\mathtt{g}} &= \frac{1}{4}\sum_{\langle ij\rangle}\sum_{\mathbf{n}}\sqrt{n_i+1}\left(U^{\alpha}_{\{n_i+1\}}U^{\beta}_{\mathbf{n}} + U^{\alpha}_{\mathbf{n}}U^{\beta}_{\{n_i+1\}}\right)\\
&\qquad \times\left(\sum_{\mathbf{n}'}\sqrt{n'_j+1}\;U^{\mathtt{g}}_{\{n'_j+1\}}U^{\mathtt{g}}_{\mathbf{n}'}\right), \qquad (4.24)\\
\frac{\partial}{\partial U^{\mathtt{g}}_{\mathbf{m}}}V^{\alpha\mathtt{g}}_{\beta\mathtt{g}} &= \frac{1}{4}\sum_{\langle ij\rangle}\sum_{\mathbf{n}'}\sqrt{n'_i+1}\left(U^{\alpha}_{\{n'_i+1\}}U^{\beta}_{\mathbf{n}'} + U^{\alpha}_{\mathbf{n}'}U^{\beta}_{\{n'_i+1\}}\right)\\
&\qquad \times\left(\sqrt{m_j+1}\;U^{\mathtt{g}}_{\{m_j+1\}} + \sqrt{m_j}\;U^{\mathtt{g}}_{\{m_j-1\}}\right). \qquad (4.25)
\end{aligned}
$$

Making use of these derivatives, the CB condensate fluctuations contribution to the Hartree matrix (4.14) is

$$
\begin{aligned}
(h_2)_{\mathbf{m},\mathbf{n}} &= \frac{1}{4M}\sum_{\langle ij\rangle}\sum_{\alpha\beta}(\sqrt{n_i+1}\sqrt{m_j}\;U^{\alpha}_{\{n_i+1\}}U^{\beta}_{\{m_j-1\}} \\
&\quad + \sqrt{n_i}\sqrt{m_j+1}\;U^{\alpha}_{\{n_i-1\}}U^{\beta}_{\{m_j+1\}} + [n\leftrightarrow m])\sum_{\mathbf{K}}\gamma_{\mathbf{k}}K_{\mathbf{K}\alpha\beta} \\
&+ \frac{1}{4M}\sum_{\langle ij\rangle}\sum_{\alpha\beta}(\sqrt{n_i+1}\sqrt{m_j+1}\;U^{\alpha}_{\{n_i+1\}}U^{\beta}_{\{m_j+1\}} \\
&\quad + \sqrt{n_i}\sqrt{m_j}\;U^{\alpha}_{\{n_i-1\}}U^{\beta}_{\{m_j-1\}} + [n\leftrightarrow m])\sum_{\mathbf{K}}\gamma_{\mathbf{K}}P_{\mathbf{K}\alpha\beta} \\
&+ \frac{1}{2M}\sum_{\langle ij\rangle}\sum_{\alpha\beta}\sum_{\mathbf{n}'}\sqrt{n'_i+1}\left(U^{\alpha}_{\{n'_i+1\}}U^{\beta}_{\mathbf{n}'}+U^{\alpha}_{\mathbf{n}'}U^{\beta}_{\{n'_i+1\}}\right) \\
&\quad \times\left(\sqrt{m_j+1}\;\delta_{\mathbf{n},\{m_j+1\}}+\sqrt{m_j}\;\delta_{\mathbf{n},\{m_j-1\}}\right)\sum_{\mathbf{K}}P_{\mathbf{K}\alpha\beta}, \qquad (4.26)
\end{aligned}
$$

where we have made use of the density ($\hat{P}_{\mathbf{K}}$) and pairing ($\hat{K}_{\mathbf{K}}$) tensors defined in (2.92) and (2.93), respectively. We have introduced the global physical constraint (2.6) by means of a Lagrange multiplier λ. We have introduced $\gamma_{\mathbf{Q}}=\sum_{\hat{\mathbf{u}}}\cos(\mathbf{Q}\cdot\hat{\mathbf{u}})$, after having symmetrized the two-body CB matrix elements $\hat{V}=(1/4)\sum_{\pm\hat{\mathbf{u}}}\hat{V}_{\hat{\mathbf{u}}}$ to preserve the C_4 symmetry of the superlattice.

Chapter 5

Cold atoms in the presence of synthetic gauge fields

In this Chapter we present results on the zero-temperature ground state phase diagram of strongly-interacting bosons in the presence of a density dependent π-flux synthetic gauge field in two-dimensions by means of the CB Gutzwiller ansatz presented in Chapter 2. Being a two-leg ladder the minimal geometry for which the synthetic gauge field emulates a uniform magnetic flux traversing the plaquettes, we first compute its ground state and study its evolution to the two dimensional limit by also computing the four-leg ladder geometry. In ladder geometries, the system exhibits integer and fractional filling Mott insulating phases, chiral superfluid and a supersolid phase characterized by the coexistence of the superfluid order and (π) charge density wave order (CDW) along the legs. In two dimensions, the integer Mott lobes and part of the region of supersolid prevail, whereas the fractional lobes disappear giving rise to a wide region of chiral superfluid characterized by a fully packed checkerboard pattern of vortex-antivortex pairs. These results suggest that cold atoms in the presence of density dependent gauge field may open a new possibility for the experimental realization of the long-sought supersolid phase.

5.1 The Bose-Hubbard model with synthetic gauge fields

The dynamics of neutral atoms in the pressence of a uniform [64, 65] or staggered [66, 67] static magnetic gauge fields can be emulated by inducing Raman assisted tunneling between different internal states of the atoms [68] resulting in a complex hopping rate, $J = |J|e^{i\theta}$, where θ is the Peierls phase. These techniques have allowed for the experimental realization of weakly interacting gases exhibiting the Hof-

stadter spectrum [64], or the Meissner-to-vortex transition characteristic of a type-II superconductor [69], among others. Moreover, in the strongly-interacting regime, the synthetic gauge fields are expected to lead to different intermediate exotic Mott insulating phases characterized by the presence of chirality [70, 71].

The periodic modulations of the optical lattices near Feshbach resonances results in a nonlineal dependence of the hopping rates with the occupation of the sites involved in the hopping process [72]. The dynamical feedback between matter and gauge fields can be emulated by combining the Raman assisted tunneling which generates the artificial gauge fields, with a periodical modulation of the optical lattice near a Feshbach resonance [73]. This combination results in a density dependent Peierls phase that is expected to produce one-dimensional statistically-induced phase transitions [74] and the emergence of fractional filling Mott lobes at vanishing interaction [73]. The two-dimensional extension of these systems may be realized experimentally by tilting the former one-dimensional lattice, inducing an additional row dependence to the Peierls phase, which results in an effective uniform finite density dependent flux per plaquette.

In our case, we generate a 2D model by disposing a 1D Bose-Hubbard chain with density dependent hoppings vertically and tilting it horizontally. This results in an anisotropic Bose-Hubbard Hamiltonian of the form,

$$\begin{aligned} H &= -\frac{U}{2}\sum_{\mathbf{r}}\hat{n}_{\mathbf{r}}\left(\hat{n}_{\mathbf{r}}-1\right)-\mu\sum_{\mathbf{r}}\hat{n}_{\mathbf{r}} \\ &\quad -J_x\sum_{\mathbf{r}}\left(a^{\dagger}_{\mathbf{r}+x}a_{\mathbf{r}}+\text{H.c.}\right) \\ &\quad -J_y\sum_{\mathbf{r}}\left(a^{\dagger}_{\mathbf{r}+y}e^{-\mathrm{i}\varphi_x\hat{n}_{\mathbf{r}}}a_{\mathbf{r}}+\text{H.c.}\right), \end{aligned} \tag{5.1}$$

where $a^{\dagger}_{\mathbf{r}}$ ($a_{\mathbf{r}}$) creates (annihilates) a boson at site $\mathbf{r}=(r_x,r_y)$ of the square lattice. The first three terms are the usual Hubbard on-site density-density interaction of strength U, the chemical potential term (μ) which regulates the total density of the system, and a hopping term along the x-direction (J_x). The hopping of bosons in the y-direction has a rate modulated by the density dependent Peierls phase, where $\varphi_x=\varphi r_x$. As mentioned earlier, this phase induces a net flux per plaquette of value φ, which now depends on the density. Loosely speaking, the density dependence of the Peierls phase reduces the number of hopping processes with complex hopping rate to those that involve states with local densities greater than one.

The Hamiltonian (5.1) possess global $U(1)$ symmetry and it is translational invariant. The periodicity in the x-direction is larger than the lattice constant for a

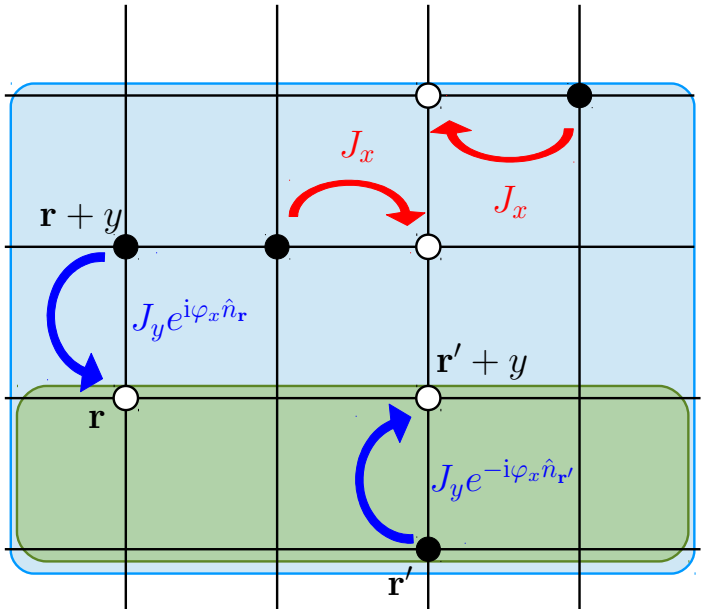

Figure 5.1: Schematic representation of the hopping terms of Hamiltonian (5.1) in two dimensions. Filled (empty) circles represent the initial (final) state for a hopping process of magnitude J_x or J_y. The Peierls phase in the y-direcion favors bond-chiral order. The two-leg (shaded green) and four-leg (shaded blue) ladder geometries are constructed from the 2D model by taking two and four legs along the x-direction.

nonzero flux, given by the relation $T_x = 2\pi x/\varphi$, where x is the lattice constant along the x-direction. For the π-flux, this period is $T_x = 2x$. The reflection symmetry is preserved along the x-direction, whereas the density dependent Peierls phase breaks it along the y-direction, as the hopping always depends on the occupation of the lowest site of a bond (see Fig. 5.1).

In the fully anisotropic case $J_x = 0$, the Hamiltonian (5.1) describes a set of uncoupled 1D anyon-Hubbard chains. In particular, in the saturated π-flux limit, half of these 1D anyon chains can be exactly mapped to 1D spinless fermion Hubbard chains via a Jordan-Wigner transformation, whereas the other half is simply the Bose-Hubbard model in 1D. The evolution of the ground state phase diagram in this 1D limit with the flux φ has been studied in Ref. [74] by means of the DMRG method. There, they have found that the $\rho = 1$ bosonic Mott lobe broadens while tuning the flux from $\varphi = 0$ (bosons) to $\varphi = \pi$ (spinless fermions). In addition, when a harmonic trap was added to the system, they found an additional Mott plateau with $\rho \simeq 1/2$ at $J_y/U = 0.5$.

Notice that if the Peierls phase was not density dependent, i.e. replacing the number operator by a constant ($\hat{n}_j = 1$), the Hamiltonian (5.1) would recover the C_4

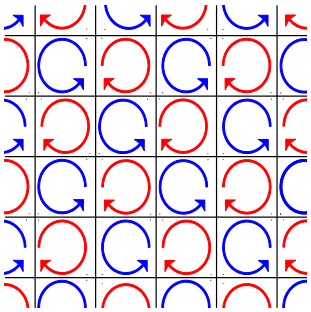

Figure 5.2: Schematic design of the fully packed checkerboard pattern of vortex-antivortex pairs of the chiral superfluid (CSF).

symmetry for a π-flux by implementing a local gauge transformation of the form,

$$a^{\dagger}_{\mathbf{r}} \rightarrow a^{\dagger}_{\mathbf{r}} e^{-\mathrm{i}\varphi r_x r_y}, \tag{5.2}$$

in the isotropic limit $J_x = J_y$.

The non density dependent case has been studied for the anisotropic two-leg ladder geometry by means of bosonization techniques [71, 75, 76] and DMRG [70]. In the weakly-interacting regime, the vortex to Meissner phase transition predicted as a function of the flux, has been recently experimentally probed [69]. Analogously to the type-II superconductors, for small values of the magnetic flux, the Meissner phase of cold atoms is characterized by having opposite currents along the legs of the ladder and vanishing current along the rungs. The net current along the ladder has a linear dependence with the flux. Near half of the saturation value ($\varphi \simeq \pi/2$) a phase transition towards the vortex phase occurs, and the net current starts to decrease exponentially till the saturation value $\varphi = \pi$, where the net current is zero [75]. In this phase, the system is permeable to the magnetic flux, hosting a series of vortices of the size of several plaquettes. In the limit $\varphi = \pi$, the vortex superfluid is the chiral superfluid of fully stacked vortex-antivortex pairs (see Fig. 5.2).

In the following, we present results on the CB Gutzwiller ansatz approach to the density dependent Peierls phase Hamiltonian (5.1) in two-dimensions. We study the anisotropic case of $J_y = 2J_y$ in order to enhance the density dependent Peierls processes along the y-direction. Given the periodicity of the lattice imposed by the π-flux, a 2×2 cluster would suffice to describe the phases. In addition, we will use 2×4 and 4×2 clusters in order to include more quantum correlations exactly. In the two-leg ladder, we obtain the usual Mott lobes at integer fillings, and a fractional Mott lobe at filling $\rho = 1/2$, induced by the anisotropy, as has been already pointed

out in [77]. The superfluid region coexists with CDW order for $\rho < 1$ and chiral order for $\rho > 1$. As we approach the two-dimensional limit, more fractional Mott lobes appear in accordance with QMC results [78] but they are narrower, disappearing in the two-dimensional limit, and leading to a chiral superfluid region, while the striped supersolid survives. Contrary to the chiral superfluid obtained in the J-K model (Chapter 3), in this case the bond-currents form a checkerboard pattern of vortices-antivortices through the lattice.

5.2 CB Gutzwiller results

In order to map out the phase diagram, we compute several observables and order parameters. In particular, the total density of the system, the charge density wave order parameter, bond-currents, and the density of Bose-Einstein condensed bosons, which signals the onset of superfluid order.

The charge density wave order is signaled by finite peaks in the quasi-momentum distribution of the density-density scattering matrix, $S(\mathbf{q}) \propto \sum_{ij} e^{-\mathrm{i}(\mathbf{r}_i - \mathbf{r}_j)} \langle \hat{n}_i \hat{n}_j \rangle$. Within the CB Gutzwiller approach in the thermodynamic leads to

$$\rho_{CDW}(\mathbf{q}) = \frac{1}{L_x L_y} \sum_{\mathbf{r} \in \square} e^{-\mathrm{i}\mathbf{q}\mathbf{r}} \langle \Phi | \, \hat{n}_{\mathbf{r}} \, | \Phi \rangle \, . \tag{5.3}$$

The total density of the system is the uniform distribution of the density, given by $\rho = \rho_{CDW}(\mathbf{0})$.

The onset of BEC is signaled by the peaks in the one-body correlation, $S(\mathbf{q}) \propto \sum_{ij} e^{-\mathrm{i}(\mathbf{r}_i - \mathbf{r}_j)} \langle a_i^\dagger a_j \rangle$, which in the CB Gutzwiller approach leads to

$$\rho_{\mathsf{c}}(\mathbf{q}) = \frac{1}{L_x L_y} | \sum_{\mathbf{r} \in \square} e^{-\mathrm{i}\mathbf{q}\mathbf{r}} \langle \Phi | \, a_{\mathbf{r}}^\dagger \, | \Phi \rangle \, |^2 . \tag{5.4}$$

in the thermodynamic limit. As the CB Gutzwiller wave function is a product of equivalent clusters, the available momenta $\mathbf{q}$ in both (5.3) and (5.4) are constrained by the size of the cluster. In two dimensions, for an $L_x \times L_y$ cluster, $q_u = 0, 2\pi n_u / L_u, \; n_u = 0, L_u$ for each direction u.

In ladder geometries, which are quasi-one-dimensional, CDW and condensate densities per leg of the ladder are defined as

$$\rho_{CDW}(q_x, r_y) = \frac{1}{L_x L_y} \sum_{r_x \in \square / r_y} e^{-\mathrm{i}q_x r_x} \langle \Phi | \, \hat{n}_{\mathbf{r}} \, | \Phi \rangle \, , \tag{5.5}$$

where the sum is restricted to the sites of the cluster lying on the leg r_y. And, the condensate density is

$$\rho_{\mathsf{c}}(q_x, r_y) = \frac{1}{l_x l_y} \sum_{r_x \in \square / r_y} e^{-\mathrm{i} q_x r_x} \langle \Phi | \, a^\dagger_{\mathbf{r}} \, | \Phi \rangle \, . \tag{5.6}$$

We also compute the expectation value of the bond-currents over the lattice. These can be defined through the time evolution of the density at each point of the lattice,

$$\frac{\partial \hat{n}_{\mathbf{r}}}{\partial t} = \mathrm{i} \, [H, \hat{n}_{\mathbf{r}}] = \sum_{\delta} \hat{\mathcal{J}}_{\mathbf{r}, \mathbf{r}+\delta}, \tag{5.7}$$

where δ runs over the nearest neighbour sites, and $\hat{\mathcal{J}}_{\mathbf{r},\mathbf{r}+\delta}$ are the bond-current operators. Explicitly,

$$\hat{\mathcal{J}}_{\mathbf{r},\mathbf{r}+x} = \mathrm{i} \left(a^\dagger_{\mathbf{r}} a_{\mathbf{r}+x} - \mathrm{H.c.} \right), \tag{5.8}$$

$$\hat{\mathcal{J}}_{\mathbf{r},\mathbf{r}+y} = \mathrm{i} \left(a^\dagger_{\mathbf{r}} e^{-\mathrm{i}\varphi \hat{n}_{\mathbf{r}} r_x} a_{\mathbf{r}+y} - \mathrm{H.c.} \right), \tag{5.9}$$

where we have expressed them in units of the hopping amplitudes J_x and J_y, respectively. We can define a bond-chiral order parameter as the sum of the bond-chiral currents over the whole lattice,

$$\Omega = \frac{1}{N_b} \sum_{\langle \mathbf{r}, \mathbf{r}' \rangle} | \langle \Psi | \, \mathcal{J}_{\mathbf{r},\mathbf{r}'} \, | \Psi \rangle |, \tag{5.10}$$

where N_b is the number of bonds of the lattice. Similarly as we did in Chapter 3, the computation of the bond-currents will depend on the position of the bond with respect to the tiling performed over the original lattice.

Figire 5.3 displays the condensate density $\rho_{\mathsf{c}}(\mathbf{q} = \mathbf{0})$ for the two- and four-leg ladders and the 2D square lattice computed with CB Gutzwiller 4×2, 2×4 and 2×4, respectively. For a non density dependence Peierls phase (**a1**, **a2**, **a3**) the ladder geometry favors fractional filling Mott lobes conmensurate with the number of legs, in accordance with the QMC study [78]. These fractional Mott lobes tend to narrow as the number of legs is increased, and disappear in the 2D limit. Out from the Mott lobes, there is a chiral superfluid phase which is characterized by the coexistence of superfluid order and bond-chiral order (not shown). The density dependence of the Peierls phase suppresses the fractional Mott lobes of density $\rho < 1$ (see Fig. 5.3 **b1**, **b2**, **b3**) and the chiral order of the superfluid, leading to a supersolid, as it can be seen in Figure 5.4.

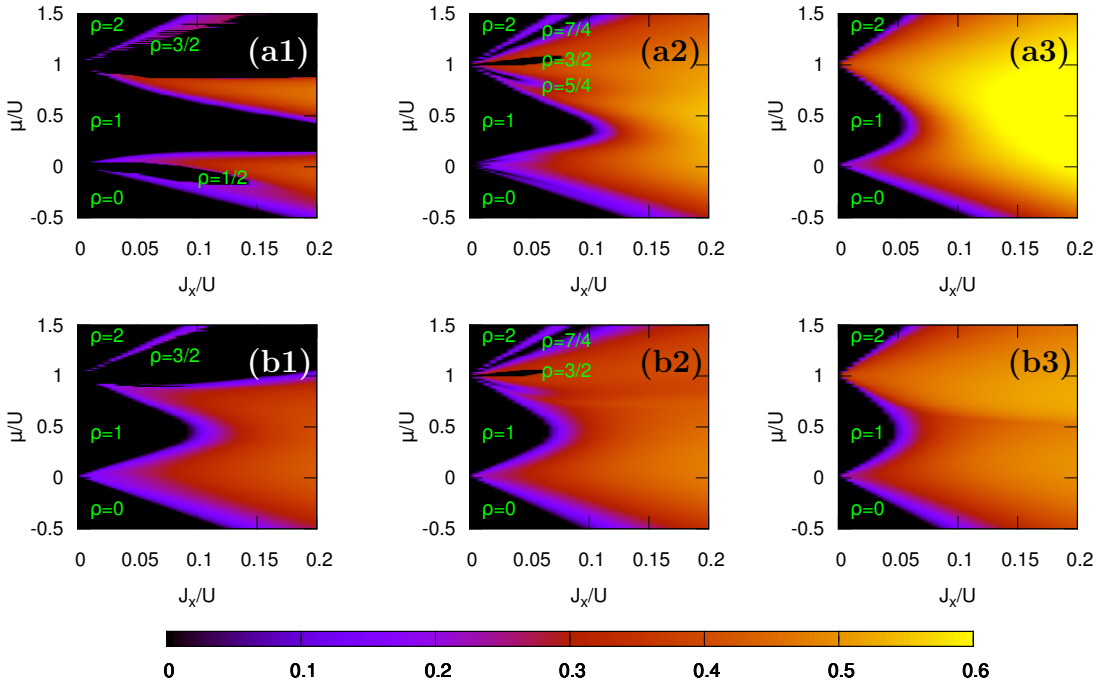

Figure 5.3: Condensate density $\rho_c(0)$ for the two-leg ladder, the four-leg ladder and the 2D square lattice with non density dependent (**a1**, **a2**, **a3**) and density dependent (**b1**, **b2**, **b3**) π-flux Peierls phase computed with a CB Gutzwiller of cluster size 4×2 (**a1, b1**) and 2×4 (**a2, b2, a3, b3**). The total density of the Mott lobes is indicated in green.

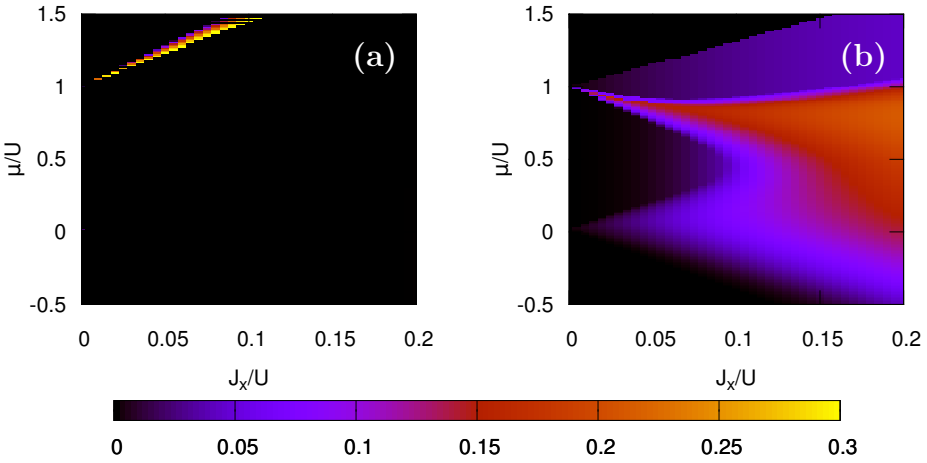

Figure 5.4: Bond-chiral order parameter (**a**) and left-leg (π) CDW order parameter (**b**) for the two-leg ladder computed with CB Gutzwiller with clusters of size 4×2.

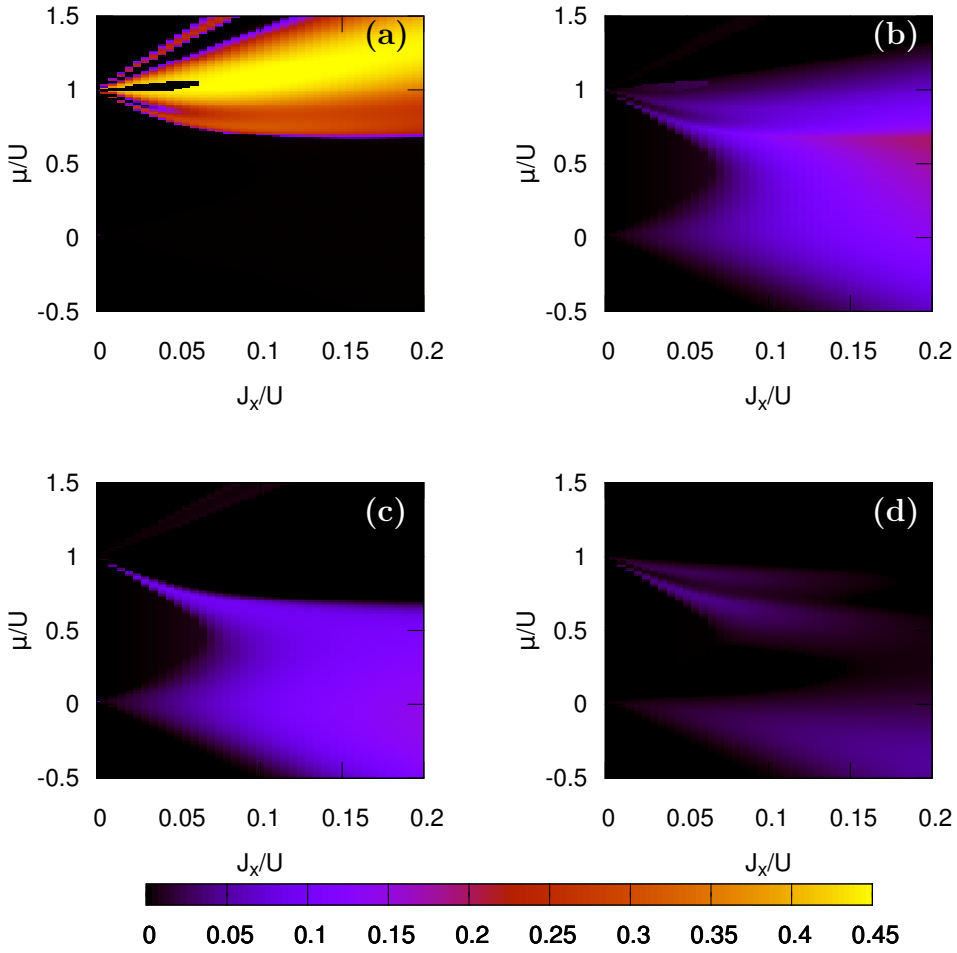

Figure 5.5: Bond-chiral order parameter (**a**) and (π) CDW order parameter for the first (**b**), second (**c**) and fourth (**d**) legs of a four-leg ladder computed with CB Gutzwiller with a cluster of size 2×4.

Figure 5.4 shows bond-chirality (5.10) and condensate density (5.6) of the lower-leg of the two-leg ladder computed with CB Gutzwiller 4×2. We can appreciate that the chiral order of the superfluid has been reduced to a very narrow region between the $\rho = 3/2$ lobe and the fully occupied $\rho = 2$ lobe. The superfluid phase has now CDW order along the lower leg. Interestingly, the $\rho = 3/2$ phase has a nonzero value of the CDW in the lower leg of the ladder. This inbalance is caused by the fact that, for the particular case of the two-leg ladder geometry, the density dependence of the Peierls phase is always evaluated on the sites of the lower leg.

Figure 5.5 shows the bond-chiral order parameter and the CDW density for three of the legs of the four-leg ladder computed with CB Gutzwiller 2×4 for the four-leg

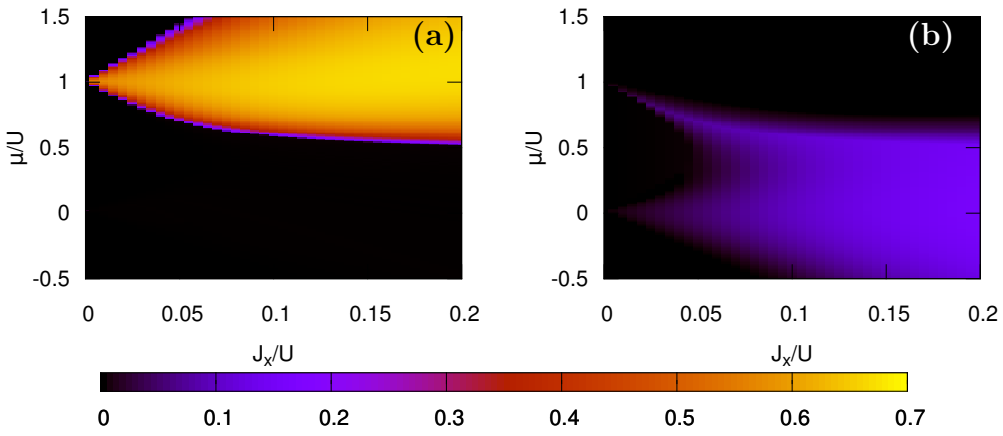

Figure 5.6: Bond-chiral order (**a**) and $(\pi, 0)$ CDW order parameter (**b**) for the 2D system computed with CB Gutzwiller 2×4.

ladder geometry of Hamiltonian (5.1). The $\rho = 3/2$ Mott lobe present in the two-leg ladder leads to the appearance of four Mott lobes with densities $\rho = 5/4, 3/2, 7/4$ and no chiral order. They are surrounded by a chiral superfluid phase which has some nonzero CDW order along the lowest leg (**b**). The rest of the superfluid phase coexists with CDW order. Analogously to the two-leg ladder, the highest leg does not possess CDW order, due to the absence of reflexion symmetry along the y direction induced by the density dependent Peierls phase.

In Figure 5.6 we show the bond-chiral order parameter and the $(\pi, 0)$ CDW order parameter for the 2D lattice computed with CB Gutzwiller 2×4 with density dependent Peierls phase. The narrow CSF phase which appeared in the two-leg ladder geometry now extends over half the region of the superfluid phase $\rho > 1$. The lower region of the superfluid $\rho < 1$ is characterized by the presence of CDW order, indicating the onset of supersolid order. The $(0, \pi)$ and (π, π) CDW orders are null over all the phase diagram.

5.3 Summary

In this Chapter we have presented CB results on the order parameters and observables of a system of strongly interacting bosons in the presence of π-flux density dependent synthetic gauge fields by means of the CB Gutzwiller approach presented in Chapter 2. We have studied the anisotropic case $J_y = 2J_x$ in order to enhance the hoppings with the Peierls-modulated phase and studied the effect of the density dependence

in two- and four-leg ladders and in two-dimensions as compared to the non density dependent case.

Taking into account the magnetic cell imposed by the π-flux in the Hamiltonian (5.1), we have used clusters of dimensions conmensurable with the magnetic cell, i.e. 2×2, 4×2 and 2×4. The tentative ground state phase diagram obtained on basis of the order parameters and observables is already mapped out by 2×2 clusters (not shown). We have shown results making use of larger clusters (4×2 and 2×4) in order to assess the stability of the phases obtained with 2×2 clusters, and to include more quantum correlations exactly. However, a careful analysis of the energy obtained by CB Gutzwiller and its derivatives across the transitions must be carried on in order to precise the phase borders and the order of the transitions.

In ladder geometries, we have obtained a series of fractional integer density Mott lobes which are conmensurate with the number of legs, in accordance with QMC results [78]. As the number of legs is increased, the factional Mott lobes narrow, disappearing in the two-dimensional limit. The density dependence of the Peierls phase supresses the fractional Mott lobes with $\rho < 1$ leading to a $(\pi, 0)$ supersolid in 2D and streches the chiral superfluid already present for the non density dependent case to the $\rho > 1$ region of the superfluid.

The feasible experimental realization of the density dependent synthetic gauge fields opens the new possiblity to probe in the laboratory the long-sought supersolid phase.

Chapter 6

Benchmarking the Hubbard model

In this Chapter we present benchmark results on the Hubbard model at half-filling by means of the composite fermion-boson mean-field schemes presented in Chapter 2. We compute the energy and double occupancy of fermions by using clusters of up to $N_\square = 6$ sites in one- and two-dimensions, obtaining an accurate description of the Mott insulating phase. Although the composite particle ansatze employed are not able to describe the metallic phase, the method can be combined with the standard Hartree-Fock method to estimate the transition point. We discuss possible alternatives to improve over this limitation.

6.1 The Hubbard model at half-filling

The Hubbard model is the prototypical example of a strongly correlated system characterized by the competition of the strong particle interaction and the kinetic energy. The Hubbard model has the following explicit form,

$$H = -t \sum_{\langle i,j \rangle} \sum_{\sigma} (c^\dagger_{i,\sigma} c_{j,\sigma} + c^\dagger_{j,\sigma} c_{i,\sigma}) + U \sum_i n_{i\uparrow} n_{i\downarrow} - \mu \sum_i n_i, \tag{6.1}$$

where $c^\dagger_{i\sigma}(c_{i\sigma})$ creates (annihilates) a fermion with spin $\sigma = \uparrow, \downarrow$ at site i, and $n_{i\sigma} = c^\dagger_{i\sigma} c_{i\sigma}$ is the number operator. It preserves the number of fermions in each spin sector, $n_\sigma = \sum_{j,\sigma} c^\dagger_{i\sigma} c_{i\sigma}$, as well as the total number of fermions, given by the sum $n_\uparrow + n_\downarrow$. In addition, it possesses particle-hole symmetry at half-filling ($\mu = U/2$). As we will be interested in the half-filled case, we can rewrite the Hamiltonian by shifting the energy by a constant,

$$H = -t \sum_{\langle i,j \rangle} \sum_{\sigma} (c^\dagger_{i,\sigma} c_{j,\sigma} + c^\dagger_{j,\sigma} c_{i,\sigma}) + U \sum_i \left(n_{i\uparrow} - \frac{1}{2} \right) \left(n_{i\downarrow} - \frac{1}{2} \right), \tag{6.2}$$

From now on, we will express all quantities in units of the hopping rate t.

The Hubbard model is exactly solvable in one dimension, where the ground state is in a Mott insulating phase for any non-zero interaction U [79]. Despite the simplicity of the model, the physics arising in dimensions higher than one remains poorly understood. Different many-body approximations have been applied to (6.1) along the years in different lattice geometries and coupling regimes. Among them, Quantum and Variational Monte Carlo calculations [80, 81, 82], Dynamical Mean-Field Theory [83], Density Matrix Renormalization Group [84] and, more recently, Density Matrix Embedding Theory [85, 86]. However, all these approaches have shown limitations to describe the strongly correlated regime ($U/t \gg 1$) in spite of the significant computational cost. In order to overcome this limitations, DMFT theories have been extended to clusters, showing excellent convergence properties in one and two dimensional lattices [87, 88]. Alternative approaches, based on slave-particle methods, have been developed in order to capture the strongly correlated regime characterized by antiferromagnetic correlations [3, 89, 90, 91], while the nature of the metal to insulator transition is still under debate.

6.2 Composite particle mean-field results

We start by tiling the original square lattice with clusters of size $L_x \times L_y$ and applying the composite particle mapping (2.39) that transforms the Hubbard Hamiltonian (6.1) into a CFB Hamiltonian of the form (2.46), where the specific form of the kinetic $\hat{T}$ and the interacting $\hat{V}$ tensors is given in the Appendix. Assuming translational invariance in the superlattice, the energy of the system can be readily computed taking the expectation value of the CFB Hamiltonian in the Fourier space (2.54),

$$\begin{aligned} E &= \sum_{\mathbf{K}} \left(T^{\alpha}_{\alpha'} \langle a^{\dagger}_{\mathbf{K}\alpha} a_{\mathbf{K}\alpha'} \rangle + T^{\beta}_{\beta'} \langle b^{\dagger}_{\mathbf{K}\beta} a_{\mathbf{K}\beta'} \rangle \right) \\ &+ \frac{1}{M} \sum_{\mathbf{K},\mathbf{Q}} \sum_{\hat{\mathbf{u}}} (V_{\hat{\mathbf{u}}})^{\beta\alpha}_{\alpha'\beta'} \left(e^{-\mathrm{i}(\mathbf{K}-\mathbf{Q})\hat{\mathbf{u}}} \langle a^{\dagger}_{\mathbf{K},\alpha} a_{\mathbf{K},\alpha'} \rangle \langle b^{\dagger}_{\mathbf{Q},\beta} b_{\mathbf{Q},\beta'} \rangle + \mathrm{H.c.} \right) \\ &+ \frac{1}{M} \sum_{\mathbf{K},\mathbf{Q}} \sum_{\hat{\mathbf{u}}} (V_{\hat{\mathbf{u}}})^{\alpha\alpha'}_{\beta\beta'} \left(e^{-\mathrm{i}(\mathbf{K}-\mathbf{Q})\hat{\mathbf{u}}} \langle a^{\dagger}_{\mathbf{K},\alpha} a^{\dagger}_{-\mathbf{K},\alpha'} \rangle \langle b_{\mathbf{Q},\beta} b_{-\mathbf{Q},\beta'} \rangle + \mathrm{H.c.} \right), \end{aligned} \quad (6.3)$$

where we have used a variational ansatz which decouples the composite bosonic and fermionic sectors as explained in Chapter 2 and restricted to real variational amplitudes for the CB and CF sectors, i.e. $(V_{\hat{\mathbf{u}}})^{\eta'\eta}_{\zeta'\zeta} = (V_{\hat{\mathbf{u}}})^{\zeta'\zeta}_{\eta'\eta}$. In particular, within the coherent approximation, the condensate CB is replaced $b^{\dagger}_{\mathbf{0g}} \to \sqrt{M}\sigma$ and the CB

fluctuations orthogonal to the CB condensed mode are neglected. The total energy reduces to,

$$\begin{aligned} E &= M T^{\mathrm{g}}_{\mathrm{g}} \sigma^2 + \sum_{\mathbf{K}} T^{\alpha}_{\alpha'} \langle a^{\dagger}_{\mathbf{K}\alpha} a_{\mathbf{K}\alpha'} \rangle \\ &+ \sigma^2 \sum_{\mathbf{K}} \sum_{\hat{\mathbf{u}}} (V_{\hat{\mathbf{u}}})^{\mathrm{g}\alpha}_{\alpha'\mathrm{g}} \left(e^{-\mathrm{i}\mathbf{K}\cdot\hat{\mathbf{u}}} \langle a^{\dagger}_{\mathbf{K}\alpha} a_{\mathbf{K}\alpha'} \rangle + \mathrm{H.c.} \right) \\ &+ \sigma^2 \sum_{\mathbf{K}} \sum_{\hat{\mathbf{u}}} (V_{\hat{\mathbf{u}}})^{\alpha\alpha'}_{\mathrm{gg}} \left(e^{-\mathrm{i}\mathbf{K}\cdot\hat{\mathbf{u}}} \langle a^{\dagger}_{\mathbf{K}\alpha} a^{\dagger}_{-\mathbf{K}\alpha'} \rangle + \mathrm{H.c.} \right). \end{aligned} \tag{6.4}$$

where repeated indices are summed. We would like to remind the reader that, although the mean-field treatment is variational and the energy reaches a minimum at self-consistency, it does not preserve the physical constraint exactly, and therefore the energy obtainedis not an upper bound of the exact ground state energy. Nevertheless, by performing a finite-size scaling analysis one can obtain a quantitative estimate of the exact result.

We are also interested in the double occupacy parameter, $D = \sum_j \langle n_{j\downarrow} n_{j\uparrow} \rangle / N$, which is directly related to the local magnetic moment $m^2 = \sum_i \langle (n_{i\uparrow} - n_{i\downarrow})^2 \rangle / N$ and therefore a change in this quantity should accompany the Mott to metal transition. It is given by

$$\begin{aligned} D &= \frac{1}{L_x L_y} \sum_{j \in \square} \sum_{\beta} \langle \beta | \, n_{j\uparrow} n_{j\downarrow} \, | \beta \rangle \, \frac{1}{M} \sum_{\mathbf{K}} \langle b^{\dagger}_{\mathbf{K}\beta} b_{\mathbf{K}\beta} \rangle \\ &+ \frac{1}{L_x L_y} \sum_{j \in \square} \sum_{\alpha} \langle \alpha | \, n_{j\uparrow} n_{j\downarrow} \, | \alpha \rangle \, \frac{1}{M} \sum_{\mathbf{K}} \langle a^{\dagger}_{\mathbf{K}\alpha} a_{\mathbf{K}\alpha} \rangle. \end{aligned} \tag{6.5}$$

where we have assumed a uniform superlattice.

In the following, we present results for the energy and the double occupancy computed with a general Slater determinant within the Bogoliubov approximation (Hartree-Fock-Bogoliubov) and the CB coherent ansatz for the bosonic sector.

In Figure 6.1, we present the energy per site (6.4) and double occupancy (6.5) for the one-dimensional case computed with various cluster sizes ($L = 2, 4, 6$). We also include the exact energy per site obtained by the Bethe ansatz (BA) [79] and the energy obtained by a standard, symmetry-preserving Hartree-Fock (HF) approximation of the original Hubbard Hamiltonian (6.1), which is exact in the non-interacting limit, $U = 0$. The ground state energy obtained with the CFB mean-field is in very good agreement with the exact result for large values of the on-site interaction U (in units of the hopping paramter t). The right inset shows how the CFB mean-field energy converges monotonically to the exact one as the size of the cluster is progressively

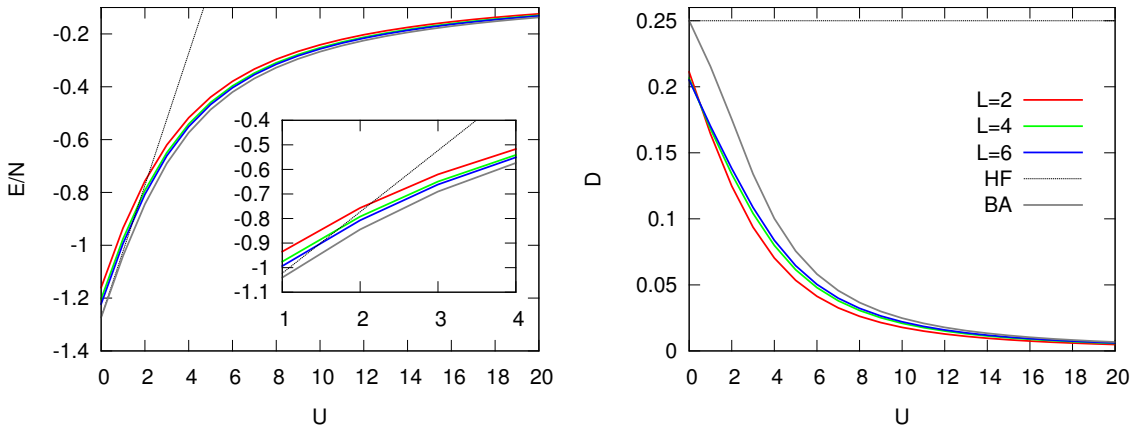

Figure 6.1: Ground state energies per site and double occupancy of the one-dimensional Hubbard model obtained from the CFB mean-field theory with various clusters sizes ($L = 2, 4, 6$), the Hartree-Fock (HF) approximation, and the exact Bethe anstaz (BA). The insets amplifies the differences in particular coupling regimes U. The dashed lines represent HF mean-field results.

increased. However, at low U, the energy from the CFB mean-field approach starts to deviate from the exact Bethe ansatz value, and crosses the HF energy at $U \sim 1.4$ for a cluster of size $L = 6$ (see left inset).

The double occupancy improves by increasing the cluster size in the range of intermediate to strong on-site interaction(see right panel inset). At weak to vanishing interactions, the CFB mean-field treatment tends to underestimate the kinetic energy contribution of the original fermions, as the on-site interaction and kinetic energy terms are not treated on equal footing, i.e. the on-site interaction is computed exactly, while part of the kinetic energy is computed in mean-field. This leads to a wave function with a lower double occupancy than the exact one. By increasing the cluster size, we are including more hopping processes into the exact computation. Nevertheless, it is interesting to see that close to the non-interacting limit $U/t = 0$, the double occupancy of the $L = 2$ cluster is higher than that obtained with an $L = 6$ cluster. This effect might be probably related to the partial breaking of translational invariance inherent to the coarse graining of the composite particle formalism.

In Figure 6.2 we show the convergence of the energy per site towards the exact Bethe ansatz result as a function of the reciprocal of the number of sites in the cluster, $1/L$, for $U = 4$ in the left panel and $U = 8$ in the right panel. Specifically, we display the energy of a single cluster obtained from the exact diagonalization of (6.1) in a cluster together with the two CFB mean-field treatments described in Chap-

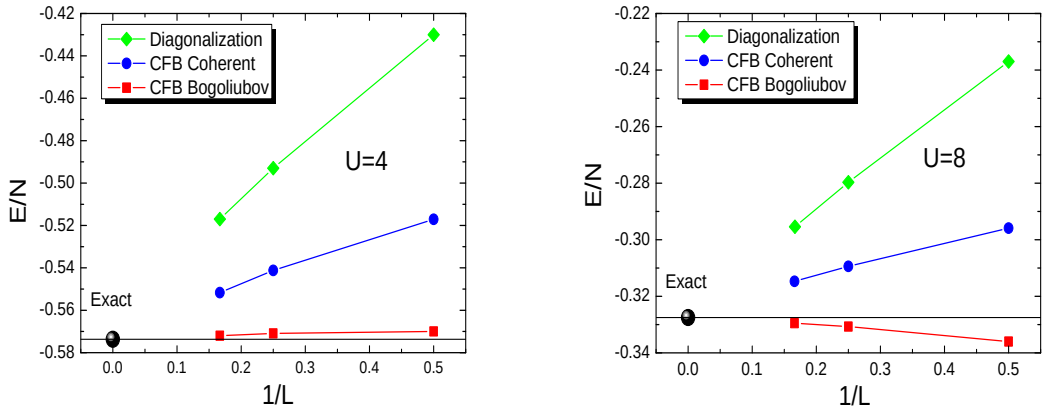

Figure 6.2: Ground state energy per site versus the inverse of the clusters size L for the CFB approximations and exact diagonalization showing the convergence to the exact Bethe ansatz value at intermediate ($U = 4$) and strong ($U = 8$) Hubbard interactions.

ter 2, namely, the bosonic coherent wave function (CFB Coherent) and the bosonic Bogoliubov wave function (CFB Bogoliubov). In both approaches (Coherent and Bogoliubov), the energy shows a clear monotonic tendence towards the exact result as a function of $1/L$. By comparing the two CFB approaches with respect to the plain diagonalization of the cluster, we can see that the use of composite particles allows for a considerable inclusion of correlation energy over the standard diagonalization. The CFB Bogoliubov treatment contains additional bosonic fluctuations over the CFB Coherent approximation which lower the energy towards the exact one. Nevertheless, for strong coupling ($U = 8$) the CFB Bogoliubov reaches an energy lower than the exact one. This is not surprising, as both ansatz contain by construction mixtures with unphysical states. It indicates that, for a fixed cluster size, the CFB Coherent ansatz is more likely to describe the strong coupling limit than the CFB Bogoliubov. In particular, the exact limit of $U \to \infty$ is contained in a CB Gutzwiller wave function (as in the case of bosonic systems), or by the closely related pure CB coherent. This can be confirmed by by inspecting the CB condensate fraction (see Fig. 6.3).

In Fig. 6.3 we show the condensate fraction computed within the CFB Coherent approach for both the one- (left) and two-dimensional (right) cases, and for several cluster sizes. In both the one- and two-dimensional cases, the condensate fraction tends to unity for any cluster size in the large U/t limit. It is remarkable that in both the one- and two-dimensional cases the smaller the cluster size is the higher the CB

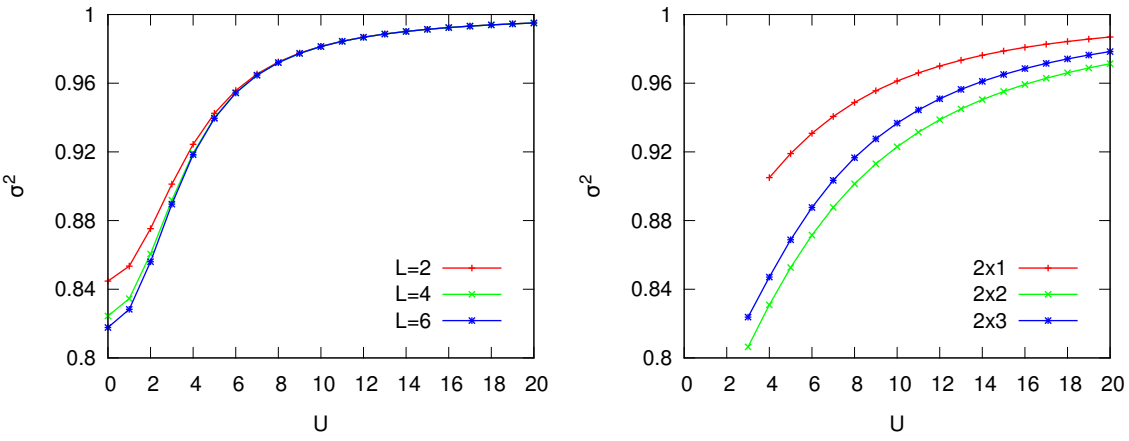

Figure 6.3: Condensate fraction of CBs computed within the CFB Coherent mean-field approximation for the one- and two-dimensional Hubbard model at half-filling for several lattice sizes. For intermediate to large on-site interactions it converges to the saturated value σ^2 assessing the validity of the CFB approach. For moderate interactions, it suddenly decreases indicating the divergence of CF fluctuations and the possible Mott to metal transition.

condensate fraction is for intermediate values of the interaction. This suggests that the CB condensate fraction should vanish at the Mott-to-metal transition.

In Figure 6.4 we show the energy and the double occupancy results of the CFB Coherent approximation for several cluster sizes applied in the two-dimensional geometry. In particular we use clusters of sizes 2×1, 2×2 and 2×3. The method is unable to reach a self-consistent solution for small U values, even with sophisticated convergence-acceleration techniques [92]. Nevertheless, the CFB can be considered as complementary to the standard HF. The energies obtained by both means are of the same order of magnitude close to the region where other methods place the phase transition. In particular, for the one-dimensional case, the HF and CFB energies cross at $U = 2.2$ ($L = 2$), $U = 1.7$ ($L = 4$) and $U = 1.4$ ($L = 6$) indicating a slow convergence towards the exact result, $U = 0$ [79]. In the two-dimensional case, recent DMFT results [93] place the Mott-insulator transition at approximately $U = 5.3$, which is slightly higher than the crossing points between HF and the CFB mean-field results.

Interestingly, the energy with 2×2 clusters is lower than the energy with 2×3, and the CB condensate fraction is lower with 2×2 than with 2×3 (see Fig. 6.3). This is originated by the fact that the 2×3 cluster is not conmensurate with the period of the Néel order, which is contained in the 2×2 cluster, on the contrary. In order to

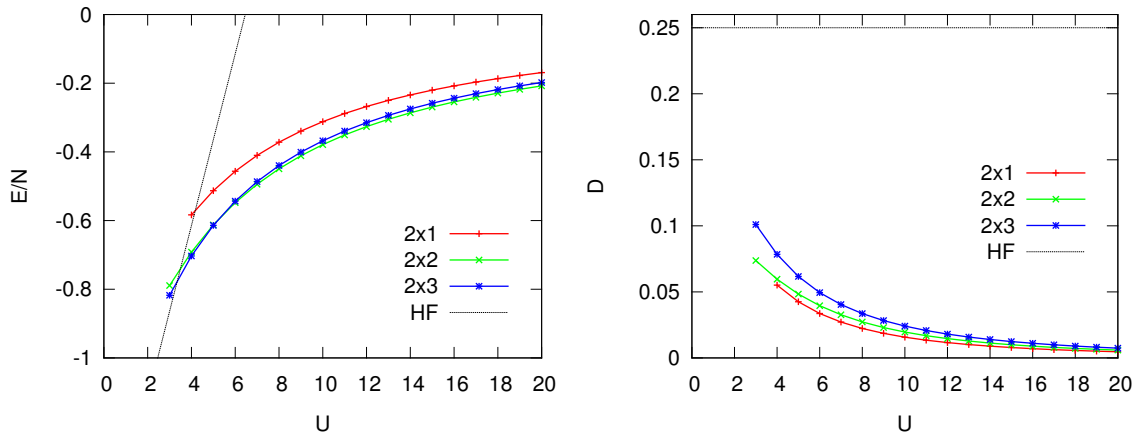

Figure 6.4: Ground state energies per site and double-occupancies of the 2-D Hubbard model obtained from the CFB mean-field theory with various clusters sizes and the Hartree-Fock approximation indicated in dashed lines.

remedy this effect, one should employ a bipartite superlattice of 2×3 clusters. This reflects the importance of choosing a cluster shape containing as many symmetries as possible of the original Hamiltonian.

6.3 Summary

In this Chapter, we have shown benchmark results of the CFB wave functions proposed in Chapter 2 for the Hubbard model at half-filling. In one- and two-dimensions, the method correctly describes the Mott insulator phase for moderate to strong interacting regimes. In particular, we have seen that the CB Coherent wave function is likely to describe the exact limit $U/t \to \infty$, as it is also the case in bosonic systems. In spite of the fact that the method is unable to describe the Fermi liquid of the weakly interacting regime, the ansatz is fairly complementary to the Hartree-Fock approach of physical fermions. The energies obtained by both means are comparable in the region where the metal to Mott transition is expected to occur, allowing for a rough estimate of it.

In order to overcome this limitation, it would be interesting to investigate the alternative CFB mapping where the cluster states with an even (odd) number of fermions are mapped to CFs (CBs) in the purely non-interacting limit.

Appendix

6.A Matrix elements of the Hubbard model

The CFB kinetic $\hat{T}$ and interaction $\hat{V}$ tensors of the Hubbard model (6.1) are

$$\begin{aligned}(T_{\mathbf{R}})^{\eta}_{\eta'} &= -t \sum_{\langle ij\rangle\in\mathbf{R}} \sum_{\sigma} {\sum_{\mathbf{n}}}' \left[U^{\eta}_{\mathbf{R}\{1_{i\sigma},0_{j\sigma}\}} U^{\eta'}_{\mathbf{R}\{0_{i\sigma},1_{j\sigma}\}} + U^{\eta}_{\mathbf{R}\{0_{i\sigma},1_{j\sigma}\}} U^{\eta'}_{\mathbf{R}\{1_{i\sigma},0_{j\sigma}\}} \right] \\ &\quad + U \sum_{j\in\mathbf{R}} \sum_{\mathbf{n}} \left(n_{j\uparrow} - \frac{1}{2} \right) \left(n_{j\downarrow} - \frac{1}{2} \right) U^{\eta}_{\mathbf{Rn}} U^{\eta}_{\mathbf{Rn}} \delta_{\eta,\eta'} \ , \qquad (6.6) \\ (V_{\mathbf{RR}'})^{\eta\eta'}_{\zeta\zeta'} &= -t \sum_{\langle i\in\mathbf{R}, j\in\mathbf{R}'\rangle} \sum_{\sigma} {\sum_{\mathbf{nn}'}}' [U^{\eta}_{\mathbf{R}\{1_{i\sigma}\}} U^{\eta'}_{\mathbf{R}'\{0_{j\sigma}\}'} U^{\zeta}_{\mathbf{R}\{0_{i\sigma}\}} U^{\zeta'}_{\mathbf{R}'\{1_{j\sigma}\}'} \\ &\quad + U^{\eta}_{\mathbf{R}\{0_{i\sigma}\}} U^{\eta'}_{\mathbf{R}'\{1_{j\sigma}\}'} U^{\zeta}_{\mathbf{R}\{1_{i\sigma}\}} U^{\zeta'}_{\mathbf{R}'\{0_{j\sigma}\}'}] \ , \qquad (6.7)\end{aligned}$$

where we have used the shorthand notation $\{n_{i\sigma}, n_{j\sigma}\} = (\ldots, n_{i\sigma}, n_{j\sigma}, \ldots)$. The prime in the sum indicates that it is restricted to cluster configurations $\mathbf{n} = (\ldots, n_{i\uparrow}, n_{i\downarrow}, n_{j\uparrow}, n_{j\downarrow} \ldots)$ with the occupation of the sites $\langle ij\rangle$ fixed. Recall that the sums are either taken over the odd (CFs) or even (CBs) subspaces. We have assumed that the ground state has no chiral order an we have taken the unitary matrix $\hat{U}$ to be real.

6.B Hartree-Bose matrix of the CFB Coherent

The Hartree matrix is obtained by deriving the energy (6.4) with respect to the bosonic amplitudes $(U^{\mathtt{g}})^{*}_{\mathbf{m}}$ (recall that we assume a homogeneus CB wave function). It will contain two terms, one comming from the one-body CB term ($\hat{h}_0$) and other comming from the interaction of the CB condensate with the CF fluctuations (contained in $\hat{h}_2$),

$$\hat{h} = \hat{h}_0 + \hat{h}_2, \qquad (6.8)$$

where

$$
\begin{aligned}
(h_0)_{\mathbf{n},\mathbf{m}} &= -t \sum_{\langle ij\rangle \in \square} \sum_{\sigma} \left[\delta_{\mathbf{n},\{1_{i\sigma},0_{j\sigma}\}} \delta_{\mathbf{m},\{0_{i\sigma},1_{j\sigma}\}} + \delta_{\mathbf{n},\{0_{i\sigma},1_{j\sigma}\}} \delta_{\mathbf{m},\{1_{i\sigma},0_{j\sigma}\}} \right] \\
&\quad + U \sum_{j \in \square} \left[n_{j\uparrow} n_{j\downarrow} - \frac{1}{2}(n_{j\uparrow} + n_{j\downarrow}) \right] \delta_{\mathbf{n},\mathbf{m}} \qquad (6.9)
\end{aligned}
$$

where $\mathbf{n}, \mathbf{m}$ are both CB configurations, with an even number of fermions in the cluster.

The contribution of the CF fluctuations to the Hartree matrix is

$$
\begin{aligned}
(h_2)_{\mathbf{n},\mathbf{m}} &= -t \sum_{\langle ij\rangle}{}' \sum_{\sigma} \sum_{\alpha\alpha'} \left(U^{\alpha}_{\{0_{j\sigma}\}} U^{\alpha'}_{\{0_{i\sigma}\}} \delta_{\mathbf{n},\{1_{i\sigma}\}} \delta_{\mathbf{m},\{1_{j\sigma}\}} + U^{\alpha}_{\{1_{j\sigma}\}} U^{\alpha'}_{\{1_{i\sigma}\}} \delta_{\mathbf{n},\{0_{i\sigma}\}} \delta_{\mathbf{m},\{0_{j\sigma}\}} \right) \\
&\qquad \times \sum_{\hat{\mathbf{u}}} \sum_{\mathbf{K}} \left(e^{-\mathrm{i}\mathbf{K}\hat{\mathbf{u}}} \langle a^{\dagger}_{\mathbf{K}\alpha} a_{\mathbf{K}\alpha'} \rangle + \mathrm{H.c.} \right) \\
&\quad -t \sum_{\langle ij\rangle}{}' \sum_{\sigma} \sum_{\alpha\alpha'} \left(U^{\alpha}_{\{0_{j\sigma}\}} U^{\alpha'}_{\{1_{i\sigma}\}} \delta_{\mathbf{n},\{1_{i\sigma}\}} \delta_{\mathbf{m},\{0_{j\sigma}\}} + U^{\alpha}_{\{1_{j\sigma}\}} U^{\alpha'}_{\{0_{i\sigma}\}} \delta_{\mathbf{n},\{0_{i\sigma}\}} \delta_{\mathbf{m},\{1_{j\sigma}\}} \right) \\
&\qquad \times \sum_{\hat{\mathbf{u}}} \sum_{\mathbf{K}} \left(e^{-\mathrm{i}\mathbf{K}\hat{\mathbf{u}}} \langle a^{\dagger}_{\mathbf{K}\alpha} a^{\dagger}_{\mathbf{K}\alpha'} \rangle + \mathrm{H.c.} \right), \qquad (6.10)
\end{aligned}
$$

where the prime indicates that the sum is restricted to the bonds of the original lattice connecting two neighbouring clusters.

Chapter 7

Summary and conclusions

In this thesis we have presented a method to describe short range correlated phases characterized by various long range orders of strongly correlated bosonic and fermionic systems relevant for condensed matter and cold atom physics. Specifically, it has been shown to be very well suited to treat frustrated spin and bosonic systems, and fermionic Mott insulators in two dimensional lattices, offering a good alternative to describe those systems which pose significant problems and computational expenses to other state-of-the-art methodologies.

Building upon the HMFT framework for quantum magnetism, the method is based on the identification of clusters as the basic building blocks containing the necessary correlations to describe the relevant physics of the phases present in the system under study. We start by tiling of the real-space lattice into clusters. The shape and size of the clusters is chosen so as to preserve as much as possible the original symmetries of the Hamiltonian. The many-body quantum states of the clusters are represented by the action of a new set of *composite boson* (CB) or *composite fermion* (CF) operators, depending on the statistics of the original problem. As the new composite operator Fock space is enlarged with respect to the original one, the physical subspace will be defined by all the states having one-and-only-one composite particle per superlattice site. This restriction is referred to as *physical constraint*. The mapping that relates the original set of spins, bosons or fermion operators with the new set of composite particle operators can be considered as a cluster extension of the Schwinger, Dickerscheid [11] or Zou-Anderson [12] mappings, respectively. Being the mapping canonical, it is possible to reexpress the model Hamiltonian of interest in terms of the new composite operators acting on the coarse grained superlattice and treat it by standard many-body techniques, with the advantage that the short range correlations are treated exactly by definition. Specifically, spin and bosonic Hamiltonians are mapped to CB

Hamiltonians while fermionic Hamiltonians are mapped to composite fermion-boson (CFB) Hamiltonians on the superlattice.

We have proposed various composite particle mean-field schemes to treat general composite particle Hamiltonians. We have introduced a CB Gutzwiller ansatz consisting of an uncorrelated product of clusters. This ansatz has allowed us to map the phase diagram of the J-K model obtaining novel superfluid and solid phases characterized by the presence of chirality in the frustrated region where QMC computations cannot be carried out. In addition, the phases obtained within the non-frustrated region are in qualitative agreement with previous QMC results. This ansatz has permited us to study a system of strongly correlated bosons in the presence of artificial gauge fields, obtaining fractional Mott insulators, chiral superfluid and a supersolid phase for a wide region of the phase diagram. This system can be realized with current cold atom experimental techniques, opening the possibility of probing the long-sought supersolid phase.

Taking clusters of the original degrees of freedom as the basic building blocks, we are treating different quantum orders on equal footing, and we are able to map the phase diagram with a unique wave function, describing phases which are not accessible by standard mean-field techniques. The CB Gutzwiller wave function allows for the systematic computation of observables and order paramters. In particular, as it preserves exactly the physical constraint, the energy is an upper bound to the exact one, and borders and order of phase transitions can be obtained by computing the energy derivatives with respect to the control parameters of the Hamiltonian. By performing several coarse-grainings we can assess the stability of the phases.

We have shown that we can include quantum fluctuations over the previous CB Gutzwiller wave function by using a CB Coherent-Bogoliubov ansatz. This wave function allows for the computation of the low-lying excitations over the ground state in a self-consistent manner. We have seen that this wave function allows us to compute the linear spin wave dispersions of ferromagnets when applied to problems of quantum magnetism through its application to the chiral superfluid phase of the J-K model. We have done benchmark calculations on the Bose-Hubbard model in two dimensions obtaining a phase diagram in quantitative agreement with QMC results, being competitive with other more sophisticated techniques such as VCA. We have shown how the progressive inclusion of quantum fluctuations over the CB condensate self-consistently leads to a quantitative improvement of the critical point. Moreover, we have obtained the low-lying dispersions over the ground state self-consistently. In particular, the Higgs excitation mode of the superfluid and the particle-hole excitation

of the Mott insulator were in quantitative agreement with recent cold atom experiments. Although this wave function does not satisfy exactly the physical constraint, and therefore it is not Ritz variational, the method provides also with an estimator of the degree of validity of the approximation, i.e. the CB condensate fraction.

We have proposed a self-consistent mean-field scheme to treat the CFB Hamiltonian resulting from the CFB mapping of Hubbard-type Hamiltonians. The scheme is based on a trial wave function which decouples the CB and CF sectors. The CF sector is always treated as a Bogoliubov vacuum of CF quasi-particles while the CB sector can be approximated by means of a CB Coherent ansatz or by means of a CB Bogoliubov ansatz. We have applied the method to the Hubbard model at half-filling, obtaining a good description of the Mott phase in both one- and two-dimensions. In particular, the CB Coherent wave function for the CB sector is able to capture the exact infinite interaction limit. The CFB mean-field scheme can be considered complementary to the standard Hartree-Fock solution to the metallic phase, and gives rough estimations of the metal-to-Mott transition. Further investigation on alternative mean-field schemes is required in order to overcome this limitation.

The mean-field schemes presented here are unable to describe strongly correlated phases of matter when the characteristic correlation length exceeds the dimensions of the cluster, i.e. critical phases characterized by power law correlations or phases characterized by non-local order parameters which lead to the so-called *spin liquid* phases. Further investigation is needed in order to overcome this limitation. One possibility would be to use alternative ansatze of the type CB Bogoliubov and including the emergent $U(1)$ lattice gauge potential term intrinsic to the mapping, similarly as it is done in other slave-particle approaches.

By setting a general composite particle algebraic framework we are leaving open the possibility to further extensions and uses as, for example, a time-dependent extension to study quench-dynamics in cold-atom systems.

Conclusiones

En esta tesis hemos presentado un método para describir fases con correlaciones de corto alcance que aparecen en sistemas bosónicos y fermiónicos fuertemente correlacionados que son relevantes para física de la materia condensada y átomos fríos. Se ha mostrado que es particularmente conveniente para tratar sistemas frustrados de espín y bosónicos, y aislantes de Mott fermiónicos en redes de dos dimensiones y por tanto resulta ser una buena alternativa para tratar sistemas que plantean serios problemas y alto costos computacionales a otros métodos del estado del arte.

Extendiendo el esquema algebraico de HMFT para magnetismo cuántico, el método está basado en la identificación de clusters como las piezas fundamentales que contienen las correlaciones necesarias para describir la física relevante de las fases presentes en el sistema de estudio. Se comienza realizando un perfecto teselado de la red en el espacio real con *clusters* o conjuntos de los grados de libertad de la red original. La forma y tamaño del cluster es elegida de manera que preserve en la mayor medida posible las simetrias originales del Hamiltoniano a tratar. Los estados cuánticos de muchos cuerpos del cluster son representados por la acción de un nuevo conjunto the *bosones compuestos* (CB) o *fermiones compuestos* (CF), dependiendo de la estadística original del problema. Como el espacio de Fock de los nuevos operadores compuestos es mayor que el espacio de Fock del problema original, el subespacio físico estará definido por aquellos estados que tengan una única partícula compuesta en cada uno de los sitios de la super-red. Está restricción es referida como *restricción física*. La relación del conjunto original de operadores de espín, bosónicos y fermiónicos con el nuevo conjunto de operadores de partículas compuestas queda establecida a través de un mapping canónico que se puede considerar la extensión a clusters del mapping de Schwinger, Dickerscheid [11] o el de Zou-Anderson [12], respectivamente. Al ser el mapping canónico, es posible reescribir el Hamiltoniano objeto de estudio en términos de los nuevos operadores compuestos actuando en la super-red y tratarlo mediante técnicas estándar de muchos cuerpos, con la ventaja de que las correlaciones de corto alcance están tenidas en cuenta de manera exacta en la propia definición de las

partículas compuestas. En particular, Hamiltonianos de espín y bosónicos se mapean a Hamiltonianos de bosones compuestos mientras que Hamiltonianos fermiónicos se mapean a Hamiltonianos de bosones y fermiones compuestos en la super-red.

Hemos propuesto varios esquemas de campo medio de partículas compuestas para tratar Hamiltonianos generales de particulas compuestas. Hemos introducido un ansatz CB Gutzwiller que consiste en un producto de clusters no correlacionados. Este ansatz nos ha permitido desvelar el diagrama de fases del modelo J-K obteniendo nuevas fases superfluidas y sólidas caracterizadas por la presencia de orden quiral en la region frustrada, donde QMC no es aplicable. Además, las fases obtenidas en la region no frustrada están en acuerdo cualitativo con resultados anteriores de QMC. Este ansatz nos a permitido también estudiar un sistema de bosones fuertemente correlacionado en presencia de campos de gauge artificiales, obteniendo aislantes de Mott de densidad fraccionaria, superfluidos quirales y una fase supersólida para una amplia región del diagrama de fase. Este sistema puede ser realizado experimentalmente con las técnicas de átomos fríos disponibles actualmente, abriendo la posibilidad de obtener en el laboratorio la fase supersólida, aún no hallada experimentalmente.

Tomando *clusters* de los grados de libertad originales como las piezas fundamentales, estamos tratando diferentes órdenes cuánticos por igual lo que nos permite obtener el diagrama de fases con una única función de onda y describir fases que no son accesibles a métodos de campo medio estándar. La funcion de onda CB Gutzwiller permite la computación sistemática de observables y parámetros de orden. En particular, como preserva exactamente la restricción física, la energía que se obtiene es un límite superior a la energía exacta, y las fronteras entre las fases y los órdenes de las transiciones de fase se pueden obtener mediante la computación de derivadas de la energía con respecto a los parámetros de control del Hamiltoniano. Realizando diferentes teselados de la red original podemos evaluar la estabilidad de las fases.

Hemos mostrado que podemos incluir fluctuaciones cuánticas sobre el ansatz CB Gutzwiller utilizando un ansatz CB Coherente-Bogoliubov, que está estrechamente relacionado. Este ansatz permite la computación de las excitaciones de baja energía sobre el estado fundamental de manera auto-consistente. En el límite en que los CBs son bosones de Schwinger asociados a grados de libertad de espín, hemos visto que esta función de onda nos permite computar las dispersiones de las ondas de espín lineales de los ferromagnetos en el caso de ser aplicada a problemas de magnetismo cuántico a través de su aplicación al superfluido quiral que emerge en el modelo J-K. Hemos hecho benchmark sobre el modelo de Bose-Hubbard en dos dimensiones obteniendo un diagrama de fases en acuerdo cuantitativo con resultados de QMC previos, y siendo

competitivos con los resultados de otras técnicas aproximativas sofisticadas, como el método VCA. Hemos mostrado que la inclusión progresiva de fluctuaciones cuánticas sobre el condensado de CBs de manera auto-consistente lleva a una mejor cuantitativa en el posicionado del punto crítico. Además, hemos obtenido las dispersiones sobre el estado fundamental de maner auto-consistente. En particular, los modos de excitación Higgs y Goldstone del superfluido están en acuerdo cuantitativo con experimentos recientes de átomos fríos. Aunque esta función de onda no preserva la restricción física de manera exacta, y por lo tanto la energía no es un límite superior a la exacta, el método provee un indicador que estima el grado de validez de la aproximación, esto es, la densidad del condensado de CBs.

Hemos propuesto un esquema de campo medio auto-consistente para tratar Hamiltonianos de bosones y fermiones compuestos (CFB) que resultan del mapping CFB de Hamiltonianos fermiónicos tipo Hubbard. El esquema está basado en un ansatz que desacopla los sectores bosónicos y fermiónicos. El sector CF es siempre tratado mediante un vacío de Bogoliubov de quasi-partículas CF mientras que el sector CB puede ser aproximado mediante un ansatz tipo CB Coherente o un ansatz CB Bogoliubov. Hemos aplicado el método al modelo de Hubbard con llenado medio obteniendo una buena descripción del aislante de Mott tanto en una como en dos dimensiones. En particular, el ansatz CB Coherent para el sector CB es capaz de capturar el límite exacto de interacción infinita. El esquema campo medio CFB propuesto puede ser considerado complementario al método Hartree-Fock estándar para el metal, y dar una estimación de la transición Mott-metal. Es necesario investigación adicional sobre ansatz CFB alternativos que puedan solventar esta limitación del método.

Los esquemas de campo medio presentados en esta tesis no son capaces de describir fases cuyas longitudes de correlación características exceden las dimensiones de los clusters, como por ejemplo fases críticas caracterizadas por correlaciones que decaen como leyes de potencia o fases caracterizadas por parámetros de orden no locales. Esta limitación puede quizá ser solventada mediante el uso de diferentes funciones de onda CB Bogoliubov e incluyendo el campo gauge $U(1)$ que emerge en la red de manera intrínseca al mapping.

Al establecer un esquema algebraico general de partículas compuestas dejamos la posibilidad abierta para diferentes aplicaciones y extensiones del método, como por ejemplo, la extensión dependiente del tiempo para tratar dinámica de *quenches* en sistemas de átomos fríos.

Bibliography

[1] P. A. Lee, N. Nagaosa, and X.-G. Wen, "Doping a Mott insulator: Physics of high-temperature superconductivity," *Rev. Mod. Phys.*, vol. 78, pp. 17–85, 2006.

[2] G. R. Stewart, "Superconductivity in iron compounds," *Rev. Mod. Phys.*, vol. 83, pp. 1589–1652, Dec 2011.

[3] P. Coleman, "New approach to the mixed-valence problem," *Phys. Rev. B*, vol. 29, pp. 3035–3044, Mar 1984.

[4] A. Auerbach, *Interacting electrons and quantum magnetism.* New York: Springer-Verlag, 1994.

[5] J. Rau, E.-H. Lee, and H.-Y. Kee, "Generic spin model for the honeycomb iridates beyond the Kitaev limit," *Phys. Rev. Lett.*, vol. 112, p. 077204, Feb 2014.

[6] Y. Kamihara, T. Watanabe, M. Hirano, and H. Hosono, "Iron-based layered superconductor La[$O_{1-x}F_x$]FeAs ($x = 0.050.12$) with T_c= $26K$," *Journal of the American Chemical Society*, vol. 130, no. 11, pp. 3296–3297, 2008.

[7] M. Shores, E. Nytko, B. Bartlett, and D. Nocera, "A structurally perfect S=1/2 Kagomé antiferromagnet," *Journal of the American Chemical Society*, vol. 127, no. 39, pp. 13462–13463, 2005. PMID: 16190686.

[8] H.T.Diep, ed., *Frustrated spin systems.* London: World Scientific, 2004.

[9] M. Lewenstein, A. Sanpera, V. Ahufinger, B. Damski, A. Sen(De), and U. Sen, "Ultracold atomic gases in optical lattices: mimicking condensed matter physics and beyond," *Adv. Phys.*, vol. 56:2, pp. 243–379.

[10] C. D. Batista and G. Ortiz, "Algebraic approach to interacting quantum systems," *Advances in Physics*, vol. 53, no. 1, pp. 1–82, 2004.

[11] D. B. M. Dickerscheid, D. van Oosten, P. J. H. Denteneer, and H. T. C. Stoof, "Ultracold atoms in optical lattices," *Phys. Rev. A*, vol. 68, p. 043623, Oct 2003.

[12] Z. Zou and P. W. Anderson, "Neutral fermion, charge-e boson excitations in the resonating-valence-bond state and superconductivity in La_2CuO_4-based compounds," *Phys. Rev. B*, vol. 37, pp. 627–630, Jan 1988.

[13] D. Huerga, J. Dukelsky, and G. E. Scuseria, "Composite boson mapping for lattice boson systems," *Phys. Rev. Lett.*, vol. 111, p. 045701, Jul 2013.

[14] J. Zhao, C. Jimenez-Hoyos, G. Scuseria, D. Huerga, J. Dukelsky, S. Rombouts, and G. Ortiz, "Composite fermion-boson mapping for fermionic lattice models," *arXiv*, p. 1408.1014.

[15] D. Huerga, J. Dukelsky, N. Laflorencie, and G. Ortiz, "Chiral phases of two-dimensional hard-core bosons with frustrated ring exchange," *Phys. Rev. B*, vol. 89, p. 094401, Mar 2014.

[16] Z. Nussinov and G. Ortiz, "Bond algebras and exact solvability of Hamiltonians: Spin $s = \frac{1}{2}$ multilayer systems," *Phys. Rev. B*, vol. 79, p. 214440, Jun 2009.

[17] E. Cobanera, G. Ortiz, and Z. Nussinov, "Unified approach to quantum and classical dualities," *Phys. Rev. Lett.*, vol. 104, p. 020402, Jan 2010.

[18] E. Cobanera, G. Ortiz, and Z. Nussinov, "The bond-algebraic approach to dualities," *Advances in Physics*, vol. 60, no. 5, pp. 679–798, 2011.

[19] L. Isaev, G. Ortiz, and J. Dukelsky, "Hierarchical mean-field approach to the J_1-J_2 Heisenberg model on a square lattice," *Phys. Rev. B*, vol. 79, p. 024409, Jan 2009.

[20] L. Isaev, G. Ortiz, and J. Dukelsky, "Phase diagram of the Heisenberg antiferromagnet with four-spin interactions," *J. Phys.: Condens. Matter*, vol. 22, p. 016006, 2010.

[21] L. Isaev, G. Ortiz, and J. Dukelsky, "Local physics of magnetization plateaux in the Shastry-Sutherland model," *Phys. Rev. Lett.*, vol. 103, p. 177201, Oct 2009.

[22] E. Zhao and A. Paramekanti, "Self-consistent slave rotor mean-field theory for strongly correlated systems," *Phys. Rev. B*, vol. 76, p. 195101, Nov 2007.

[23] D. Yamamoto, A. Masaki, and I. Danshita, "Quantum phases of hardcore bosons with long-range interactions on a square lattice," *Phys. Rev. B*, vol. 86, p. 054516, Aug 2012.

[24] A. E. Trumper, L. O. Manuel, C. J. Gazza, and H. A. Ceccatto, "Schwinger-boson approach to quantum spin systems: Gaussian fluctuations in the "natural" gauge," *Phys. Rev. Lett.*, vol. 78, pp. 2216–2219, Mar 1997.

[25] G. Kotliar and A. E. Ruckenstein, "New functional integral approach to strongly correlated fermi systems: The Gutzwiller approximation as a saddle point," *Phys. Rev. Lett.*, vol. 57, pp. 1362–1365, Sep 1986.

[26] J.-P. Blaizot and G. Ripka, *Quantum theory of finite systems*. Cambridge: MIT Press, 1986.

[27] M. Roger, J. H. Hetherington, and J. M. Delrieu, "Magnetism in solid ^{3}He," *Rev. Mod. Phys.*, vol. 55, pp. 1–64, Jan 1983.

[28] M. Roger, "Ring exchange and correlated fermions," *Journal of Physics and Chemistry of Solids*, vol. 66, no. 89, pp. 1412 – 1416, 2005.

[29] R. Coldea, S. M. Hayden, G. Aeppli, T. G. Perring, C. D. Frost, T. E. Mason, S.-W. Cheong, and Z. Fisk, "Spin waves and electronic interactions in La_2CuO_4," *Phys. Rev. Lett.*, vol. 86, pp. 5377–5380, Jun 2001.

[30] A. W. Sandvik, S. Daul, R. R. P. Singh, and D. J. Scalapino, "Striped phase in a quantum XY model with ring exchange," *Phys. Rev. Lett.*, vol. 89, p. 247201, Nov 2002.

[31] R. G. Melko, A. W. Sandvik, and D. J. Scalapino, "Two-dimensional quantum XY model with ring exchange and external field," *Phys. Rev. B*, vol. 69, p. 100408, Mar 2004.

[32] T. Matsubara and H. Matsuda, "A lattice model of liquid Helium," *Progress of Theoretical Physics*, vol. 16, no. 6, pp. 569–582, 1956.

[33] A. W. Sandvik, "Evidence for deconfined quantum criticality in a two-dimensional Heisenberg model with four-spin interactions," *Phys. Rev. Lett.*, vol. 98, p. 227202, Jun 2007.

[34] A. Läuchli, J. C. Domenge, C. Lhuillier, P. Sindzingre, and M. Troyer, "Two-step restoration of SU(2) symmetry in a frustrated ring-exchange magnet," *Phys. Rev. Lett.*, vol. 95, p. 137206, Sep 2005.

[35] Z. Nussinov and G. Ortiz, "A symmetry principle for topological quantum order," *Annals of Physics*, vol. 324, no. 5, pp. 977 – 1057, 2009.

[36] A. Paramekanti, L. Balents, and M. P. A. Fisher, "Ring exchange, the exciton Bose liquid, and bosonization in two dimensions," *Phys. Rev. B*, vol. 66, p. 054526, Aug 2002.

[37] R. Schaffer, A. A. Burkov, and R. G. Melko, "Superfluid phases of lattice bosons with ring-exchange interaction," *Phys. Rev. B*, vol. 80, p. 014503, Jul 2009.

[38] K. A. Al-Hassanieh, C. D. Batista, G. Ortiz, and L. N. Bulaevskii, "Field-induced orbital antiferromagnetism in Mott insulators," *Phys. Rev. Lett.*, vol. 103, p. 216402, Nov 2009.

[39] M. P. Zaletel, S. A. Parameswaran, A. Rüegg, and E. Altman, "Chiral bosonic Mott insulator on the frustrated triangular lattice," *Phys. Rev. B*, vol. 89, p. 155142, Apr 2014.

[40] J. J. Sakurai and J. Napolitano, *Modern quantum mechanics*. San Francisco: Addison-Wesley, 2011.

[41] Nozières, P. and Saint James, D., "Particle vs. pair condensation in attractive Bose liquids," *J. Phys. France*, vol. 43, no. 7, pp. 1133–1148, 1982.

[42] T. Tay and O. I. Motrunich, "Possible realization of the exciton Bose liquid phase in a hard-core boson model with ring-only exchange interactions," *Phys. Rev. B*, vol. 83, p. 205107, May 2011.

[43] R. V. Mishmash, M. S. Block, R. K. Kaul, D. N. Sheng, O. I. Motrunich, and M. P. A. Fisher, "Bose metals and insulators on multileg ladders with ring exchange," *Phys. Rev. B*, vol. 84, p. 245127, Dec 2011.

[44] A. Sandvik and R. Melko, "Ground-state phases and quantum phase transitions in a two-dimensional spin-1/2 XY model with four-spin interactions," *Annals of Physics*, vol. 321, no. 7, pp. 1651 – 1668, 2006. July 2006 Special Issue.

[45] T. Coletta, N. Laflorencie, and F. Mila, "Semiclassical approach to ground-state properties of hard-core bosons in two dimensions," *Phys. Rev. B*, vol. 85, p. 104421, Mar 2012.

[46] D. Jaksch, C. Bruder, J. I. Cirac, C. W. Gardiner, and P. Zoller, "Cold bosonic atoms in optical lattices," *Phys. Rev. Lett.*, vol. 81, pp. 3108–3111, Oct 1998.

[47] M. P. A. Fisher, P. B. Weichman, G. Grinstein, and D. S. Fisher, "Boson localization and the superfluid-insulator transition," *Phys. Rev. B*, vol. 40, pp. 546–570, Jul 1989.

[48] D. van Oosten, P. van der Straten, and H. T. C. Stoof, "Quantum phases in an optical lattice," *Phys. Rev. A*, vol. 63, p. 053601, Apr 2001.

[49] S. Sachdev, *Quantum phase transitions*. Cambridge, UK: Cambridge University Press, 1999.

[50] S. D. Huber, E. Altman, H. P. Büchler, and G. Blatter, "Dynamical properties of ultracold bosons in an optical lattice," *Phys. Rev. B*, vol. 75, p. 085106, Feb 2007.

[51] D. Pekker and C. Varma, "Amplitude/Higgs modes in condensed matter physics," *arXiv*, p. 1406.2968.

[52] L. Amico and V. Penna, "Dynamical mean field theory of the Bose-Hubbard model," *Phys. Rev. Lett.*, vol. 80, pp. 2189–2192, Mar 1998.

[53] D. Pekker, B. Wunsch, T. Kitagawa, E. Manousakis, A. S. Sørensen, and E. Demler, "Signatures of the superfluid to Mott insulator transition in equilibrium and in dynamical ramps," *Phys. Rev. B*, vol. 86, p. 144527, Oct 2012.

[54] T. McIntosh, P. Pisarski, R. J. Gooding, and E. Zaremba, "Multisite mean-field theory for cold bosonic atoms in optical lattices," *Phys. Rev. A*, vol. 86, p. 013623, Jul 2012.

[55] M. Knap, E. Arrigoni, and W. von der Linden, "Variational cluster approach for strongly correlated lattice bosons in the superfluid phase," *Phys. Rev. B*, vol. 83, p. 134507, Apr 2011.

[56] E. Arrigoni, M. Knap, and W. von der Linden, "Extended self-energy functional approach for strongly correlated lattice bosons in the superfluid phase," *Phys. Rev. B*, vol. 84, p. 014535, Jul 2011.

[57] B. Capogrosso-Sansone, S. G. Söyler, N. Prokof'ev, and B. Svistunov, "Monte Carlo study of the two-dimensional Bose-Hubbard model," *Phys. Rev. A*, vol. 77, p. 015602, Jan 2008.

[58] S. Gazit, D. Podolsky, and A. Auerbach, "Fate of the Higgs mode near quantum criticality," *Phys. Rev. Lett.*, vol. 110, p. 140401, Apr 2013.

[59] L. Pollet and N. Prokof'ev, "Higgs mode in a two-dimensional superfluid," *Phys. Rev. Lett.*, vol. 109, p. 010401, Jul 2012.

[60] K. Chen, L. Liu, Y. Deng, L. Pollet, and N. Prokof'ev, "Universal properties of the Higgs resonance in (2+1)-Dimensional $U(1)$ critical systems," *Phys. Rev. Lett.*, vol. 110, p. 170403, Apr 2013.

[61] M. Greiner, O. Mandel, T. Esslinger, T. Hänsch, and I. Bloch, "Quantum phase transition from a superfluid to a Mott insulator in a gas of ultracold atoms," *Nature*, vol. 415, p. 39, 2002.

[62] M. Endres, T. Fukuhara, D. Pekker, M. Cheneau, P. Schauss, C. Gross, E. Demler, S. Kuhr, and I. Bloch, "The Higgs amplitude mode at the two-dimensional superfluid/Mott insulator transition," *Nature*, vol. 455, p. 455, 2012.

[63] V. I. Yukalov, "Basics of Bose-Einstein condensation," *Phys. Part. Nucl.*, vol. 42, p. 460, 2011.

[64] M. Aidelsburger, M. Atala, M. Lohse, J. T. Barreiro, B. Paredes, and I. Bloch, "Realization of the Hofstadter Hamiltonian with ultracold atoms in optical lattices," *Phys. Rev. Lett.*, vol. 111, p. 185301, Oct 2013.

[65] H. Miyake, G. A. Siviloglou, C. J. Kennedy, W. C. Burton, and W. Ketterle, "Realizing the Harper Hamiltonian with laser-assisted tunneling in optical lattices," *Phys. Rev. Lett.*, vol. 111, p. 185302, Oct 2013.

[66] J. Struck, C. Ölschläger, M. Weinberg, P. Hauke, J. Simonet, A. Eckardt, M. Lewenstein, K. Sengstock, and P. Windpassinger, "Tunable gauge potential for neutral and spinless particles in driven optical lattices," *Phys. Rev. Lett.*, vol. 108, p. 225304, May 2012.

[67] M. Aidelsburger, M. Atala, S. Nascimbène, S. Trotzky, Y.-A. Chen, and I. Bloch, "Experimental realization of strong effective magnetic fields in an optical lattice," *Phys. Rev. Lett.*, vol. 107, p. 255301, Dec 2011.

[68] D. Jaksh and P. Zoller, "Creation of effective magnetic fields in optical lattices: the Hofstadter butterfly for cold neutral atoms," *New J. Phys.*, vol. 5, p. 56, 2003.

[69] M. Atala, M. Aidelsburger, M. Lohse, J. Barreiro, B. Paredes, and I. Bloch, "Observation of the Meissner effect with ultracold atoms in bosonic ladders," *arXiv:1402.0819*, 2014.

[70] A. Dhar, T. Mishra, M. Maji, R. V. Pai, S. Mukerjee, and A. Paramekanti, "Chiral Mott insulator with staggered loop currents in the fully frustrated Bose-Hubbard model," *Phys. Rev. B*, vol. 87, p. 174501, May 2013.

[71] A. Petrescu and K. Le Hur, "Bosonic Mott insulator with Meissner currents," *Phys. Rev. Lett.*, vol. 111, p. 150601, Oct 2013.

[72] A. Rapp, X. Deng, and L. Santos, "Ultracold lattice gases with periodically modulated interactions," *Phys. Rev. Lett.*, vol. 109, p. 203005, Nov 2012.

[73] S. Greschner, G. Sun, D. Poletti, and L. Santos, "Density dependent synthetic gauge fields using periodically modulated interactions," *arXiv:1311.3150*, 2014.

[74] T. Keilmann, S. Lanzmich, I. McCulloch, and M. Roncaglia, "Statistically induced phase transitions and anyons in 1D optical lattices," *Nature Commun.*, vol. 2, p. 361, 2011.

[75] E. Orignac and T. Giamarchi, "Meissner effect in a bosonic ladder," *Phys. Rev. B*, vol. 64, p. 144515, Sep 2001.

[76] A. Tokuno and A. Georges, "Ground states of a Bose–Hubbard ladder in an artificial magnetic field: field-theoretical approach," *New J. Phys.*, vol. 16, p. 073005.

[77] F. Crépin, N. Laflorencie, G. Roux, and P. Simon, "Phase diagram of hard-core bosons on clean and disordered two-leg ladders: Mott insulator–Luttinger liquid–Bose glass," *Phys. Rev. B*, vol. 84, p. 054517, Aug 2011.

[78] T. Ying, G. G. Batrouni, G. X. Tang, X. D. Sun, and R. T. Scalettar, "Charge gaps at fractional fillings in boson Hubbard ladders," *Phys. Rev. B*, vol. 89, p. 195128, May 2014.

[79] E. H. Lieb and F. Y. Wu, "Absence of Mott transition in an exact solution of the short-range, one-band model in one dimension," *Phys. Rev. Lett.*, vol. 20, pp. 1445–1448, 1968.

[80] S. Zhang, J. Carlson, and J. E. Gubernatis, "Pairing correlations in the two-dimensional Hubbard model," *Phys. Rev. Lett.*, vol. 78, pp. 4486–4489, 1997.

[81] M. Guerrero, G. Ortiz, and J. E. Gubernatis, "Correlated wave functions and the absence of long-range order in numerical studies of the Hubbard model," *Phys. Rev. B*, vol. 59, pp. 1706–1711, Jan 1999.

[82] S. Sorella, "Wave function optimization in the variational Monte Carlo method," *Phys. Rev. B*, vol. 71, p. 241103, 2005.

[83] A. Georges, G. Kotliar, W. Krauth, and M. J. Rozenberg, "Dynamical mean-field theory of strongly correlated fermion systems and the limit of infinite dimensions," *Rev. Mod. Phys.*, vol. 68, pp. 13–125, 1996.

[84] U. Schollwöck, "The density-matrix renormalization group," *Rev. Mod. Phys.*, vol. 77, pp. 259–315, 2005.

[85] G. Knizia and G. K.-L. Chan, "Density matrix embedding: A simple alternative to dynamical mean-field theory," *Phys. Rev. Lett.*, vol. 109, p. 186404, 2012.

[86] I. W. Bulik, G. E. Scuseria, and J. Dukelsky, "Density matrix embedding from broken symmetry lattice mean fields," *Phys. Rev. B*, vol. 89, p. 035140, Jan 2014.

[87] G. Kotliar, S. Y. Savrasov, G. Pálsson, and G. Biroli, "Cellular dynamical mean field approach to strongly correlated systems," *Phys. Rev. Lett.*, vol. 87, p. 186401, 2001.

[88] M. Balzer, W. Hanke, and M. Potthoff, "Mott transition in one dimension: Benchmarking dynamical cluster approaches," *Phys. Rev. B*, vol. 77, p. 045133, 2008.

[89] G. Kotliar and A. E. Ruckenstein, "New functional integral approach to strongly correlated fermi systems: The Gutzwiller approximation as a saddle point," *Phys. Rev. Lett.*, vol. 57, pp. 1362–1365, 1986.

[90] Z. Zou and P. W. Anderson, "Neutral fermion charge-e boson excitations in the resonating-valence-bond state and superconductivity in La_2CnO_4-based compounds," *Phys. Rev. B*, vol. 37, p. 627, 1988.

[91] S. Östlund and M. Granath, "Exact transformation for spin-charge separation of spin-1/2 fermions without constraints," *Phys. Rev. Lett.*, vol. 96, p. 066404, 2006.

[92] P. Pulay, "Improved SCF convergence acceleration," *Journal of Computational Chemistry*, vol. 3, pp. 556–560, 1982.

[93] G. Sordi, K. Haule, and A.-M. S. Tremblay, "Mott physics and first-order transition between two metals in the normal-state phase diagram of the two-dimensional Hubbard model," *Phys. Rev. B*, vol. 84, p. 075161, 2011.